"Development of a high temperature cooled fast response probe for gas turbine applications"

Mersinligil, Mehmet

Abstract

The measurement of unsteady pressures within the hot components of gas turbine engines still remains a true challenge for test engineers. Several high temperature pressure sensors have been developed but so far their applications are restricted to unsteady wall static pressure measurements. Because of the severe flow conditions such as turbine inlet temperatures of 1700°C and pressures of 50 bar or more in the most advanced aero-engine designs; few (if any) experimental techniques exist to measure the time-resolved flow total pressure inside the gas path. In this thesis, the development as well as the first experimental engine and test rig results obtained from a fast response cooled total pressure probe are presented. The designed probe was successfully tested at the turbine exit of a Rolls-Royce Viper turbojet engine, at exhaust temperatures around 750°C and in the Rolls-Royce intermediate pressure burner rig, at temperatures above 1600°C. Following tests with the first probe ma...

Document type : *Thèse (Dissertation)*

VON KARMAN INSTITUTE FOR FLUID DYNAMICS
TURBOMACHINERY & PROPULSION DEPARTMENT

UNIVERSITÉ CATHOLIQUE DE LOUVAIN
INSTITUTE OF MECHANICS, MATERIALS AND CIVIL ENGINEERING

Development of a High Temperature Cooled Fast Response Probe for Gas Turbine Applications

---

Thesis presented by Mehmet Mersinligil in order to obtain the degree of "Docteur en Science de l'Ingénieur", Université Catholique de Louvain, Belgium, May 2014.

Promoter: Prof. Tony Arts (Université Catholique de Louvain, Belgium)
Supervisor: Prof. Jean-François Brouckaert (von Karman Institute for Fluid Dynamics, Belgium)

Doctoral Committee:
Prof. Jean-François Remacle (Université Catholique de Louvain, Belgium)
Prof. Miltiadis Papalexandris (Université Catholique de Louvain, Belgium)
Dr. Jörg Weidenfeller (Alstom, Germany)

A selection of doctoral theses published by the von Karman Institute:

Detailed numerical characterization of the separation-induced transition, including bursting, in a low-pressure turbine environment
(J. Babajee, École Centrale de Lyon, France, November 2013)

Multi-dimensional upwind discretization and application to compressible flows
(K. Sermeus, Université Libre de Bruxelles, Belgium, January 2013)

Multiphase fluid hammer: modeling, experiments and simulations
(M. Léma Rodríguez, Université Libre de Bruxelles, Belgium/
Universidade da Coruña, Spain, October 2013)

Multiscale modeling of atmospheric flows: towards improving the representation of boundary layer physics
(D. Muñoz-Esparza, Université Libre de Bruxelles, Belgium, Septembre 2013)

Ground testing investigation of hypersonic transition phenomena for a re-entry vehicle
(D. Masutti, TU Delft, The Netherlands, June 2013)

Experimental study of the performance and stability of a low pressure axial compressor for a contra-rotating turbofan engine architecture
(N. Van de Wyer, Université Catholique de Louvain, December 2012)

A full catalogue of publications is available from the library.

Development of a High Temperature Cooled Fast Response Probe for Gas Turbine Applications

Keywords: high temperature, instrumentation, pressure probe, unsteady pressure, cooled probe, pressure measurement, measurement techniques

D/2014/0238/635, T. Magin, Editor-in-Chief
Published by the von Karman Institute for Fluid Dynamics with permission.

ISBN 978-2-87516-071-3

To my loving family…

In the realm of ideas, everything depends on enthusiasm;
in the real world, all rests on perseverance.

– Johann Wolfgang von Goethe

Acknowledgments

More than seven years have passed since I have left my home country to take a 'short break' of 9 months from my career as an aerospace engineer working on unmanned aerial vehicles, low Reynolds number aerodynamics and boundary layer stability by attending the world famous Diploma Course in the von Karman Institute. During this period, thanks to the very cosmopolitan composition of the VKI, I have had the chance to discover many different cultures, and to establish friendships that will hopefully last a lifetime with colleagues dispersed around the world. Apart from the social benefits, I had the chance to learn from world-class professors and to enroll in European level distributed research projects where I had to chance to visit many different universities and industrial facilities and collaborate with many valuable researchers, professors and engineers.

In terms of funding, this work has been supported by the EU Framework Program 6 project HEATTOP (Accurate High Temperature Engine Aero-Thermal Measurements for Gas Turbine Life Optimization Performance and Condition Monitoring) under Contract No. AST5-CT-2006-030696. HEATTOP was a new collaborative research project, which aimed to develop new, more durable, more accurate instrumentation for high temperature gas turbine applications. It was my personal honor to hear that HEATTOP was quoted as "public money well spent" by Dr. Rémy Dénos, the European commissioner responsible from this project and also a former VKI professor, who emphasized many achievements accomplished during the course of four years during his speech in the final meeting of HEATTOP.

I would like to thank my supervisor, Professor Jean-François Brouckaert for his valuable support and time during the course of my study. We have spent many hours together discussing results, the way to go ahead, planning tests and writing papers. Together, we had the chance of writing three journal papers just from the work presented here in this

thesis. I would also like to thank Professor Tony Arts, our department chairman, for sharing his experience at times when needed the most.

In addition, I would like to express my deep gratitude for Emeritus Professor Claus Sieverding, 'Santa Claus' for being available not only for technical discussions spending hours on end, always impressing me with his vast knowledge and experience, but also for being there at all times, even for personal matters.

It is impossible to realize such work without the support of technical personnel. It is very hard to list the names of all people who have constructed the team enabling this project. However to name a few, I would like to mention Willy Godard for stretching the limits of his lathe and milling machine for manufacturing pieces that could well find their place in a Swiss watch; Terence Boeyen for joining those tiny pieces and sensors under his microscope precisely just like a Swiss watch; Jean-Christophe Desilve, our lab technician is helping me out whenever needed; Pierre Cuvelier, our electronic lab technician for preparing the electrical control of our cooling system, writing PLC codes, building new signal conditioning amplifiers and repairing old ones; Julien Desset, our industrial engineer for handling relations with our workshop, our suppliers and also for traveling with me during the test campaigns not only as a support engineer, but also as a companion.

I also wish to thank Pete Loftus, James Roberts, and Richard Stevenson from Rolls-Royce PLC, Dr. Marios Christodoulou and Martin Haste from SCITEK Consultants Ltd, Sanel Zenkic and Edvard Svenman from Volvo AB (currently named GKN Aerospace) for enabling the measurement campaigns, comprising major part of this work presented.

The VKI has been our second home for many years since the beginning of the Diploma Course program. What made this place a second home was those true friends and fellows among which I'd like to at least mention the names of Fabio (BB) for his wisdom, Vasilis (Bill) for his fraternity, Benoît (Ben, the space marshal) for the shared Gin-Tonics or Vodka-Red Bulls, Delphine for her criticism and support, Lilla for long discussions and organizing barbecues, Tamás (the big guy) and Raimondo for constantly reminding our geeky nature. I'd also like to thank those fellows with whom I have shared offices at different times for cheering up the environment while being busy with mundane tasks:

Jan (Gianni), Rémy, Boris, Milan, Sara, Domingo, Stefano (Sheldon Lee Cooper), Christopher and Clara.

Finally, I'd like to thank my family, and especially my sister, Mérvé for being so patient and caring during hard times. If it hadn't been for their support, this work might never have come to fruition.

Abstract

The measurement of unsteady pressures within the hot components of gas turbine engines still remains a true challenge for test engineers. Several high temperature pressure sensors have been developed but so far their applications are restricted to unsteady wall static pressure measurements. Because of the severe flow conditions such as turbine inlet temperatures of 1700°C and pressures of 50 bar or more in the most advanced aero-engine designs; few (if any) experimental techniques exist to measure the time-resolved flow total pressure inside the gas path.

In this thesis, the development as well as the first experimental engine and test rig results obtained from a fast response cooled total pressure probe are presented.

The first objective of the probe design was to favor continuous immersion of the probe into the engine to obtain time series of pressure with a high bandwidth and therefore statistically representative average fluctuations at the blade passing frequency. The probe is water cooled by a high pressure cooling system and uses a conventional piezo-resistive pressure sensor which yields therefore both time-averaged and time-resolved pressures. The initial design target was to gain the capability of performing measurements at the temperature conditions typically found at high pressure turbine exit (800-1100°C) with a bandwidth of at least 40kHz and in the long term at combustor exit (2000K or higher).

The probe was first traversed at the turbine exit of a Rolls-Royce Viper turbojet engine, at exhaust temperatures around 750 °C and absolute pressure of 2.1 bar. The probe was able to resolve the high blade passing frequency ($\sim$23kHz) and several harmonics up to 100kHz. Besides the average total pressure distributions from the radial traverses, phase-locked averages and random unsteadiness are presented. The probe was also used in a virtual three-hole mode yielding unsteady yaw angle, static pressure and Mach number.

The same probe was used for measurements in a Rolls-Royce intermediate pressure burner rig. Traverses were performed inside the flame tube of a kerosene burner at temperatures above 1600°C. The probe successfully measured the total pressure distribution in the flame tube and typical frequencies of combustion instabilities were identified during rumble conditions. The cooling performance of the probe is compared to estimations at the design stage and found to be in good agreement. The frequency response of the probe is compared to cold shock tube results and a significant increase in the natural frequency of the line-cavity system formed by the conduction cooled screen in front of the miniature pressure sensor were observed.

Following tests with the first probe manufactured and tested in Rolls-Royce facilities, several improvements were made on the probe design among which the use of a leadless sensor and change in sensor wiring in order to improve signal are the foremost improvements.

Finally, the measurements performed at the turbine exit of a military engine with the second generation prototype are presented. The probe was immersed into the engine through the bypass duct between turbine exit and flame-holders of the afterburner of a Volvo RM12 engine, at exhaust temperatures above 900°C. The probe was able to resolve the blade passing frequency ($\sim$17 kHz) and several harmonics up to 100 kHz.

Contents

Nomenclature

Greek Symbols		
γ	Heat capacity ratio	-
μ	Dynamic (molecular) viscosity	kg/(m·s)
ρ	Density	kg/m^3
Roman Symbols		
C_p	Specific heat at constant pressure	J/(kg·K)
d	Diameter	m
dq	Incremental heat flow rate	W
dx	Incremental length along probe	m
f_n	Natural frequency	Hz
h	Convection heat transfer coefficient	W/(m^2·K)
k	Thermal Conductivity	W/(m·K)
L	Probe Length	m
M	Mach Number	-
m	Mass	kg
Nu	Nusselt Number $[(h \cdot d)/k]$	-
P	Pressure	Pa
Pr	Prandtl Number $[(C_p \cdot \mu)/k]$	-
Q	Heat flow rate	W
Re	Reynolds Number $[(\rho \cdot U \cdot L)/\mu]$	-
T	Temperature	K
Tu	Turbulence intensity	-
U	Velocity	m/s
V	Voltage	V
V	Volume	m^3
W	Width	m

Sub- and Superscripts

1	Inner surface of inner wall
2	Outer surface of inner wall
3	Inner surface, outer wall
4	TBC-probe interface
5	Outer surface of TBC
$\cdot$	Time rate
bl	Blockage
bp	Blade passage
c	Cavity
d	Based on diameter
g	Gas
in	Inlet
j	Index defining location
o	Total quantity
out	Outlet
p	Surface
s	Sensor
TBC	Thermal barrier coating
w	Water

List of Figures

List of Tables

Chapter 1

Introduction

From the invention of the jet engine by Sir Frank Whittle (April 1937) and Dr. Hans von Ohain (September 1937), technology has evolved from turbojets having pressure ratios at the order of 3:1 with single-stage uncooled turbines with inlet temperatures below 800°C, to modern multi-spool high bypass ratio turbofans with core engine pressure ratios exceeding 40:1, having combustors burning air-fuel mixtures at the edge of dissociation and complex cooled turbines with inlet temperatures at the order of 1600°Cmade of single-crystal alloys.

In parallel to this evolution, the design and analysis tools have progressed with the help of developments in measuring capabilities, computer technology and large amounts of know-how accumulated. The use of computers has gone beyond now-conventional areas such as computer aided design and manufacturing (CAD/CAM) with the development of computer aided engineering (CAE) tools. To mention a few, finite-element methods (FEM) allowing to calculate the stresses in components opened a new era in structural design. Likewise, computational fluid dynamics (CFD) progressed from steady, inviscid panel methods to time-resolved large-eddy simulations (LES) and direct numerical simulations (DNS).

Recently, the 'old-school' method of building dedicated rigs for each component, and basing the design on experimental data collected on these rigs has lost the feasibility due to a parallel increase of computational power and decrease in costs for super-computer clusters.

On the other hand, CFD methods are still far from resolving the reality especially in complex flow patterns such as those found in turbomachinery flows. In order to 'fine-tune' numerical tools and to create the

better numerical models through better understanding of flow physics, there still is, and will be a demand for experimental validation data. With the use of unsteady numerical methods, the demand on the experimental side has also shifted towards time-resolved measurements. Still, a major part of the design process is based on assumptions and correlation tables that are 'known to work' thanks to years of experience on the subject, limiting improvements on new designs. For instance, due to the lack of turbulence intensity data at the combustor exit, the turbine designer has to assume a value 'high enough' to keep his design in a safe envelope. Apart from design purposes, accurate measurements in the hot gas path are also crucial for engine condition and performance monitoring and are likely to revolutionize approaches in controls and diagnostics.

Besides the interest to validate numerical predictions of engine performance, efficiency, and component life, the availability of high temperature steady and unsteady pressure and temperature data would also enable much progress in the field of condition monitoring and active control technologies, as outlined by Simon et al. [69], 2004, in their review of sensor needs for control and health management of future intelligent aircraft engines.

Due to the limitations of current experimental techniques and also the severity of conditions in modern turbomachinery flows, measurements of temperature and pressure in the hot parts of modern aero-engines and stationary gas turbines remains a true challenge for measurement and instrumentation engineers. Enabling flow-path measurements of unsteady pressure with the aim of achieving considerable advances in design and analysis of the flow-field in the hot parts of gas turbines and aero-engines comprises the focus point of this thesis work, where flow temperatures are in excess of 1600°C and pressure levels are above 40 bar for certain components and applications.

This thesis is structured in the following manner: In Chapter 2, a thorough literature survey categorizing existing literature into wall measurements and probes is presented. In Chapter 3, in addition to the probe concept, the environmental conditions and the design objectives are presented. In Chapter 4, the probe design is discussed in detail. Material selection and manufacturing processed are presented together

with a brief description of the probe cooling system in Chapter 5. In Chapter 6, Turbojet engine and combustion rig tests of the first probe manufactured are presented. Finally, In Chapter 7, the second generation of the probes are presented together with a test campaign on a turbofan engine, before concluding this work in Chapter 8.

Regarding unsteady pressure measurements above temperatures of 1000 °C, few, if any accurate and reliable technique exists to measure the time-resolved gas path total pressure. In gas turbine combustors or in hot turbine sections, attempts to measure unsteady pressures have traditionally been accomplished using two different types of devices: flush mounted wall pressure sensors or immersion type instruments. In Chapter 2, a thorough review of the available literature is presented covering both types of instruments.

Two gas turbine instrumentation organizations, composed of Original Equipment Manufacturers (OEMs), instrumentation vendors and research institutions including academia, on both sides of the Atlantic highlight these needs in their respective capability vs. requirement charts. The Propulsion Instrumentation Working Group (*www.piwg.org*), or PIWG in short, located in the U.S. has performed a survey and issued specifications in order to fulfill these requirements [63]. In Europe, the European Virtual Institute for Gas Turbine Instrumentation (*www.evi-gti.com*), or EVI-GTI in short, has prepared 'The Lab Gap Matrix' [19] identifying the missing instrumentation capabilities not only limited to flow-field measurements, but covering all different disciplines (such as structural, thermal, aerodynamic, etc.) for both design and operation purposes. These two organizations keep the aforementioned documents up-to-date with the help of bi-annual joint meetings. A recent summary of state-of-the art in gas turbine instrumentation together with sensor and measurement capability needs in high temperature environments can also be found in the lecture notes of Niska [57].

Major needs for measuring capabilities in the hot gas path are concentrated to unsteady pressure and temperature measurements. After many years developing sensors and transducers, thermocouples are still the widely used sensor of choice when it comes to measuring high temperatures. Even though resistance temperature devices (RTD) and thermistors are found to be more accurate and resistant to aging effects

such as drift, their application range falls way below of high temperature thermocouples. For time-resolved measurements, the only known method with field success known to the author is the dual thin film probe patented by Chana [9].

Regarding time-resolved pressure measurements, advances in Fabry-Pérot interferometers, piezo-electric and piezo-resistive transducers are noteworthy. However, piezo-resistive transducers outshine other methods for measuring unsteady pressure in the gas path, as they can be miniaturized into sizes unachievable with any other technique and provide both steady and unsteady pressure components.

Measuring in a flow environment characterized by unsteadinesses of the order of tens of kHz with temperatures exceeding the melting points of most metals, poses a great challenge to test and measurement engineers.

The long term goal of the probe development presented in this thesis, and discussed in detail in Chapter 3, was initially defined as "the measurement of the unsteady flow behind turbine rotors and instabilities in combustion chambers". The short term goals were summarized as a proof-of-concept via measurements at temperature levels typically found at High-Pressure Turbine (HPT) exit conditions ($\sim$800–1100 K), with a sufficiently high bandwidth in order to resolve the fundamental frequency and several harmonics.

In order to obtain accurate measurements in the highly unsteady and three-dimensional flow-field in turbine stages, it is mandatory to have adequately long acquisitions for off-line analyses. Concerning pressure measurements at high temperatures in particular, it is important to keep the probe continuously in the hot gas path in order to avoid any thermal shock from contaminating the recordings, which necessitates the use of a highly efficient cooling system. The main advantage in this approach is the recording of time-series at stable operating conditions, where the probe is in thermal equilibrium.

The probe design concept discussed in detail in Chapter 4, is based on a high-temperature 'Silicon on Insulator' (SOI) piezo-resistive pressure transducer surrounded by cooling channels for operation at temperature levels much higher than the metal melting point, yet alone the sensor

temperature limit. In order to maximize the bandwidth, the sensor is placed at the probe tip behind a screen incorporated in the probe design, protecting the sensor diaphragm from any impinging particles. The cooling scheme is essentially based on a co-centric tube assembly, providing separate channels for feed and return of the coolant, with the sensor placed normal to the probe axis within a tube incorporating an extra co-centric coolant passage around the sensor extending through the screen. This arrangement provides a means to cool the screen upstream the sensor diaphragm by conduction.

The initial design study has been focused on investigating different probe and cooling scheme arrangements for continuous operation of the probes at temperatures as high as 1400 K and pressures up to 40 bars. Both gaseous and liquid coolants and refrigerants have been investigated. Distilled water has been employed as the coolant of choice both due to its high specific heat capacity and in order to avoid any film formation (i.e. lime) acting as an unwanted thermal-barrier inside the cooling channels hampering the cooling effectiveness. The use of ceramic Thermal Barrier Coatings (TBC), typically used for coating turbine blades, in order to reduce the heat in-flux and metal surface temperatures has also been investigated. In addition to cooling the probe shaft, requiring a uniform coolant flow without stagnant regions, the most difficult challenge in a cooled probe design has been identified as cooling the sensor diaphragm via cooling the gas in the cavity upstream the sensor diaphragm.

In order to have a means to calculate for the global thermal parameters, allowing to carry out a parametric study helping to optimize a probe for a specific application or assessing the performance of a cooing scheme under different environments, a mono-dimensional model explained in Section 4.3.1 has been created solving the conjugate heat transfer into the probe from the hot stream and within the probe.

In addition to the mono-dimensional model, two- and three-dimensional Navier-Stokes simulations presented in Section 4.3.2 and 4.3.3 have been carried out. The reasoning for the numerical prediction campaign is three-folds. The first aim is to validate and if necessary, calibrate the predictions obtained using the mono-dimensional tool developed. The second aim is to search for any stagnant or re-circulating zones within the

coolant stream suspected to create hot-spots inducing thermal stresses and rendering the cooling system insufficient. The third and the most important aim is to obtain a detailed flow-field analysis yielding the temperature distribution which has not been modeled in the mono-dimensional prediction tool.

As explained in Chapter 5, emphasis has been given on material selection with more than one constraint in mind. Besides having appropriate thermal properties, the material of choice for such an application needs to be machinable and weldable in addition to having creep and corrosion resistance. A cooling system has been designed for the sole purpose of providing the coolant to the probe designed. The intention of having measurement campaigns outside lab environments, but on real aero-engines has necessitated having redundancies against any failure on the cooling system. Studies have been conducted for sealing design, joining techniques and non-conventional machining techniques prior to probe manufacturing. Once the prototype probe has been manufactured, full static, dynamic and aerodynamic calibrations have been performed.

Finally, in Chapter 6, successful prototype probe tests performed at the turbine exit of a Rolls-Royce (RR) Viper mk.201 turbojet engine and in the Rolls-Royce Intermediate Pressure (IP) Combustion Rig are presented; marking an important milestone as first fast-response pressure measurements within the hot gas-path in a turbine and a combustor, and thus opening a new era in flow-characterization in turbomachinery flows.

Several changes which were made for a second generation of the cooled probe with the help of the experience gained with the first prototype together with the tests performed using this improved cooled probe design at the LPT exit of a Volvo Aero RM-12 low-bypass ratio military turbofan are presented in Chapter 7.

Using a high temperature total pressure probe, the unsteady pressure field between turbine blade rows, the shock position and the wake passing events may be obtained. The single sensor probe has also been used in a virtual 3-hole mode, yielding the periodic flow angle fluctuations.

Chapter 2

Literature Survey

Unsteady pressure measurements has been, and still is, regarded among the interesting research topics and thus have been the subject of various review papers. A review of the state-of the art as of 1979 concerning steady and unsteady pressure instrumentation for gas turbines was published by Armentrout and Kicks [60]. Two papers, both published in 1980, first by Lakshminarayana [43] and another by Carta and O'Brien [8] are focused on the fast-response instrumentation for unsteady aerodynamic measurements and turbulence measurements in turbomachinery flows.

A more recent and substantial review on the progress in measurement techniques in unsteady flows in turbomachinery environments using surface instrumentation for determination of shear-stress, heat flux and pressure and using probes for determination of time-resolved pressure and temperature is published by Sieverding et al. [68] in 2000. Again in 2000, Ainsworth has published a similar review focused on unsteady pressure measurements [2], in addition to the publication detailing the state-of-the art on fast-response aerodynamic probes by Kupferschmied [36]. However, it is worth to mention that these contributions are limited to low-temperature systems that are typically below 400 K.

There are only a few techniques existing for accurate and reliable fast-response total pressure measurements at high temperature as explained in section 2.2.2.3, which are still far below the temperature levels in the hot sections of modern gas turbines or are limited to a few kHz of bandwidth. In high temperature sections of gas turbines such as turbine exit flows and combustion chambers, the attempts to obtain unsteady

pressure measurements are accomplished using either flush-mounted wall sensors or immersing instruments such as probes.

2.1 Very High Temperature Sensors and Cooled Sensors for Wall Pressure Measurements

Even though flush-mounted wall sensors by definition do not measure the flow-path total pressure, which is the focus of this study, some high temperature sensors have been developed for the purpose. Work in this area may be categorized as very high temperature sensors and cooled sensors typically incorporating a cooling jacket around a somewhat more conventional sensing element.

2.1.1 High Temperature Pressure Sensors

The great majority of the sensors for measuring unsteady pressure may be categorized as piezo-electric sensors, piezo-resistive (a.k.a. semiconductor) sensors and Fabry-Perrot interferometers.

In a piezoelectric sensor, being typically a force transducer, the pressure is collected with the help of a membrane which is linked directly onto the piezo element by the aid of a shaft. Indeed, the main purpose of the membrane is the separation of the sensor back-end from the measured medium, eliminating membrane flexure and in turn increasing sensor life. For this reason, this is the foremost unsteady-pressure sensor type utilized in the aero-engines and gas-turbines that are delivered to the end-users. Another advantage of piezo-electric sensors, being active devices not requiring and power supply, is the simplicity in electrical connections requiring only two electrical contacts. Due to this very reason, the piezo-electric sensor only measures AC components and does not respond to the steady component. Typical sensor bandwidths are at the order of 15 kHz. In addition, the major disadvantage, again due to the operating principle of these sensors, is the requirement to have relatively large membranes. In fact, the pressure applied on the membrane

surface is transmitted to the piezo element, creating a direct proportion between the membrane area and the sensitivity.

The piezo elements used in these sensors may be categorized under ceramics and crystals. The most typical ceramic elements are PZT (Lead Zirconate Titanite with applications limited to 500 K and BiT (Bizmuth Titanite) with applications limited to 800 K. Current commercial high-temperature piezoelectric sensors are based on crystal piezo elements, mainly Tourmaline crystals allowing operation up to 1050 K. A disadvantage of crystal piezo elements compared to ceramics is the low sensitivity levels. A new crystal element, $GaPO_4$ (Gallium Phosphate) offers slightly better sensitivity values at even higher temperatures, stretching the limit for these sensors to 1200 K as reported by Schmid [64] and Schricker [66].

Another technique that is long-known, but recently gaining popularity is the Fabry-Pérot interferometry. These interferometers allow measuring both steady and unsteady pressure at bandwidths currently at the order of 50 kHz. With the use of sapphire crystal membranes and high temperature optical fibers, the temperature capability has been demonstrated at levels around 1300 K by Gahan [23]. With the use of a second cavity behind the pressure measuring membrane, a sensor of this type may also be used to measure the steady temperature, as already reported by Kersey and Dandridge [33] and Inci et al. [28] more than two decades ago. A major disadvantage of the Fabry-Pérot interferometer pressure sensor is the difficulty in harness layout. The inability to bend the optical fiber signal cables with tight radii and the necessity to use a complex optical interrogator creates difficulties in installation.

Even though the above mentioned sensor types offer great temperature capabilities, the sheer size of these sensors prohibit their use in aerodynamic probes, as noted by Brouckaert [7]. For this reason, the piezoresistive, or semiconductor, pressure transducer is the sensor type of choice allowing measurements of steady and unsteady pressure components simultaneously with transducer sizes unachievable with above mentioned sensors.

A disadvantage for the semiconductor sensor is the requirement of having a minimum of four conductor leads, which in turn complicates the

harness design and shielding against EMI/RFI (Electromagnetic Interference and Radio Frequency Interference) noises, etc. On the other hand, they are proven to be robust and available for applications ranging from 0.35 to 70 bar, allowing measurements at high bandwidths typically ranging from 20 kHz to 1 MHz.

Conventional piezoresistive pressure transducers are built using typical semiconductor manufacturing techniques, such as diffusion and etching. Typically, a Wheatstone bridge is formed by four resistors diffused on top of a silicon membrane. The use of Phosphor and Boron to create p-n junctions as in transistor technology limits the thermal envelope of the conventional piezoresistive transducer to temperatures below 420 K due to the decrease in the band gap, which may be defined as the energy required to excite an electron from the valence band to the conduction band, creating current leakages which in turn self-destruct a silicone chip.

Concerning piezo-resistive pressure transducers, possible improvements have been reported by Mallon [49]. In 1992, Kurtz et al. [41] has reported that by replacing the P and N wells used in junctions with glass, a silicon-on-silicon sensor was manufactured which can operate up to 800 K. It is also claimed that by doing so, the optimum in high temperature piezo-resistive pressure sensors is achieved.

A technique first introduced and perfected by IBM [13] for building high-speed transistors that can be used to deliver higher performance microchips for computer chip applications, called “silicon-on-insulator (SOI)”, represents a fundamental advance in the way chips are built. As noted by Mendez [51], the benefits of SOI technology may be summarized as the complete isolation of n-well and p-well structures and low parasitic capacitance due to isolation from the bulk silicon membrane which in turn eliminates the current leakage problem associated to conventional chips. This technique, employing an insulating layer, typically SiO_2, between the bulk silicon and the structures atop has stretched the temperature limits up to 780 K, limit now being the plastic deformation of silicon at temperatures reaching 900 K.

The problems related to leads of the transducer limiting the operable temperature levels have been overcome with this improvement, which

is the replacement of P-N junction isolation technique with complete oxide isolation technique (i.e. SOI transducers), in order to bond the strain gauge onto the diaphragm, extending the limits. Laboratory demonstration of 'leadless' ruggedized SOI transducers that have operational temperatures in excess of 873 K and accelerations greater than 200 g as reported by Kurtz et al. [39] in 2004. A schematic representation of SOI type transducers is shown in Figure 2.1 together with a conventional junction.

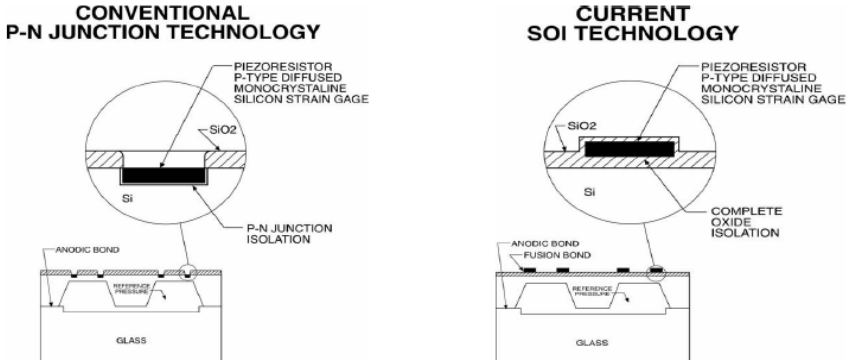

Figure 2.1: Piezoresistive silicon strain gages are integrated within the silicon diaphragm structure but are electrically isolated from the silicon diaphragm [39]

The latest evolution of the patented Silicon on Insulator (SOI) technology enabling the piezoresistive sensing elements to be di-electrically isolated from, while being molecularly attached to a silicon diaphragm are shown on a 'leadless' sensor in Figure 2.2. These current sensors have dynamic responses ranging from 150kHz up to 1MHz depending on pressure level.

A 'leadless' sensor chip incorporates a rim for hermetic sealing at the gauge side of the diaphragm around the strain gages as shown in Figure 2.3 and a glass contact wafer having 4 holes for the contact wires to pass through.

The advantage of leadless sensors compared to the conventional sensor mounting scheme is the replacement of wire-bonds used for creating

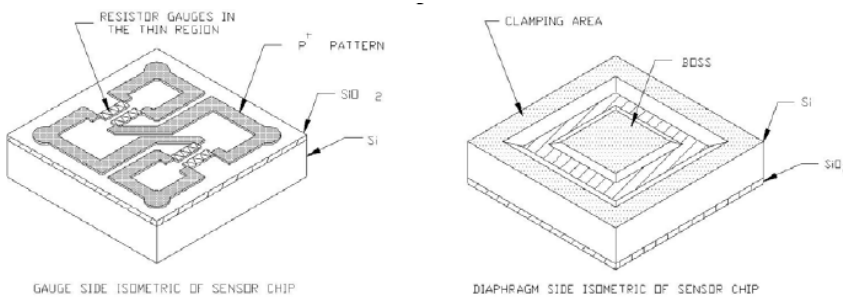

Figure 2.2: The gage and diaphragm side views of a modern SOI transducer chip [39]

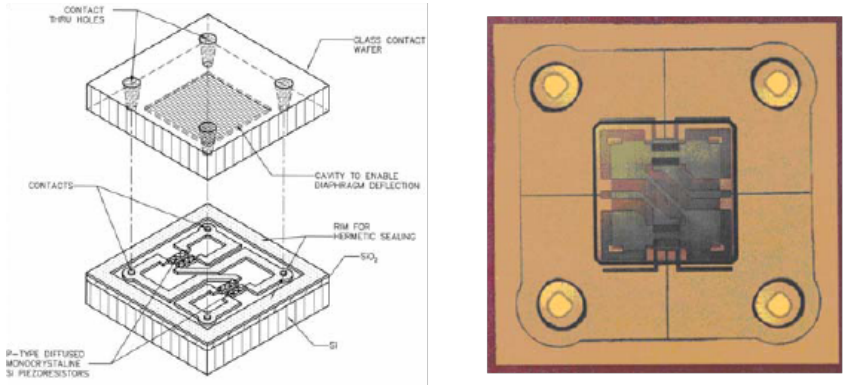

Figure 2.3: Schematic view of the 'leadless' SOI chip: Schematic on the left and picture of the actual chip with the glass wafer attached on the right hand side [40]

the contact between the signal-transmission wires and the sensor chip by reversing the sensor chip, creating a direct bond to contact pins during sensor baking under vacuum, which is an essential process for production of absolute sealed sensors. Other advantages are the increased protection of the resistors from foreign object damage and a slight increase in temperature capability due to the elimination of wire-bonding procedure, pushing the sensor operation limit up to 873 K.

Above 900 K, it is impossible to employ silicon as the matrix material

undergoes plastic deformation as summarized by Ferguson [20]. Current trend is to employ silicon carbide (SiC) or boron oxide quartz as presented by Kulite Semiconductors. Such a high temperature piezo-resistive SiC pressure sensor is reported to be currently operational up to 873K is demonstrated by Ned et al. [56] and shown in Figure 2.4. The leadless bonding scheme, shown in Figure 2.4a is the same as described above in Figure 2.3 for SOI sensors.

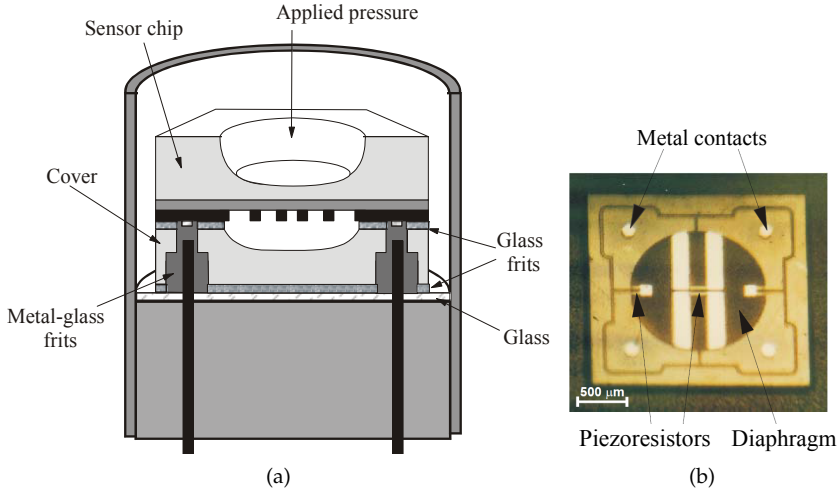

Figure 2.4: (a) Silicon Carbide transducer schematic (b) Photograph of the SiC chip [56]

Further gains in the temperature capability is still possible thanks to SiC (Silicon Carbide) based sensors allowing extended use up to 880 K [56], and have been demonstrated in a cantilever beam configuration at that temperature in a running gas turbine [58]. A comprehensive review of high temperature pressure transducers as of 2009 is given by Chivers [11].

One of the drawbacks associated with the use of piezo-resistive sensors at variable temperature environments is their thermal stability, altering the zero-offset and sensitivity with respect to temperature. As the electrical resistance of the resistors forming the Wheatstone bridge are

changing with respect to temperature, the sensitivity of piezoresistive pressure transducers also change as a function of temperature. These thermal errors are resolved either using passive compensation modules or an active compensation. The passive compensation module is based on the knowledge of the temperature coefficient of resistance for the piezo-resistor materials employed, and are typically delivered with a commercial transducer. Welsh and Pyne [74] have shown in 1980 that if a transducer is supplied with a constant voltage, the change in Wheatstone bridge resistance due to temperature induces a change in current drawn by the bridge. This change in bridge current can be tracked by the potential drop across a 'sense' resistor placed in series with the bridge. Hence, for higher temperature applications, passive compensation is deemed insufficient and the active compensation technique explained by Welsh and Pyne should be utilized in order to keep a track of sensor temperature, removing the necessity of a passive temperature compensation module in the expense of having a full pressure and temperature calibration as previously demonstrated by Mersinligil et al. [52].

For SOI sensors, the potential drop across the sense resistor in active compensation technique is a linear function of the temperature within the range of interest. As suggested by Kupferschmied [37] and Cherrett [10], this linear correlation linking the sense potential drop to the bridge temperature may be exploited such that the pressure transducer may be used as a resistance temperature device (RTD). Due to the high thermal inertia of the piezoresistive transducer compared to thermocouples, the SOI transducer temperature measurements are confined to steady readings. However, as demonstrated by Mersinligil et al. [53], the simultaneous measurement of steady temperature and unsteady pressure at the same spot makes it attractive to make entropy measurements. As stated by Denton , "entropy is the only rational measure of loss in machines extracting work" [14].

However, for SiC sensors, the correlation between temperature and the sense voltage is not linear as shown in Figure 2.5. In fact, due to the nature of the characteristic, the sense voltage may be the same at two temperature levels, prohibiting the use of these sensors across wide temperature ranges. Currently the only feasible way to use these sensors, adding a great difficulty to the measurement technique, is tracking the thermal history of the sensor starting from non-trivial temperature lev-

els or adding a stable temperature transducer such as a thermistor, and RTC or a thermocouple into the sensor package.

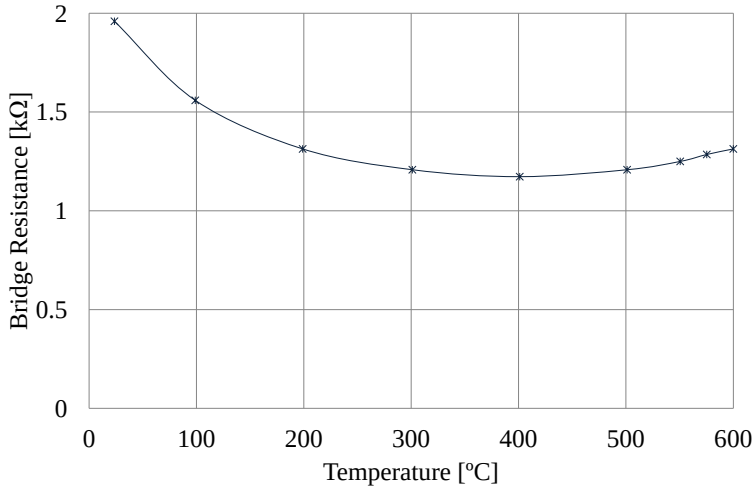

Figure 2.5: Non-monotonic resistance change with temperature for a leadless SiC sensor [56]

2.1.2 Cooled Sensors

In the last decade, a few cooled piezoresistive pressure transducers have been commercially released. The cooling jacket design studies for those transducers were published by Ferguson and Ivey [21, 22] reporting operation up to 1370 K for water-cooled configurations and up to 1070 K for air-cooled variants. One of the most recent studies on this concept, again by Ferguson and Ivey shown in Figure 2.6, is the air-cooling jacket around a commercial piezoresistive high-bandwidth transducer with quoted temperature capability up to 1170 K [32]. As previously explained with piezoelectric transducers and Fabry-Pérot interferometers, the sheer size of the cooled piezoresistive sensor assembly becomes significantly large for a probe design. On the other hand, with temperature capabilities not exceeding competitor sensor types, cooled piezoresistive sensors have not gained wide spread.

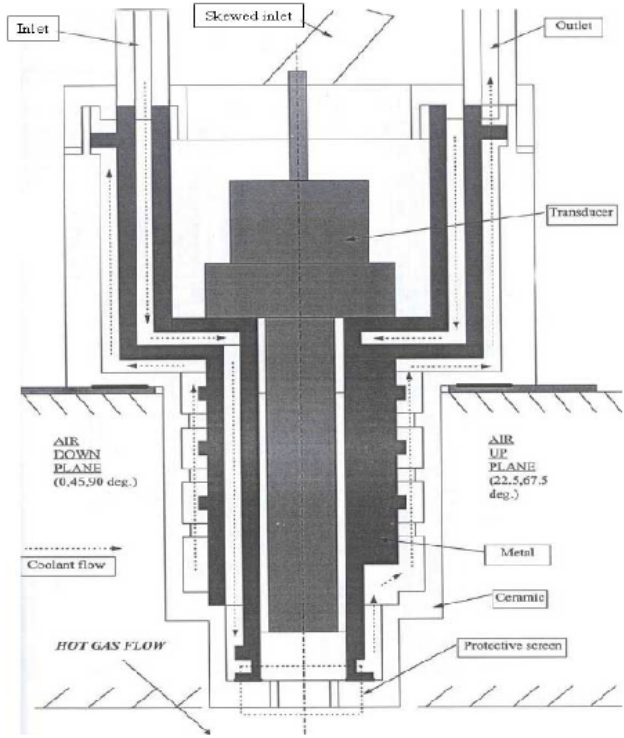

Figure 2.6: Air cooled jacket design, Ferguson and Ivey [31]

2.1.3 Thermal Protection

Thermal protection have been proven to be effective and successful through many years of research and application. Using ceramic thermal barrier coatings (TBC) are common practice in gas-turbine industry at turbine blades, since it reduces the heat flux through the surface greatly thanks to very low conductive properties, and hence greatly reducing metal surface temperature levels.

Ceramic thermal barrier coatings are highly favored due to very high melting point, very low conductivity and acceptable strength. However, they are brittle and therefore sensitive to thermal expansions, while ex-

pensive and hard to apply. These coatings are applied in liquid form by means of spaying and fixed on the surface by a heat-treatment process. As noted by Ivey and Ferguson [31]; "The Finite Element Model predictions indicated that the best form of thermal barrier was an entire ceramic structure."

On the transducer side, Kistler has applied such ceramic protector units in front of a piezo-resistive sensor and achieved good protection against thermal shocks. Using this approach, transducers operable up to 600K are now available commercial off-the-shelf. A patent has been published in the U.S. by Cook [12] in 1990, originally filed in 1970, in which a honeycomb-like member is used to secure both pressure release and thermal transfer for the piezoelectric sensor.

2.2 Immersion Type Instruments – Probes

Concerning unsteady pressure measurements in flow regimes with temperatures higher than sensor capability, two methods are found to be feasible. First and the most conventional method is the use of a cooled probe, where the probe itself together with the transducer(s) is cooled using a coolant fluid. Another approach is the use of a fast traverse mechanism allowing measurements until the transducer employed starting from a low ambient temperature heats up to a determined threshold, after which the probe is retracted promptly.

2.2.1 Fast Probe Immersion

The fast immersion technique, pioneered by Oxford University, is based on the use of conventional fast-response aerodynamic probes without cooling coupled with a fast probe traverse using a pneumatic actuation scheme shown in Figure 2.7. In this method, the probe is cooled outside the measured environment by creating an air curtain within the traverse housing; where the probe initially at ambient conditions is rapidly inserted into the hot flow, and again rapidly retracted following acquisition before the sensor(s) reach a critical temperature, avoiding any damage. The actual insertion and retraction durations are as little

as 80 ms, while the whole traverse is completed approximately within 0.2 s.

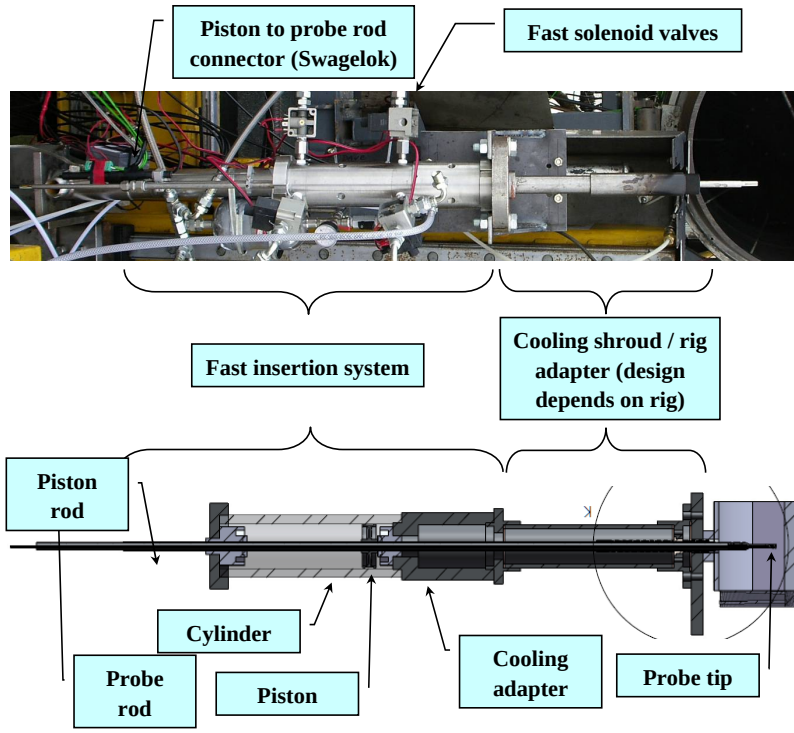

Figure 2.7: Oxford Pneumatically driven linear traverse mechanism [48]

Numerous pressure and temperature probes with a diameter of 6 mm have been built incorporating commercial off-the-shelf sensors such as thermocouples and piezo-resistive pressure transducers, pneumatic ports and dual thin film sensors in order to measure both steady and unsteady pressure and temperature. a "Mk II" probe is shown in Figure 2.8 incorporating a K-type thermocouple, dual thin-film gauges for measuring total temperature, a Kulite pressure transducer and a pitot tube for measuring total pressure. Measurements performed in an industrial gas turbine using fast-immersion probes have been reported by Passaro et al. [61]. A complete overview of this innovative approach together with

details of various probes built is published by Oldfield and Lubbock [59].

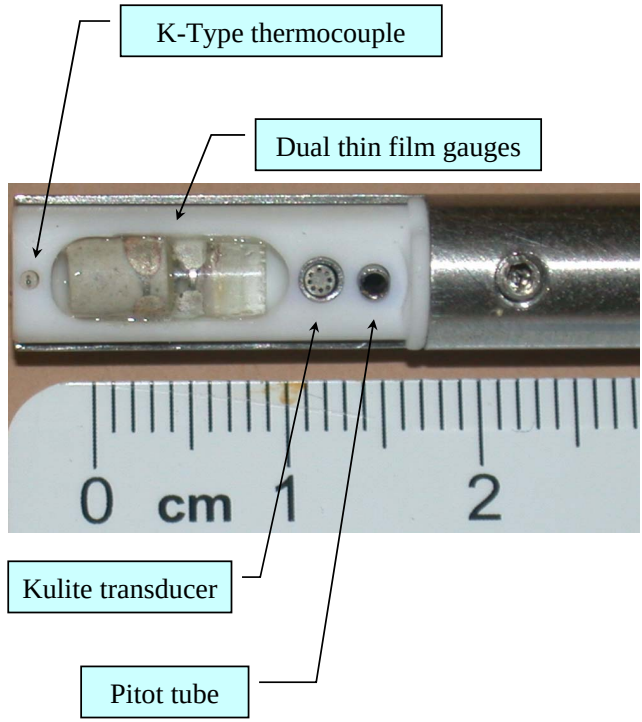

Figure 2.8: Oxford mk.II probe [48]

The major drawback of this technique lies in its operating principle, which is the short immersion duration at the order of 200 ms. As the probe is rapidly inserted into the flow of interest, the transducers go through an immense acceleration, rendering measurements during the travel impossible. Moreover, for pressure measurements, the thermal transient occurring on the sensor membrane during immersion disallows the measurement of a steady component, while the time-constant of the pneumatic port is barely enough, and for some cases insufficient, for a proper steady pressure level determination before the transducer critical temperature is reached, forcing retraction. As the piezoresistive sensor does not reach steady-state in term of temperature, together with

the existence of a strong thermal transient across piezoresistive elements forming the bridge, calibration of the sensor also poses a serious problem that is yet to be addressed.

2.2.2 Cooled Probes

2.2.2.1 Early work

The development of probes for high-temperature environments, initiated with early plasma research dates back to 1923, where Langmuir [44] has published his results in very low-density ionized gas flows, yielding low heat-flux values. As detailed in the contribution of Grey [25], a complicated diagnostic probe incorporating double sonic-orifices based on a forced cooling method have been developed in the late 1940s, again for low-density flows.

Recalling the fact that the heat-flux into the probe is proportional to the density of the medium, initiation of dense plasma research marks the development of sophisticated probe cooling techniques for calorimeters, heat-flux, electrostatic and gas sampling probes with heat flux levels reaching several MW/m^2, posing a great difficulty in measuring gas properties. Grey has published a thorough state-of-the art of these techniques as of 1970 [26].

In the earlier calorimeter probe designs, total isolation of the calorimeter from the exterior 'cooling jacket', required for high heat-flux environments, have been unsuccessfully attempted. The breakthrough avoiding this problem is the introduction of a 'tare' measurement, where the cooling rate required to maintain the probe temperature without gas sample aspiration is subtracted from the cooling rate required otherwise, enabling the gas sample enthalpy determination. The sketch of the probe constructed using pure copper with stainless-steel supports is shown in Figure 2.9, where water pressurized up to 55 bar is fed into the probe from an outer jacket passing through the probe tip and an inner jacket, surrounding the gas sampling tube, before exiting. Sheathed thermocouples are utilized to determine the coolant temperature rise together with the cooled gas sample temperature.

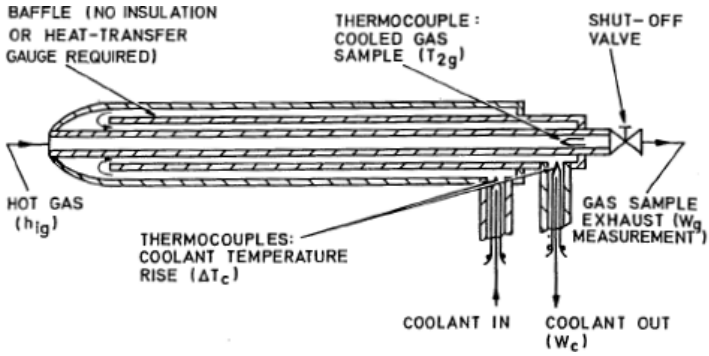

Figure 2.9: Calorimetric probe used with tare-measurement technique, Grey [26]

The complete system diagram used for enthalpy measurements is shown in Figure 2.10. The coolant temperature rise and flow-rate are measured to determine the cooling rate in two configurations: first with the gas sampling path closed by the aid of a valve, while measuring the steady pressure, and second with aspiration for gas composition analysis.

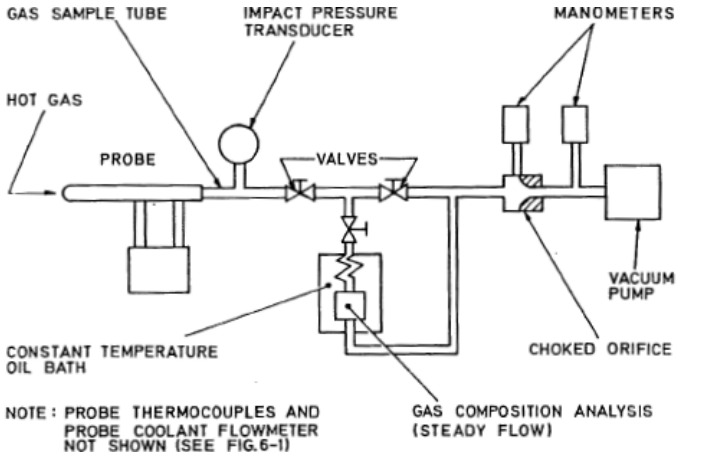

Figure 2.10: Diagram of instrumentation used with tare-measurement calorimetric probe, Grey [26]

The probe concept with variants as small as Ø1.6 mm has been successfully utilized in a wide range of flowfields enduring continuous operation in pressures up to 100 bar with a heat flux as high as 82 MW/m^2. The heat transfer capability of the probe is shown in Figure 2.11.

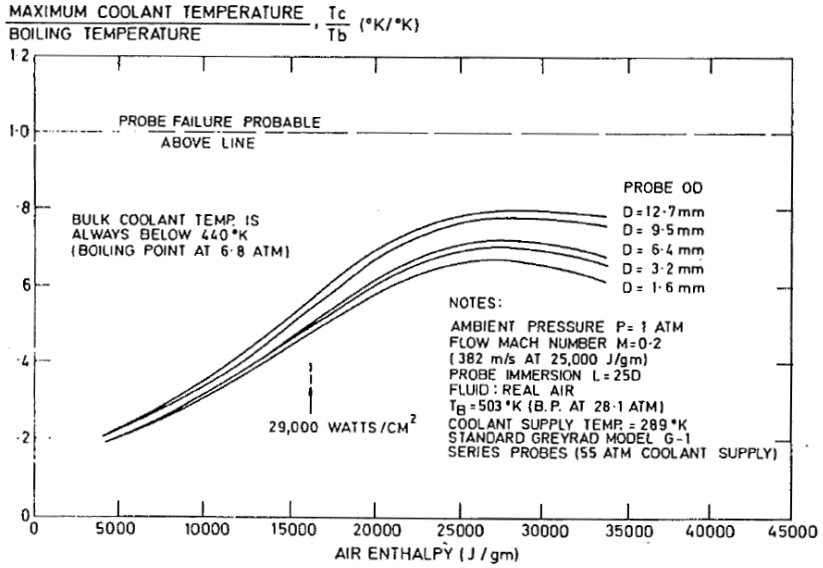

Figure 2.11: Heat transfer capability of simple tare-measurement probe, Grey [26]

Another variant of the same probe concept with the calorimetric portion of the probe isolated from the cooling jackets with sizes as small as Ø4.8 mm is shown in Figure 2.12. This ingenuity enables the variation of the coolant flow within the calorimeter independently from that of the surrounding cooling jacket, allowing to set the desired temperature rise and hence setting sensitivity. By decreasing the calorimeter coolant flow rate, the problem arising especially at low pressures due to the low ratio of heat absorbed from the gas sample to total heat absorbed by the coolant (i.e. including probe cooling), decreasing the sensitivity and therefore increasing associated measurement errors is avoided.

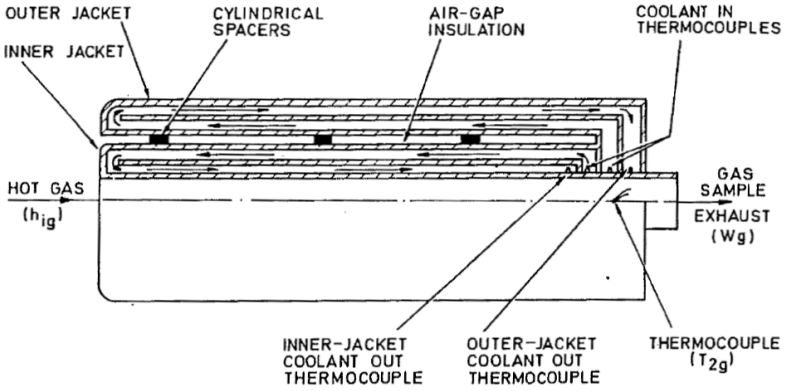

Figure 2.12: Double probe (fully isolated calorimeter) for stagnation point measurements, Grey [26]

2.2.2.2 Pneumatic Probes

Several water-cooled pneumatic pressure probes have been patented for continuous operation in high-temperature flows. In the design patented by Ashby in 1988 [5], a pressure transducer is placed within a pressure chamber connected to an external cooling system via tubes as shown in Figure 2.13. The drawback of this design arising from the use of a pressure chamber is the high settling-time confining the probe to steady measurements.

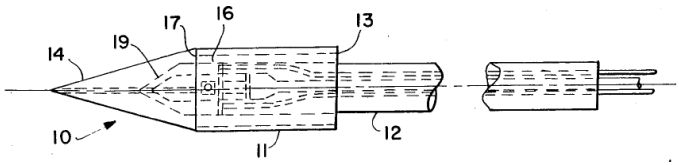

Figure 2.13: Cooled total pressure probe, Ashby [5], 1988

On the other hand, in 1991 Lagen et al. have patented a water-cooled static pressure probe for steady measurements with quoted operation temperature up to around 1650 K [42] which is shown in Figure 2.14.

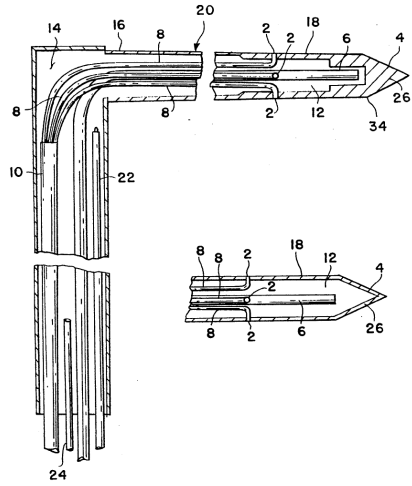

Figure 2.14: Cooled static pressure probe, Lagen et al. [42]

It is also worth mentioning the 4-hole pneumatic probe presented by Warnack in 2002 [73], shown in Figure 2.15, incorporating a thermocouple, with an uncooled Ø6 mm tip and a water-cooled stem allowing operation at temperatures up to 1070 K.

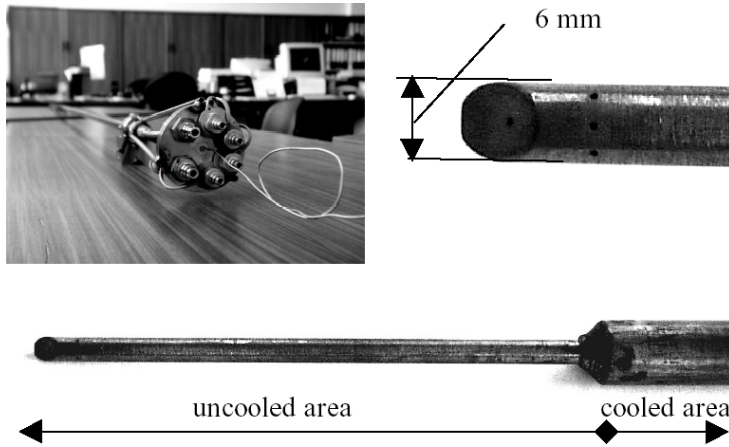

Figure 2.15: Water-cooled 4-hole pneumatic probe, Warnack [73], 2002

A more recent high-temperature 3-hole pneumatic pressure probe has been designed for aero-engine in-situ measurements at pressure levels up to 30 bar temperature levels slightly above 1600 K. Measurements downstream of IP and HP turbine stages for the Rolls-Royce Trent 900 engine (powering the Airbus A380 airliner) performance test using an in-engine radial traverse gear and this high-temperature 3-hole pneumatic probe has been presented by Anderson et al. in 2008 [4]. Successful measurements of the total pressure, yaw angle, total temperature and Mach number through the engine operating envelope has been demonstrated. The cooled traverse gear incorporating all the transducers and electronics required, with a requirement to be mounted between the liners separating core flow from the by-pass flow at temperatures around 550 K is shown in Figure 2.16.

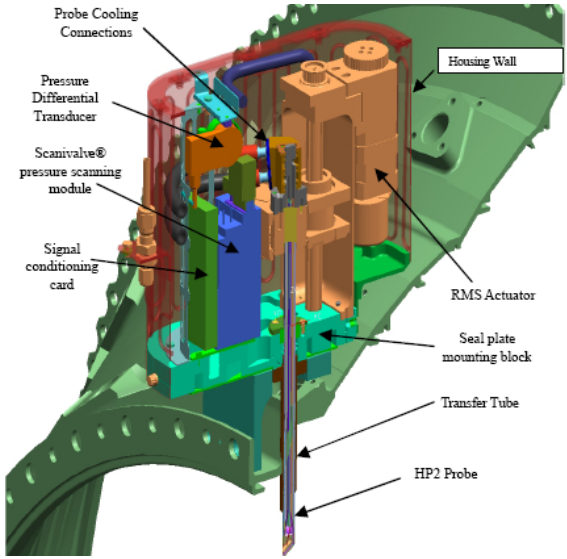

Figure 2.16: Traverse system mounted on engine, Anderson et al. [4], 2008

The probe tip incorporating a Platinum/Ruthenium shield, a thermocouple and pressure tappings is shown in Figure 2.17 together with the end of the central dividing plate extending through the probe stem separating incoming and returning coolant. As in their design process, local

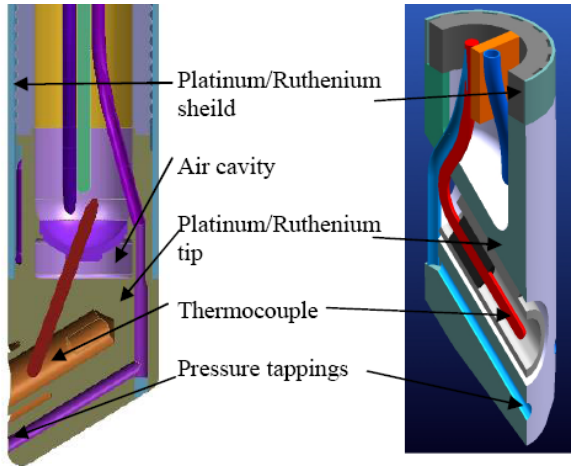

Figure 2.17: Cooled pneumatic 3-hole probe, probe tip cross section showing the Platinum/Ruthenium tip and shield, Anderson et al. [4]

hot-spots creating local boiling have been identified, a hemi-spherical guide has been electron-beam welded inside the probe tip creating an air cavity and hence a thermal insulation between the platinum probe tip and the cooled stem. Although the platinum probe tip is below the critical temperature, the mechanical strength has been found to be insufficient necessitating the use of a Platinum/Ruthenium alloy.

Recently, Cambridge University has revived the tare measurement technique introduced and successfully utilized by Grey [26], shown in Figure 2.10, in order to develop a high temperature intermittent aspirated probe for pressure and temperature measurements. The probe built, shown in Figure 2.18, with a head diameter of 6 mm and stem diameter of 12 mm is operated intermittently in stagnation and aspiration phases to measure total pressure and derive total temperature respectively. A laboratory temperature capability of 1800 K has been demonstrated by Yang et al. while the maximum temperature of the probe designed for engine environments is limited to 1300 K. In order to extend this limit, a cooled probe design is being developed. A detailed description of this technique is presented by Massini et al. [50].

Figure 2.18: Intermittent aspirated probe head [50]

2.2.2.3 High-Frequency Pressure Probes

An early example of a high-frequency pressure probe is the water-cooled transient pressure probe presented once again by Grey in 1970 [26], designed for rocket nozzle detonation measurements, where high-frequency combustion instabilities were of interest. The probe having a size of Ø9.5 mm shown in Figure 2.19 incorporated a Ø5.6 mm piezo-electric crystal pressure transducer with a quoted natural frequency of 400 kHz surrounded by Ø0.51 mm cooling jets blowing directly onto the transducer diaphragm which is covered with an ablative layer allowing emergency protection in case of any malfunction of the cooling jet scheme. It is claimed that this design provides effective cooling of the transducer, without sacrificing the frequency response while providing full-protection against drift-producing temperature changes. Unfortunately, no measurement results have been presented.

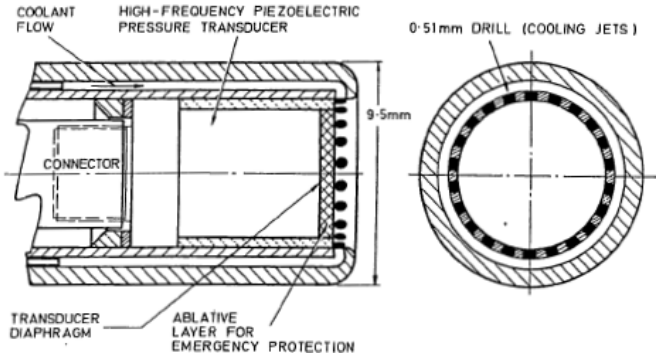

Figure 2.19: High frequency transient pressure probe, Grey [26]

Moore presented a fast-response (100 Hz – 10 kHz) water cooled pressure probe, shown in Figures 2.20 and 2.21, for acoustic measurements in high temperature flows such as jet-pipes in 1977 [54]. Miniature pressure transducers mounted on a Ø½" (∼Ø12.7 mm) probe with their sensing surfaces flush-mounted parallel to the flow are maintained at temperatures below 400 K by using ordinary tap water pressurized to approximately 3 bars flowing at a rate of 0.143 ℓ/min with the probe immersed in a high temperature gas stream of 2 bars and approximately 1250 K.

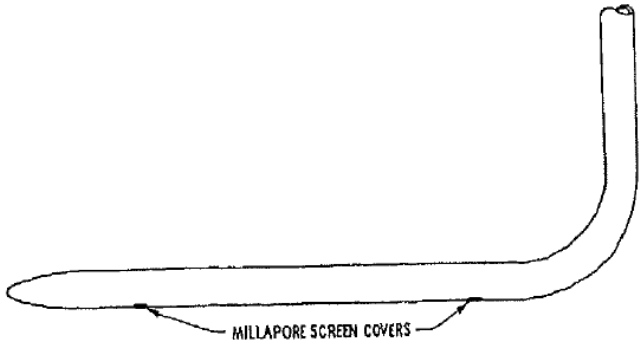

Figure 2.20: Cooled probe external configuration, Moore [54], 1977

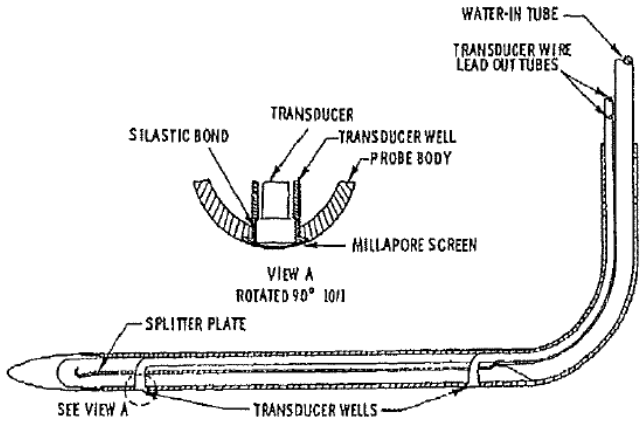

Figure 2.21: Cooled probe internal configuration, Moore [54], 1977

Aimed at turbine blade cooling studies, Larguier presented a fast response cooled probe with a quoted frequency bandwidth of 500 kHz, shown in Figure 2.22, in 1985 [46]. The cylindrical probe tip sized Ø4 mm, incorporates a Ø0.8 mm pressure hole parallel to the flow direction located 6 mm aft of the nose. An elastomer, good at transmitting high-frequency pressure fluctuations, is employed as a thermal barrier between the measurement location and the sensor diaphragm. The probe is cooled using water in order to maintain the piezoelectric ceramic below the Curie temperature, above which the piezoelectric properties of the ceramic is lost. A thermocouple is employed in the design to ensure the Curie temperature is not exceeded. A measurement capability of 1000 K has been demonstrated using this probe.

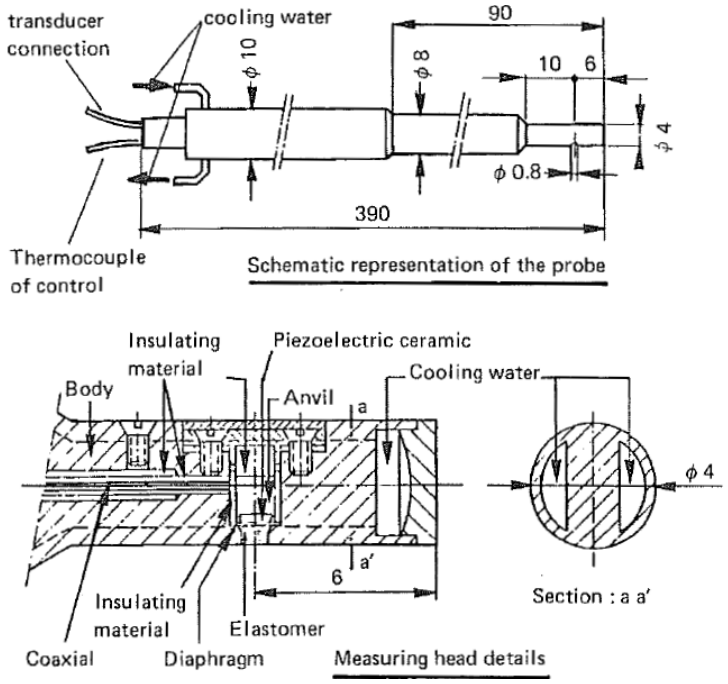

Figure 2.22: High temperature unsteady pressure probe equipped with a miniaturized measuring head developed for the wake analysis of turbine rotor blades (all dimensions in mm), Larguier [46], 1985

2.3 Summary

Summarizing the available literature, several high temperature sensors employing either piezoelectric crystal technology or Fabry-Pérot interferometry technique have already reached a temperature capability of 1200-1300 K. However, the sheer size of these sensors limit their use to only wall measurements. Concerning piezo-resistive sensors have reached a temperature capability above 850 K, which approaches the material limit used in fabrication of such sensors. On the other hand, sensor packaging still remains a challenge for employment of these sensors in probes that may reach such high temperature levels. Although some studies have been done on cooled piezoresistive sensors, due to the fact that their temperature capabilities don't exceed that of uncooled high-temperature sensors such as piezoelectric sensors and the similar dimensions to such sensors, they have gained wide spread. Fast immersion technique, where a sensor of lower temperature capability than the measurement environment is quickly inserted and taken back out before critical temperatures have been reached also is not favored as the immersion times are far inferior to sensor stabilization times, yielding unusable readings. Concerning fast-response cooled probe designs, most of the applications are limited to a few kHz. One interesting example presented by Larguier has demonstrated a probe of 4 mm head diameter reaching temperature levels around 1000 K. However this temperature is still far below the levels typically found in the hot sections such as the combustion chambers and turbines of modern gas turbine engines.

Chapter 3

Design Requirements and Probe Concept

3.1 Probe Concept

In order to acquire statistically representative data to determine both periodic and random pressure fluctuations using tools such as phase locked averaging, a probe for continuous immersion in the hot gas-path is required.

As a high bandwidth sensor, operating at temperatures above its survivability limit, has to be employed to achieve this goal, a cooled probe design is necessary.

The conceptual design of the cooled probe, shown in Figure 3.1, is based on an arrangement of two co-centric tubes creating feed and return lines (i.e. an inner cylinder for feed, and an outer annular jacket for return), forcing the coolant to flow through a passage near a cylindrical piezo-resistive pressure sensor placed transversally to the probe shaft axis.

As illustrated in Figure 3.2, by incorporating a protective screen for the sensor within a housing, again in a co-centric tube arrangement, the sensor may be cooled via convection around its circumference, while the screen employed is cooled via conduction.

Keeping the complexity of the assembly in mind, priority is given for obtaining the smallest achievable probe head diameter, which is determined to be Ø8 mm as will be justified later.

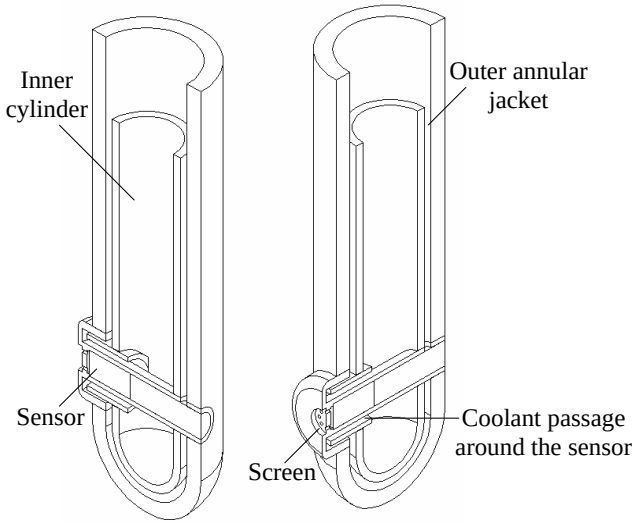

Figure 3.1: Fast response cooled total pressure probe concept

3.2 Heat Load Conditions

The highest temperature levels in turbomachinery flows are found in combustors and high-pressure turbine stages, where measurements of the flow-quantities are extremely difficult to accomplish. The latest engines are providing compressor delivery pressures as high as 55 bar, corresponding to turbine inlet pressures of above 50 bar and HPT outlet pressures above 20 bar at take-off conditions. Typical conditions for modern turbofan engines given by the European Virtual Institute for Gas Turbine Instrumentation (EVI-GTI) are presented in Figure 3.3. As it may be seen, turbine-inlet temperatures (TIT) are as high as 2100°C or $\sim$2400K.

Concerning gas path measurements, using probes above the melting point or the re-crystallization temperature of most metals and alloys, the only viable option is to employ cooled probes. The high heat-flux into the probe immersed in the hot gas-path is due to the combination of high temperature, high pressure and hence density and high turbulence levels emanating from swirlers used for mixing in combustors and

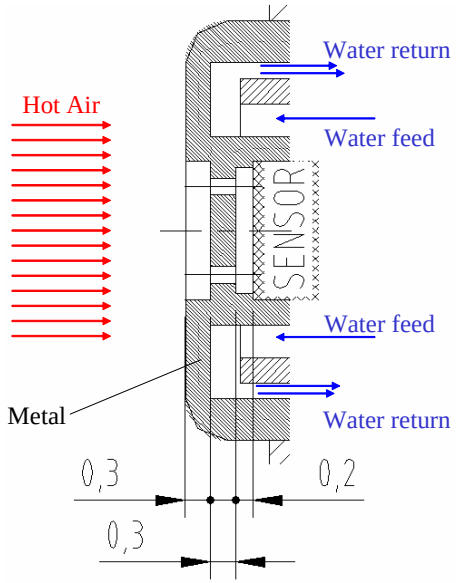

Figure 3.2: Sensor head and screen cooling configuration

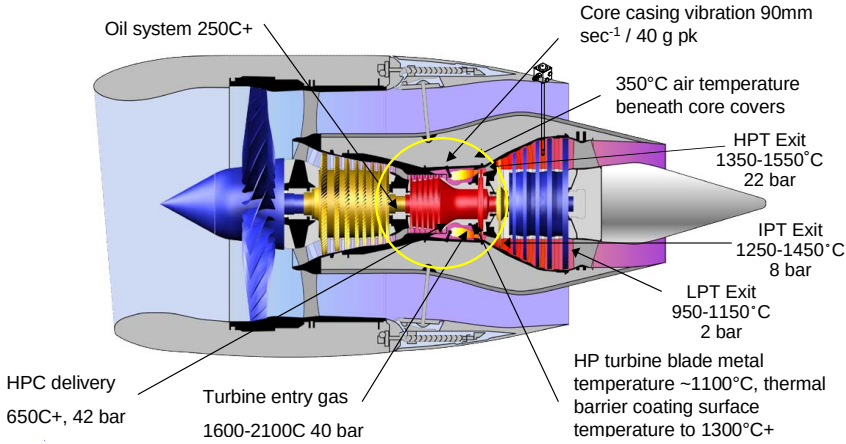

Figure 3.3: Pressure and temperature conditions in a modern turbofan engine [19]

blade passing events for turbines. In cases where probes are subjected to flames, radiation heat transfer also becomes important in addition to the conjugate heat transfer which includes conduction and forced convection. In addition, for a meridionally uniform flow, the amount of heat collected by a probe is proportional to the immersion depth, as well as the probe material affecting conduction, geometry affecting convection and surface coatings employed affecting both conduction and radiation heat transfer.

Considering the complicated nature of the measurement environment, where a catastrophic failure is unavoidable in case of a cooling system malfunction, it is crucial to have an accurate estimate of the heat transfer into a probe for cooling system sizing and assessment.

Among various geometries such as wedges, etc., cylindrical probe geometries are favored for various reasons. In the case of an unsteady flow-field with a high variance of flow angle with respect to both time and space, the flow around a cylinder does not essentially change, decreasing the aero-elastic loading on the probe to a minimum. Moreover, dynamic stall characteristics of a cylindrical probe is far superior to those of other geometries, which can not recover after the onset of stall, yielding incorrect measurements.

The external heat transfer into the probe has been estimated using various correlations linking Nusselt and Reynolds numbers for a cylinder in cross-flow. A detailed review of the correlations developed for a cylinder in cross-flow is presented by Morgan [55]. However, many correlations do not include the effect of turbulence intensity, having a substantial influence on the heat transfer as shown by Moss and Oldfield [71]. The turbulence intensity or the tubulence level, defined as the ratio of velocity fluctuations to mean velocity level, may reach values as high as 15% at the combustion chamber exit [61]. The correlations considered in the present study are those which are probably the most widely used within the gas turbine heat transfer community, namely: Smith & Kuethe [70] in eq. (3.1), Kestin & Wood [34] in eq. (3.2), Lowery & Vachon [47] in eq. (3.3), Zukauskas & Ziugzda [77] in eq. (3.4) and Zukauskas [76] in eq. (3.5).

$$\overline{Nu_d} = Re_d^{0.5}\left(1 + 0.0277(1 - e^{-2.91\times10^5 Re_d})(TuRe_d^{0.5})\right) \tag{3.1}$$

$$\overline{Nu_d} = Re_d^{0.5}\left(0.945 + 3.48\left(\frac{TuRe_d^{0.5}}{100}\right) - 3.99\left(\frac{TuRe_d^{0.5}}{100}\right)^2\right) \tag{3.2}$$

$$\overline{Nu_d} = Re_d^{0.5}\left(1.010 + 2.64\left(\frac{TuRe_d^{0.5}}{100}\right) - 3.070\left(\frac{TuRe_d^{0.5}}{100}\right)^2\right) \tag{3.3}$$

$$\overline{Nu_d} = 0.068\left(\frac{Re_d\pi}{2}\right)^{0.73}\left(Tu^{0.17}\right)\left(Pr_g^{0.4}\right)\left(\frac{T_g}{T_{wall}}\right)^{0.12} \tag{3.4}$$

$$\overline{Nu_d} = CRe_d^m Pr_g^n\left(\frac{Pr_\infty}{Pr_s}\right)^{\frac{1}{4}} \tag{3.5}$$

The effect on the calculated heat flux by using the different correlations is shown in Figure 3.4. The highest convection rate is estimated by the relation of Smith & Kuethe. However, this model together with the model of Zukauskas are not validated for a wide range of Reynolds and Mach numbers limiting their applicability. For instance, the relation by Smith and Kuethe is valid only for incompressible flows, where the relation by Kestin and Wood has only been validated at three Reynolds numbers (75,000, 100,000 and 125,000), the highest of which is approximately one third of the desired level. The model by Lowery & Vachon has been validated for Reynolds numbers up to 302,000 at values of turbulence intensity from 0.40 to 14.20 per cent, given in eq. (3.3), has therefore been selected for estimating the average Nusselt number around the probe. The perfect agreement between the three models is worth mentioning although they are not shown to be valid in the applied conditions. As it can be seen in Figure 3.4, the heat flux experienced by the probe reaches values in excess of 2 MW/m^2 above 1250 K.

In addition to the heat transfer, other considerations pose many constraints on the design of a new probe for testing in real gas turbines. In an environment where the temperatures outside the core engine casing and the by-pass liner are of the order of 700 K, with additional spacing constraints and with the added complexity of having to use existing access ports, the probe sizing is a cumbersome process in which not only

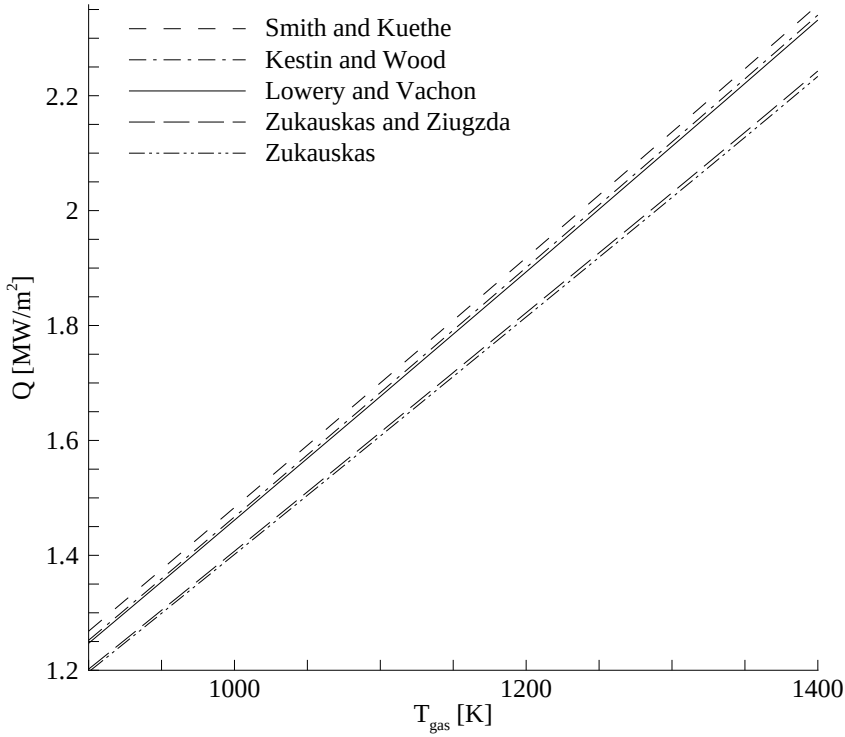

Figure 3.4: Comparison of heat flux evolution as a function of gas temperature using different Nusselt number correlations, P_o = 40 bar, M = 0.5, Tu = 15%, probe diameter = 8 mm, immersion depth = 27 mm

the probe, but also the utilities forming the system have to be considered.

3.3 Design Objectives

The primary objective of this design study has been determined as the assessment of the feasibility of a probe concept based on the following requirements:

- The measurement of both steady and unsteady components of the gas path total pressure with high accuracy (defined per application) and high signal-to-noise ratio
- The measurement of both periodic (by phase-locked averaging (PLA) over several blade passages or rotor revolutions) and random fluctuations
- The highest possible frequency bandwidth, ideally up to 100kHz.
- The smallest possible probe head size for optimum spatial resolution and minimal flow disturbance
- A high robustness and reliability of design considering the extremely harsh conditions of the hot turbine environment and the requirement of engine integrity.

Chapter 4

Probe Design

4.1 Pressure Sensor

The sensor selection depends on many parameters such as the measured quantity, size and environmental capabilities. The requirement to measure both the steady and unsteady components (i.e. DC and AC) favors the use of piezo-resistive sensors. Concerning the temperature capability, piezo-electric sensors are proven to be operable at higher temperatures compared to piezo-resistive sensors. However, the required diaphragm diameter, at the order of 4-6 mm, in order to obtain the sensitivity required prevents the use of such sensors in a fast-response cooled probe.

For designing the cooled probe, a commercial off-the-shelf high temperature silicon-on-insulator (SOI) ultra-miniature Kulite piezo-resistive sensor (XCE-062), shown in Figure 4.1, with operating temperatures ranging from 218 K to 546 K, and with a temperature compensation between 298 K and 508 K, is selected.

The XCE-062 series offer very small packaged sensor dimensions (2 mm in length and 1.6 mm in diameter). The high signal-to-noise ratio, and wide pressure range options from 0.35 to 70 bar are other factors for the choice. The SOI sensor is rated for 546 K limited by the polytetrafluoroethylene (PTFE, commercially known as Teflon) lead insulation material, while the sensor chip itself can sustain temperatures as high as 773 K.

These sensors are either coated with room-temperature vulcanizing (RTV) silicone elastomer or covered with metal screens for protection against

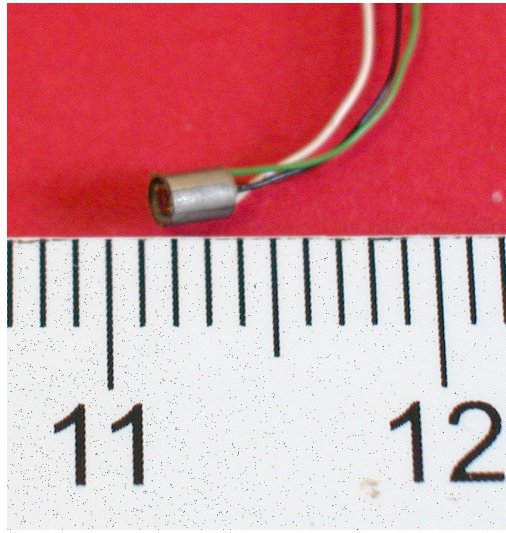

Figure 4.1: Photograph of the selected Kulite XCE-062 series ultra-miniature pressure transducer

foreign object damage (FOD). However, the sensor chosen for this application is maintained in its bare form in order to achieve the highest possible frequency response and is protected with a perforated screen integrated to the probe, which is cooled together with the probe body as shown in Figure 3.2.

As the operating principle of the piezo-resistive pressure sensor is based on measuring the bridge imbalance due to tension and compression of four resistors, illustrated in Figure 4.2, bonded onto a diaphragm, the sensor not only responds to pressure but also to temperature changes as the electrical resistivity is a function of temperature. Passive compensation modules based on the knowledge of this resistivity-temperature behavior of the resistor material employed are supplied with commercial sensors to overcome this problem. However, a basic static calibration at various temperature levels revealed that the passive compensation module is not effective in maintaining zero measurand output (i.e. offset) while proving effectiveness in maintaining sensitivity.

In lieu of a passive compensation module, an active scheme using a dif-

ferent amplifier topology allowing real-time temperature monitoring by the aid of a *sense* resistor placed in series to the Wheatstone bridge as described by Ainsworth [1] is employed. This amplifier circuit, incorporating a sense resistor equivalent to the bridge resistance is shown in Figure 4.2. As neither the offset nor the sensitivity is compensated for temperature changes in this scheme, a full calibration map in both temperature and pressure for the whole measurement range is required. On the other hand, the temperature output indicating the bridge temperature provides a means to assess the cooling system effectiveness.

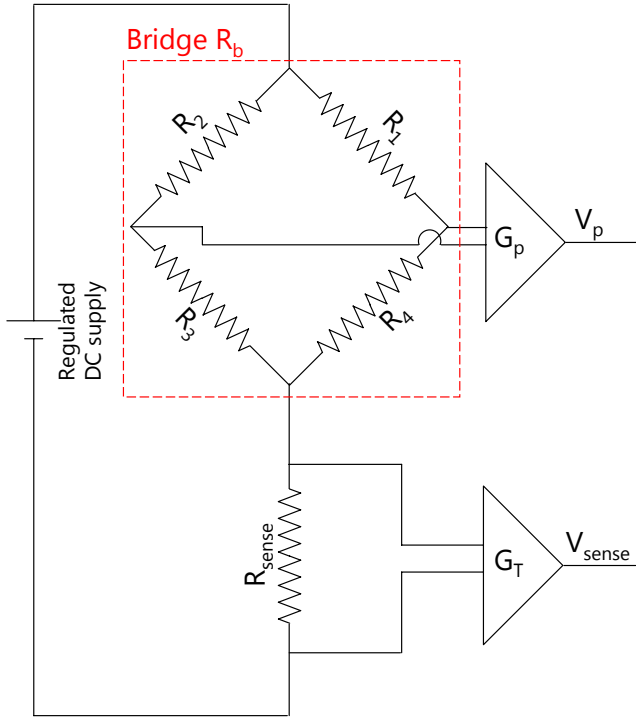

Figure 4.2: Active compensation amplifier circuit diagram incorporating a sense resistor

4.2 Aerodynamic Design

4.2.1 Probe Sizing and Geometry

The aerodynamic design process of fast-response aerodynamic probes essentially differs from that of steady-state probes. For instance, during the design of a pneumatic pressure probe, the steady state qualities are regarded resulting in different geometries such as L-shaped probes, wedge probes, etc. As explained by Gossweiler [24], the measurement quality of fast-response probes depends on a number of dynamic characteristics, which in turn are directly related to the probe size and geometry.

As an example, a wedge probe instrumented with high bandwidth sensors may be considered. Even though the wedge probe performs considerably well in determining the flow angle in steady-state flows, its performance is far from being adequate in unsteady flow conditions as separated regions occur on the wedge surfaces with fluctuating flow angles. These separated regions also induce dynamic structural loading resulting in vibrations.

The parameters determining the aerodynamic design process may be gathered under two groups as steady-state (static) and unsteady (dynamic) characteristics.

For a total pressure probe, static considerations include angular insensitivity range (i.e. the angular range in which true total pressure is measured), Mach and Reynolds number effects, turbulence effects, velocity gradient effects and finally blockage effects. Minimizing the probe size is the key in reducing these undesirable effects. As there is little room to improve these characteristics, an ideal probe being far from reality, most of these effects are taken into account with the aid of aerodynamic calibrations.

Considering dynamic aspects, the prominent characteristic is the frequency response, which is explained in section 4.2.2. On the other hand, one has to consider unsteady aerodynamic loading and dynamic stall as explained above in the example of a wedge probe together with other factors such as vortex shedding interactions. Cylindrical probe

geometries have been shown to be the least sensitive to those unsteady effects. Furthermore as explained by Brouckaert [7], total pressure measurements are far less affected by the corresponding aerodynamic errors compared to the directional (side-sensor) pressure measurements such as in case of unsteady flow-angle measurements by multi-sensor probes.

4.2.2 Frequency Response

In order to fully exploit the bandwidth of a sensor in Pitot-type or cylindrical probes, a flush-mounted arrangement is the best solution without any doubt. However, it is important to bear in mind the fact that the acquired data does not represent true flow-field due to the presence of pressure gradients on the surface of a sensor diaphragm.

In order to remedy the pressure gradient problem, sensors are slightly retreated from the apex as shown in Figure 4.3, which also improves angular insensitivity at the expense of reducing the frequency bandwidth.

It is worth mentioning that there is no agreement or straight-forward method in quantifying this retreat. Among several retreat-to-diameter ratios mentioned, Epstein [18] suggests a value of 1, while Larguier [45] suggests a value of 0.5. The most recent value given by Sieverding et al. [67] suggests a retreat-to-diameter ratio from 0.2 to 0.3. In the present design, the cooled protective screen is retreated by 0.3 mm as seen in Figure 3.2. Given that the sensor diameter is 0.062" ($\sim$1.6 mm), the retreat-to-diameter ratio obtained is nearly 0.19 in order to minimize the bandwidth loss while still maintaining a good angular response, i.e. to have a flat region above $\pm 5^{\circ}$ in angular calibration pressure recovery is above 99% which is explained later in section 6.1.3.

The cooled protective screen incorporated in the probe comprises 8 holes of 0.3 mm diameter. In order to calculate the frequency response of the assembly, the line-cavity theory of Bergh & Tijdeman [6] is utilized by assuming a line using an equivalent diameter obtained by calculating the total area of the 8 holes on the screen. The transfer function obtained is presented in Figure 4.4 and calculated for two other cavity lengths

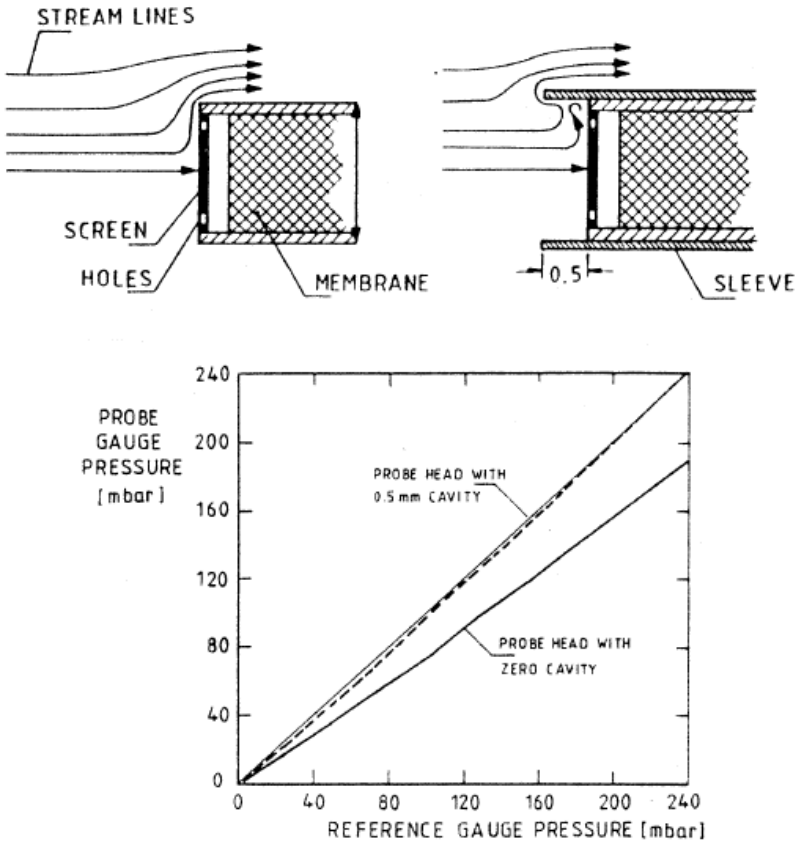

Figure 4.3: Effect of transducer retreat on total pressure reading, Sieverding et al. [67], 1995

taking into account the small recess of the sensor with respect to the sensor housing.

The sensor head designed, shown in Figure 3.2, is manufactured for experimental validation purposes before the probe design is finalized. Validation tests carried out in the VKI shock-tube facility, presented in Figure 4.5, shows good agreement between the line-cavity theory and

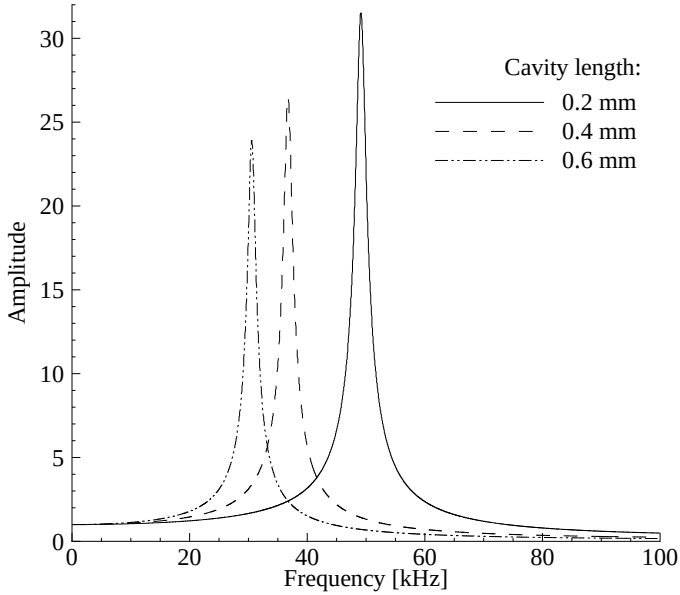

Figure 4.4: Comparison of the theoretical transfer functions for different cavity lengths for the frequency response of the screen-cavity configuration

experimental results.

The line-cavity resonance, shown in Figure 4.4, is found to be around 50 kHz, yielding a flat frequency response until 20 kHz. On the other hand, as also noted by Ivey & Ferguson [32], the Helmholtz equation, given in eq. (4.1), indicated that the line-cavity resonance frequency is proportional to the speed of sound, which is a function of gas temperature. In other words, the resonance frequency increases with increasing gas temperature in the recess cavity as shown in Figure 4.6.

$$f_n = \frac{a}{2\pi}\sqrt{\frac{\pi d^2}{4LV_c}} \tag{4.1}$$

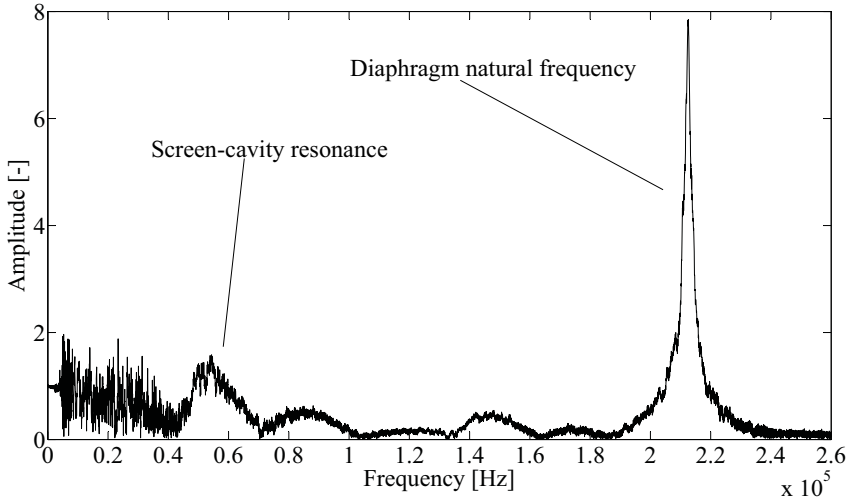

Figure 4.5: Experimental transfer function from the shock tube tests for the frequency response of screen-cavity configuration

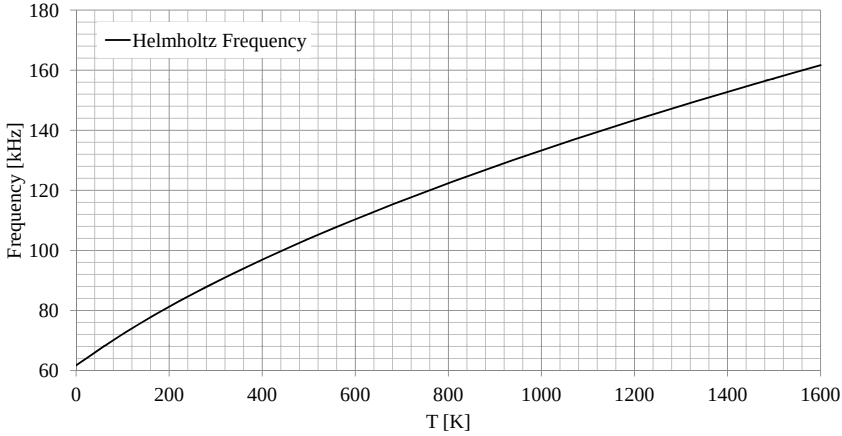

Figure 4.6: Variation of Helmholtz frequency with respect to temperature as given in eq. (4.1)

4.3 Probe Cooling

4.3.1 Parametric Study - One Dimensional Model

The heat balance around the cooled probe design depends on a wide array of parameters. In addition to flow-parameters such as pressure, temperature, Mach and Reynolds numbers, turbulence level and gas properties; other factors such as probe size (i.e. length and diameter), radial immersion depth, probe wall thicknesses and materials, coolant properties (i.e. temperature, pressure, viscosity, conductivity and flow rate) have to be carefully taken into account for cooling performance assessment.

The choice of the coolant fluid, whether it is a refrigerant, distilled water, oil or a gas such as air, also adds complexity to this process.

In order to avoid the complexity of three-dimensional Navier-Stokes simulations for design purposes, parametric studies are favored for determining the optimum configuration.

In an effort to achieve both fast and good estimations of the global thermal parameters, to optimize the configuration for a given measurement case and to assess the performance of a given probe configuration under various flow conditions, a one-dimensional model is developed in MATLAB.

Water is the coolant of choice due to its high specific heat capacity and incompressibility as well as being harmless. Additionally, it is possible to pressurize the probe internally using water which is safe in case of a leak due to its incompressibility although not preferred by engine manufacturers. Internal pressurization also decreases structural stresses on the probe walls while increasing the coolant boiling point as shown in Figure 4.7.

The one-dimensional tool solves the heat balance at interfaces which are basically the wall boundaries. The Nusselt number relation explained in section 3.2 by Lowery & Vachon, given in eq. (3.3) is used to estimate the convection at the gas-external wall boundary. In addition to the

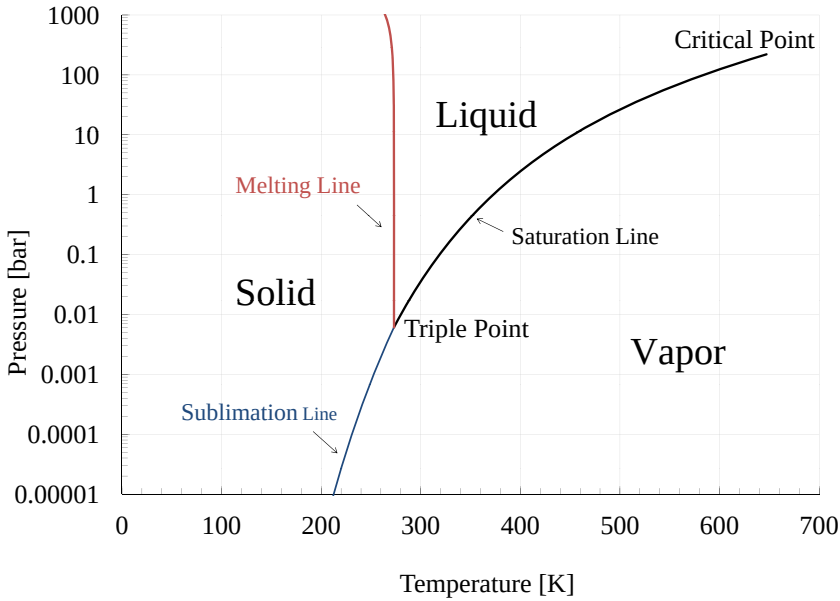

Figure 4.7: Phase diagram of Water [72]

conduction heat transfer through the metallic probe walls, the *Dittus-Boelter* equation [17], given in eq. (4.2), is used to solve for the convection heat transfer at the water-wall boundaries.

$$\overline{Nu_d} = 0.023 Re_d^{\frac{4}{5}} Pr^n = \frac{\overline{h_1} d}{k_w} \tag{4.2}$$

In eq. (4.2), values of n =0.4 for heating and n =0.3 for cooling should be used. The equation is valid for turbulent flows in circular tubes and it has been experimentally confirmed for the range of conditions where $Re_d > 10000$, $0.7 \leq Pr \leq 160$, $l/d > 10$. As a first approximation, the Dittus-Boelter equation may be used to obtain a reasonable estimate of the average Nusselt number, $\overline{Nu_d}$, by evaluating the fluid properties at the arithmetic mean of the coolant feed and return temperatures, which is: $\overline{T_w} = (T_{w_{in}} + T_{w_{out}})/2$.

The model is based on the assumption that the probe body is a tubular counter-flow heat exchanger as shown in Figure 4.8. Blockage by the wire harness is denoted with $\varnothing_{bl}$, while the walls are enumerated from the innermost metallic wall to the outermost layer representing a TBC layer.

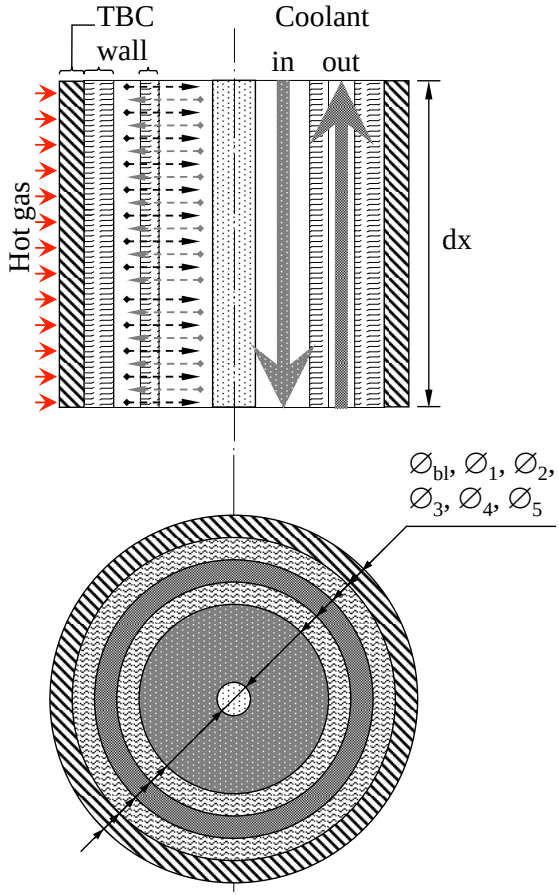

Figure 4.8: Schematic representation of the 1-D model theory

The schematic representation of the heat flow is given in Figure 4.9. While the outer gas temperature is denoted by T_g, the wall temperatures are denoted by T_{p_j}, j being the wall index as explained above,

with section 4-5 representing the optional thermal barrier coating (TBC) layer.

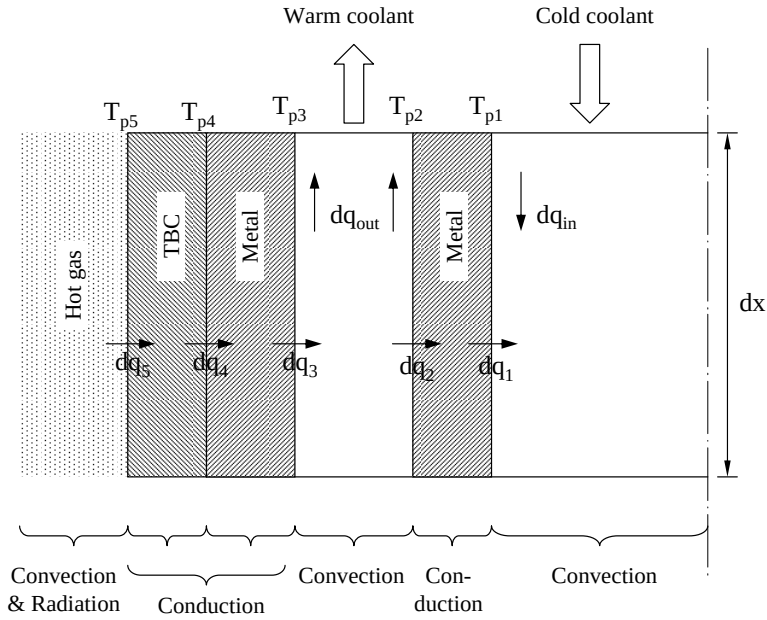

Figure 4.9: Schematic representation of the heat flow through the probe

The heat exchange in the vicinity of the sensor is not modeled, which implies that the sensor temperature is also not modeled. Instead, the coolant temperature at the sensor location, T_{ws} is calculated, which is lower than the actual sensor temperature by definition. The probe length is denoted by L and the whole heat balance written for an incremental length dx is therefore integrated in order to reach global values. While the wall temperatures are assumed to be uniform, the heat transfer is assumed to be in the normal direction to the surfaces, neglecting the axial heat transfer along the probe length. Contact resistance (i.e. between the TBC layer and the probe outer wall) is also neglected.

Writing down the heat transfer scheme given in Figure 4.9, one obtains the set of equations given in eqs. (4.3) to (4.5).

$$dq_5 = dq_4 = dq_{out} - dq_{in} \tag{4.3}$$

$$dq_5 = dq_4 = dq_3 = dq_2 + dq_{out} \tag{4.4}$$

$$dq_2 = dq_1 = dq_{in} \tag{4.5}$$

For a hollow cylinder with convective surface conditions, having inner and outer diameters of d_1 and d_2 with surface temperatures of T_{s_1} and T_{s_2} respectively, for steady-state conditions with no heat generation, one may obtain the expression given in equation (4.6) for the heat transfer rate, by combining the heat equation and Fourier's law in cylindrical coordinates, as thoroughly explained by Incropera and DeWitt [29].

$$q_r = \frac{2\pi Lk(T_{s_1} - T_{s_1})}{ln\left(\frac{d_2}{d_1}\right)} \tag{4.6}$$

By expanding eqs. (4.3) to (4.5) using eq. (4.6) and then combining, equation (4.7) is obtained.

$$\begin{aligned} dq_5 = h_g \pi d_5 dx(T_g - T_{p5}) = \frac{2\pi k_{TBC} dx(T_{p5} - T_{p4})}{\ln d_5/d_4} = \\ = \frac{2\pi k_o dx(T_{p4} - T_{p3})}{\ln(d_4/d_3)} = h_3 \pi d_3 dx(T_{p3} - T_{out}(x)) \end{aligned} \tag{4.7}$$

It is important to note that the term T_{out} represents the outlet temperature of the infinitesimal element with a length dx as shown in Figure 4.9. For the sake of simplicity, the common term dx in all equations is dropped, and two variables are defined as shown in eqs. (4.8) and (4.9).

$$\alpha = \frac{2\pi k_{TBC}}{\ln(d_5/d_4)} \tag{4.8}$$

$$\beta = \frac{2\pi k_o}{\ln(d_4/d_3)} \tag{4.9}$$

By substituting the two new variables in eq. (4.7), eq. (4.10) is obtained.

$$\begin{aligned} &h_g d_5(T_g - T_{p5}) = \alpha(T_{p5} - T_{p4}) \\ &= \beta(T_{p4} - T_{p3}) = h_3 d_3(T_{p3} - T_{out}) \end{aligned} \tag{4.10}$$

Rearranging eq. (4.10) into a system of equations, given in eqs. (4.11) to (4.13), the surface temperatures starting from the outer gas temperature T_g may be computed.

However, the conductivity and convective heat transfer coefficient values are dependent on temperature and pressure. So as new temperature values are obtained, an iterative approach has to be followed in order too obtain correct results.

$$h_g d_5 T_g - h_g d_5 T_{p5} = \alpha T_{p5} - \alpha T_{p4} \tag{4.11}$$

$$\beta T_{p4} - \beta T_{p3} = \alpha T_{p5} - \alpha T_{p4} \tag{4.12}$$

$$\beta T_{p4} - \beta T_{p3} = h_3 d_3 T_{p3} - h_3 d_3 T_{out} \tag{4.13}$$

The heat balance representing the probe, and not an infinitesimal length, is obtained by multiplying eqs. (4.11) to (4.13) with L. T_{out} is the average of the water temperature near the sensor (at the probe tip) and the outlet water temperature. Hence the problem is reduced to obtaining the outlet water temperature and the water temperature near sensor.

Recalling eqs. (4.3) to (4.5), the approach demonstrated may be repeated. When the heat balance at the inner side is written, the resultant equations are as shown in eq. (4.14) and eq. (4.15).

$$Q_2 = \frac{\pi L(T_{wout} - T_{win})}{\frac{1}{h_2 d_2} + \frac{1}{h_1 d_1} + \frac{\ln(d_2/d_1)}{2k_i}} \tag{4.14}$$

$$Q_5 = \frac{\pi L(T_g - T_{wout})}{\frac{1}{h_3 d_3} + \frac{1}{h_g d_5} + \frac{\ln(d_5/d_4)}{2k_{TBC}} + \frac{\ln(d_4/d_3)}{2k_o}} \tag{4.15}$$

As explained before, the problem is solved in an iterative manner, starting with an initial T_{ws} guess. Knowing the coolant mass flow rate, the outlet water temperature is calculated using eq. (4.16) and the sensor region water temperature is determined using eq. (4.17).

$$T_{wout} = T_{ws} + \frac{(Q_5 - Q_2)}{\dot{m}_w C_{p_{wout}}} \tag{4.16}$$

$$T_{ws} = T_{win} + \frac{Q_2}{\dot{m}_w C_{p_{win}}} \tag{4.17}$$

In the one-dimensional model, the radiation heat transfer is neglected. Calculation of radiation heat transfer requires the knowledge of the emissivities of both the probe surface and the hot walls, and a view factor which are dependent on the probe properties but also the internal geometry, temperature distribution, base material and coating properties of the test vehicle under consideration.

In order to quantify the importance of radiation heat transfer an order-of-magnitude analysis is required. Using some strong assumptions for the geometry (assumed to be a cylinder) and the emissivities (mean value typical of nickel alloys), an order-of-magnitude analysis has been carried out and the radiation heat transfer is found to be confined within 20 per cent of the convection heat transfer rate. It is important to mention that this analysis has been carried out assuming that the probe is not subjected to flames, which would greatly increase radiation heat transfer rate.

The above given description of the one-dimensional model is valid for a probe with uniform properties from tip to tail. In order to model probes with varying properties along the length, multiple sector capability has been added, enabling the calculation of the probe stem effects and parts of the probe subjected to different conditions, i.e. simulating the probe tip immersed into the gas path (e.g. at 1400 K), and the remaining probe length traversing the hot core engine casing (e.g. at 530 K).

Parametric studies have been performed using the one-dimensional model developed. The coolant flow direction (i.e. whether cold coolant feed through the inner tube or through the outer annular jacket) and the flow

rate have been investigated, leading to the conclusion that feeding the coolant through the inner tube performs better and coolant flow rates of the order of 2ℓ/min are required.

Several Nickel superalloys, typically used for high temperature components in gas-turbines exhibiting excellent mechanical strength and creep resistance at high temperatures, were investigated and discussed in detail in section 5.1. Among these, Nimonic and Inconel alloy families, both developed in 1960s for supporting the development of the Whittle engine, stand out.

Figure 4.10 shows the results obtained using Inconel 600 and 718, Nimonic 75 and copper. The properties are given in Table 4.1, and further discussed in section 5.1. The reason for including copper in the analysis is due to its high thermal conductivity, approximately twenty times that of most high-temperature alloys resulting in wall temperatures approximately 100 K lower than other nickel superalloys presented, even though its mechanical properties are very poor at high temperatures. The better cooling of the copper probe wall results in higher heat extraction and in higher water temperatures, posing a risk of boiling.

	Unit	Copper	Inconel 718	Inconel 600	Nimonic 75
Thermal	[W/mK]	401 @0-100°C	11.4 @20°C	14.9 @20°C	11.7 @20°C
conductivity			24 @800°C	27.5 @800°C	
Tensile strength	[MPa]	224-314	1190 @500°C	570 @500°C	650 @500°C
Melting range	[°C]	1083	1210-1344	1354-1413	1340-1380

Table 4.1: Some properties of possible materials for manufacturing the probe

The effects of immersion depth, thermal barrier coating, heat exchange within the probe stem and heat extracted with respect to the gas temperature are summarized in Figure 4.11.

The reference case is a probe of Ø8 mm made of Inconel 600 with a TBC layer of 0.3 mm, immersed 27 mm into a M=0.5 hot gas stream at 1400 K and 40 bar with a turbulence intensity of 15%, cooled with distilled water at a flow rate of 2ℓ/min. Adding the influence of the heat exchange inside the probe stem of 300 mm long, a slight increase in heat extracted and probe outer wall temperature is observed. On the other hand, a great decrease in the heat transfer through the hot

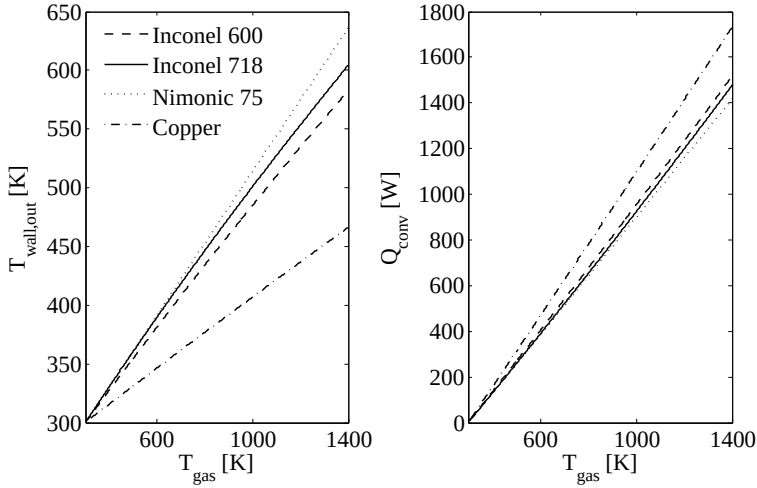

Figure 4.10: Effect of probe material on probe outer wall temperature and heat to be extracted as a function of gas temperature

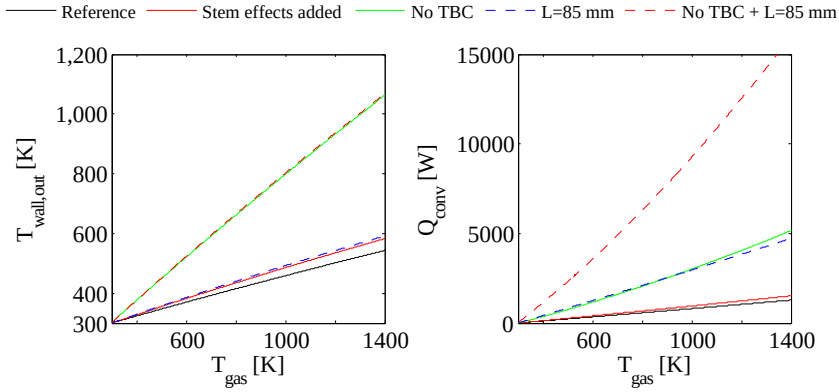

Figure 4.11: Effects of immersion depth, thermal barrier coating, etc. on the outer wall temperature and exctracted heat with respect to gas temperature ($P_o = 40$ bar, $M = 0.5$, $Tu = 0.15$)

gas stream, decreasing the outer wall temperature (T_{p_4}) from 1070 K to 570 K, is predicted with the presence of a thermal barrier coating

(TBC). Without a TBC layer, and for an immersion of 85 mm, as much as 16 kW is extracted from the probe. Finally, it is worth mentioning that the probe length does not have a major influence on the surface temperature but rather on the heat extracted.

In Figure 4.12 effect of turbulence intensity is plotted. As expected, the heat transfer rate and therefore the temperatures rise togethwr with the turbulence intensity, *Tu*. However, the level of rise is small since averaged Nusselt number is calculated, whereas the effect of *Tu* is felt most at the forward stagnation point.

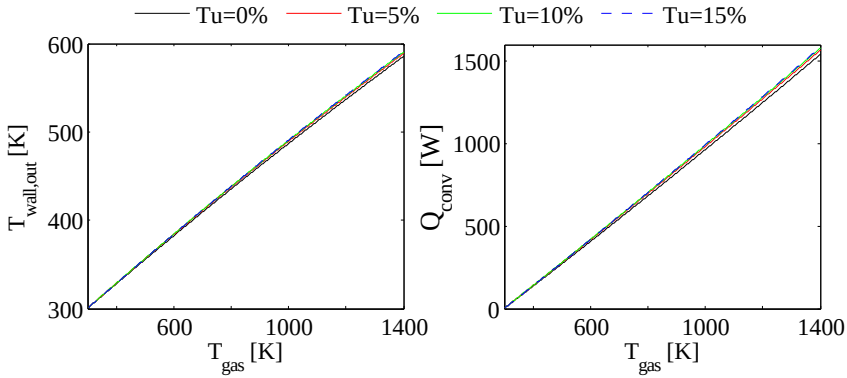

Figure 4.12: Comparison of different turbulence intensity values, using Lowery and Vachon [47] relation

Effect of ambient pressure is also incorporated into the 1D model. As the density of the surrounding gas increases almost proportional to the pressure, the heat transfer rate is effected directly as shown in Figure 4.13. When the ambient pressure is increased from 1bar to 50bars, the heat transfer rate to the probe is almost tripled.

Effect of coolant mass flow rate is presented in Figure 4.14. It is note mentioning that higher the coolant mass flow rate, higher amount of heat can be taken away from the probe, which yields lower surface and water temperatures.

Mach number effects are plotted 4.15. For low Mach numbers, within the incompressible range, the Mach number has a great effect on heat

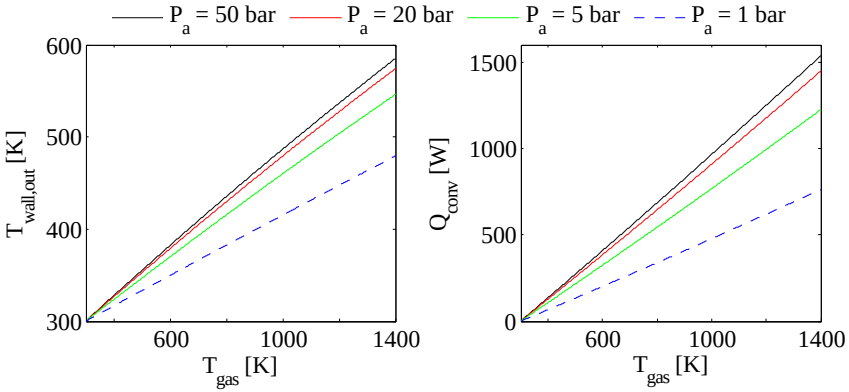

Figure 4.13: Comparison of different ambient pressure values

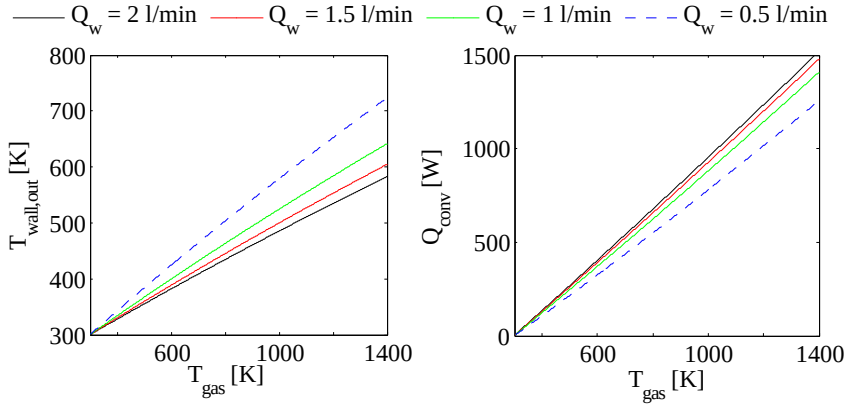

Figure 4.14: Comparison of different coolant mass flow rate values

transfer, where as the compressible regime is achieved, this effect drops considerably. However, one has to note that a very strong assumption is made, which assumes no supersonic pockets or shocks around the probe.

Finally, calculations for test beds that have been used during this study have been presented in Figure 4.16. On Rolls-Royce Viper and Volvo RM-12 low by-pass ratio military turbofan engine, the coolant temper-

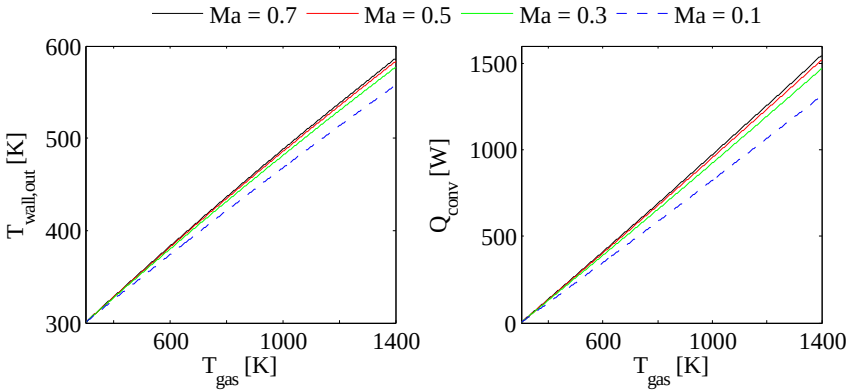

Figure 4.15: Comparison of different flow Mach numbers

ature is taken as room temperature. However on Rolls-Royce Intermediate Pressure (IP) Burner Rig, coolant temperature and mass flow are different, as a cold water supply system exists which can deliver water below 10°C at a mass flow rate higher than 10 ℓ/min.

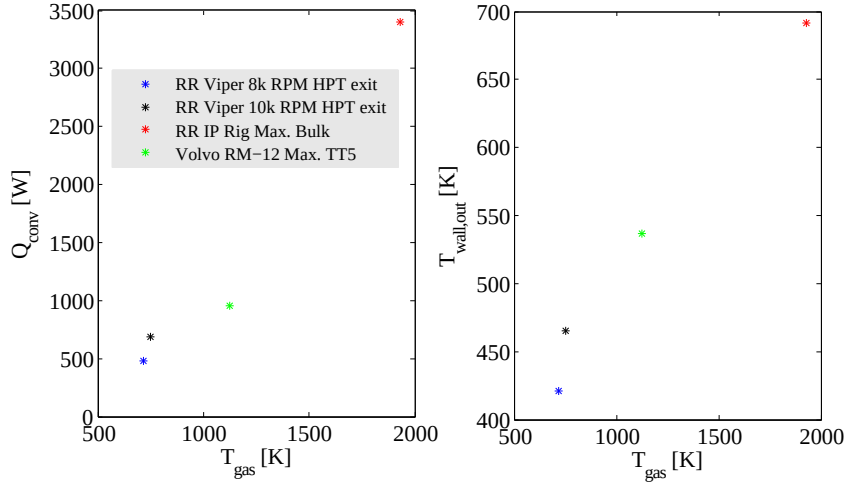

Figure 4.16: 1D solutions on test beds on which the cooled probe is tested

4.3.2 Two-Dimensional Navier-Stokes Computations

Two and three dimensional Navier-Stokes calculations are performed in order to verify the cooling performance predicted by the one-dimensional model developed, to locate and identify possible fluid recirculation or stagnation regions causing local hot-spots and finally to solve for the temperature distribution in the vicinity of the sensor.

The two and three dimensional computational models used in this thesis (i.e. mesh-grid and boundary conditions) have been previously developed at the VKI. For a detailed description of the model, the reader is referred to the report of Pau [62]. However, a short summary is provided in order to complement the results obtained using this model.

The computations were carried out using ANSYS Fluent, with the standard $k-\varepsilon$ model, which is selected due to its robustness, economy and reasonable accuracy for a wide range of turbulent flows, explaining its popularity in industrial flow and heat transfer simulations. Second order upwind discretization schemes have been used to solve the momentum and energy equations.

In order to model the coolant flow in the vicinity of the sensor, a simple two-dimensional planar geometry, shown in Figure 4.17 has been generated, where the sensor axis is normal to the probe axis.

In this two-dimensional model, the external flow-field (i.e the hot gas) is not modeled, requiring the determination of the convective heat transfer coefficient, h_g. In order to reach that goal, the model is initialized using the convective heat transfer coefficient calculated via the probe outer wall temperature obtained from one-dimensional model. The initial calculation using the two-dimensional model results in an updated outer wall temperature, which in turn is fed-back into the model in an iterative manner until convergence is achieved.

As the geometry of the two-dimensional model is not representative of a cylinder in cross-flow, eq. (3.5) may only be used by modifying the constants C, m and n so that they represent a cylindrical plate perpendicular to a cross flow, as explained by Zukauskas [76].

The resulting temperature contour maps and stream-traces shown in Figure 4.17 indicate an effective cooling, with the sensor itself remaining

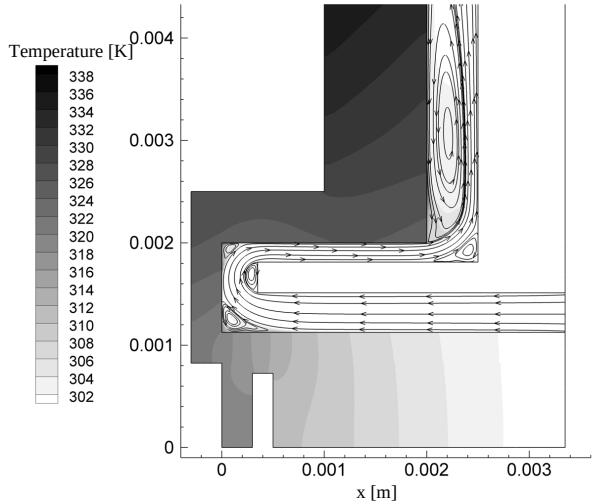

Figure 4.17: 2D planar model of the sensor region, temperature contour plot and stream traces, $T_g = 1400$ K, $M = 0.5$, $P_o = 1$ bar, $h_g = 2600$ W/m^{2}K, coolant flow rate $= 2\ell$/min

below 313 K, for a total gas temperature of 1400 K, $M = 0.5$, $P_o = 1$ bar, $h_g = 2600$ W/m^{2}K and a coolant flow rate of 2ℓ/min. Various recirculation regions do not seem to affect the temperature distribution substantially. In order to improve the cooling effectiveness by avoiding recirculation zones, the original design with sharp corners has been modified with rounded corners inside the return channel, removing sharp edges as shown in Figure 4.18, avoiding corner recirculation zones.

4.3.3 3D Navier-Stokes Computations

The complete three-dimensional probe head is modeled including both the coolant fluid and the metal regions and solving the momentum and energy equations. The computational domain has been split into 112 volumes to facilitate the grid generation around the complex geometry formed by probe tubes and the sensor area. Both structured and unstructured grid elements have been used depending on the complexity

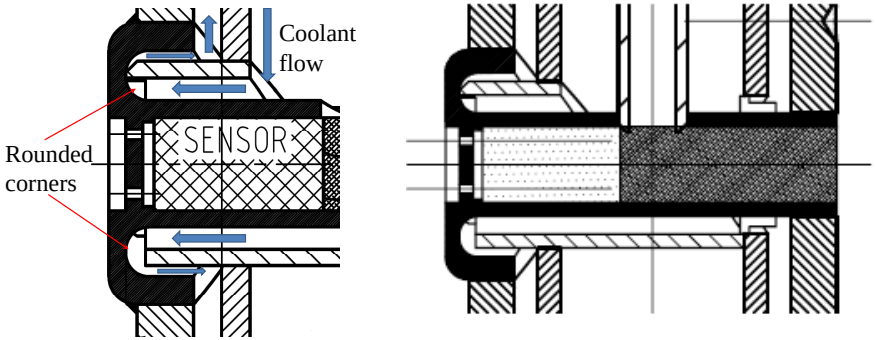

Figure 4.18: Design modification on the screen and the sensor cooling channel with the help of the two-dimensional computations

of the geometry. Approximately 1,496,000 grid cells have been generated in order to simulate the probe head geometry.

In order to reduce the complexity of the simulation, the external flow field has been excluded. The same boundary conditions were applied as described above in the two-dimensional model with a fixed value of the heat transfer coefficient, instead of an iterative approach, calculated using the correlation of Lowery & Vachon given in eq. (3.3) according to the flow conditions.

Temperature contour plots around the sensor for two cases, one with the coolant fed from the annular jacked and the other with the coolant fed from the inner tube, are shown in Figure 4.19 once again for a total gas temperature of 1400 K, $M = 0.5$, $P_o = 1$ bar, $h_g = 2600$ W/m^{2}K and a coolant flow rate of 2ℓ/min.

In both cases (water in from inner tube and from annular jacket), the overall temperature levels remain lower than 380 K and the sensor itself is maintained below 340 K. The highest temperature area is found to be on the outer annulus at the bottom of the probe. The cooling scheme in which water is fed from the internal cylinder is computed to have a lower overall temperature value compared to the case where coolant is fed from the external jacket. The heat flux transferred to the fluid along the inner tube cylinder is lower than that one exchanged with the

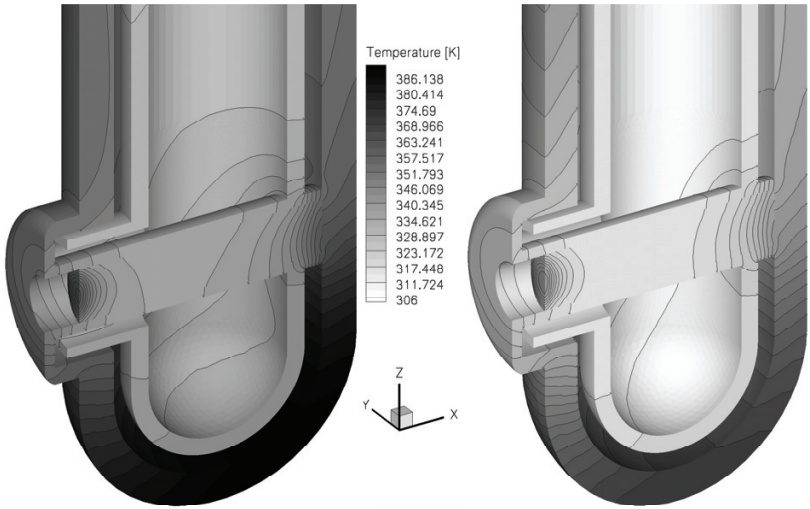

Figure 4.19: Temperature distribution inside probe walls, water inlet from the annular jacket (left) and water inlet from the inner tube (right), $T_g = 1400$ K, $M = 0.5$, $P_o = 1$ bar, $h_g = 2600$ W/m^{2}K, coolant flow rate$= 2\ell$/min

fluid along the external jacket, directly in contact with the hot gas side. Therefore, for the case in which cooling water is fed from the inner tube, where the cold coolant is brought down directly to the sensor header, the sensor experiences a temperature lower than 310K marking a temperature difference as much as 30 K.

4.3.4 Comparison with the one-dimensional model

The results obtained from the one-dimensional model and from the computed full three-dimensional geometry are compared in terms of global cooling parameters. The three-dimensional simulation results are post processed in order to obtain relevant quantities enabling the comparison as explained below.

The water temperature at the outlet of the computational domain has been computed using a mass flow weighted average. The water tem-

perature approaching the sensor has been computed as a mass flow weighted averaged temperature in a horizontal plane located just before the sensor region. The overall heat flux and the probe surface temperatures are computed as integral values on the external probe tube surface. Results have been compared for the case with hot gas free stream temperature and Mach number of 1400 K and 0.5 respectively.

Figures 4.20–4.23 compare the results obtained for different mass flow rates between 0.5 and 2.0 ℓ/min. General agreement is found for the water temperature at outlet shown in Figure 4.20 and for the water temperature approaching the sensor shown in Figure 4.21. A similar conclusion may be drawn for heat extracted from the probe as presented in Figure 4.22.

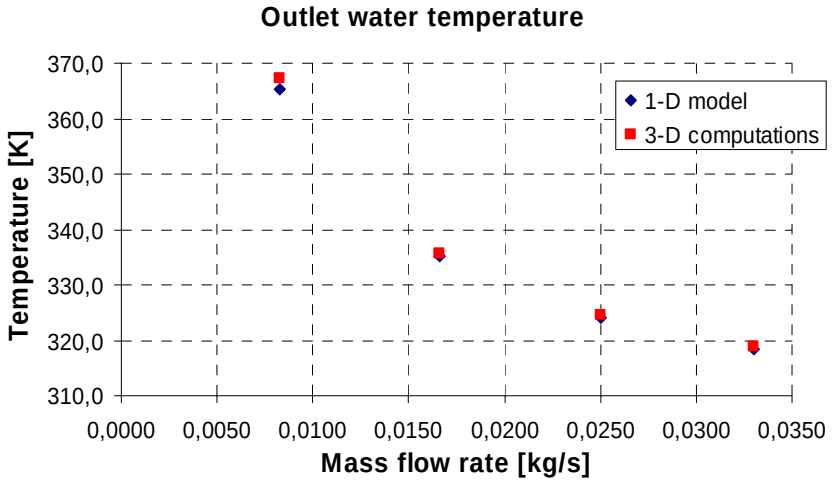

Figure 4.20: Water return temperature as a function of mass flow rate, $T_g = 1400$ K, $M = 0.5$, $P_o = 1$ bar

The one-dimensional model computes generally higher values of the external probe surface compared to the three-dimensional simulations, where the temperature difference is as high as 80 K for a flow rate of 0.5ℓ/min and drops to 20 K for a flow rate of 2ℓ/min as seen in Figure 4.23. This is related to a higher heat flux calculated for the three-dimensional case compared to the one-dimensional model. This is attributed to the fact that in the one-dimensional model the probe is mod-

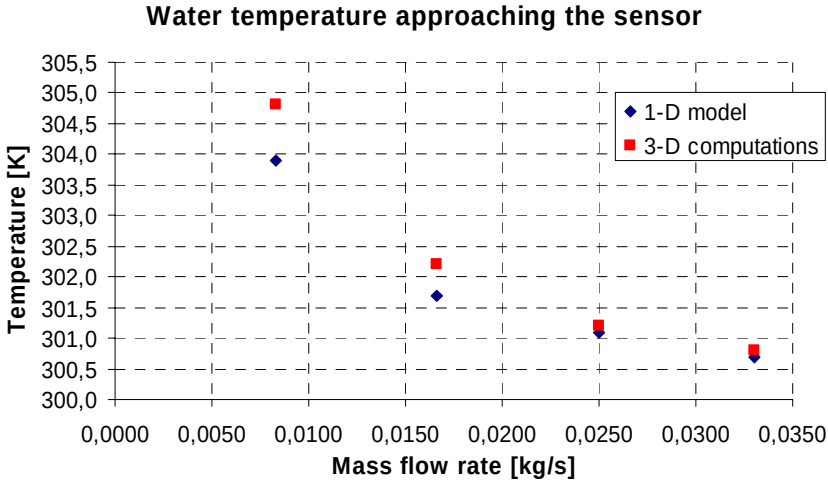

Figure 4.21: Water temperature approaching to the sensor as a fucntion of mass flow rate, $T_g = 1400$ K, $M = 0.5$, $P_o = 1$ bar

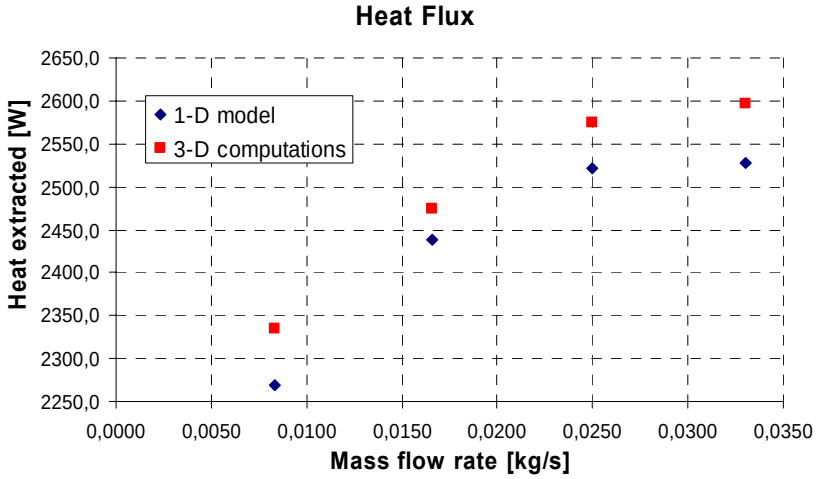

Figure 4.22: Evacuated heat as a function of mass flow rate, $T_g = 1400$ K, $M = 0.5$, $P_o = 1$ bar

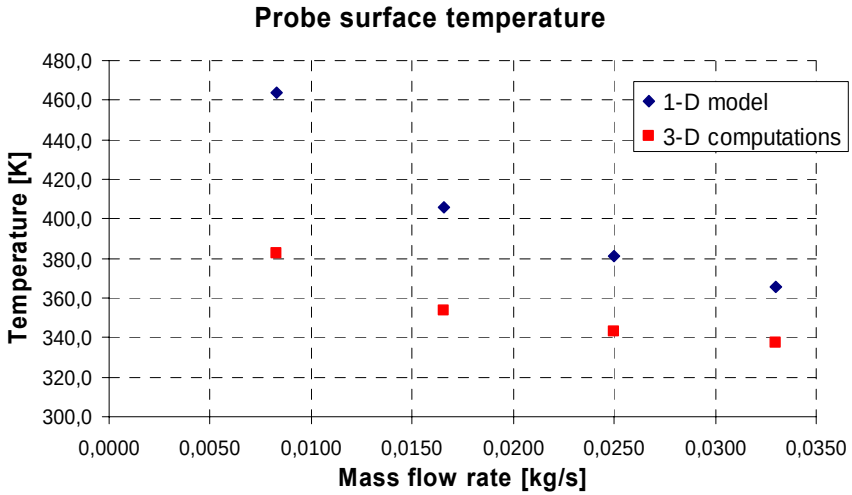

Figure 4.23: Probe surface temperature as a function of mass flow rate, $T_g = 1400$ K, $M = 0.5$, $P_o = 1$ bar

eled as a tube without considering the cooling effects at the sensor region.

In the three-dimensional geometry, heat can flow from the probe surface to the sensor which is like a cylinder in a water cross-flow incoming from the inner cylinder. In this way, around the sensor, the coolant can extract more heat and consequently the values computed for the three-dimensional geometry were found to be higher than those calculated in the one-dimensional model. Higher heat flux yields higher outlet water temperatures and lower external surface probe temperatures.

Additionally, it is important to recall that the probe stem is not modeled in the 3D model, and in fact, the indicated high surface temperature is found in the stem section in the one-dimensional model, where both the wall thickness and the section diameter is higher.

In summary, the comparison indicates that the one-dimensional model is able to predict the global cooling parameters, with a slight overestimation, which might be used as a safety factor.

4.3.5 Internal Cooling Optimization

As seen in Figure 4.24, the initial probe design suffers from the recirculation around the sensor area of the return channel. In addition, the highest temperature is observed at the probe tip area as shown in Figure 4.19 (left) due to poor coolant circulation in the space between the two hemispherical parts as shown.

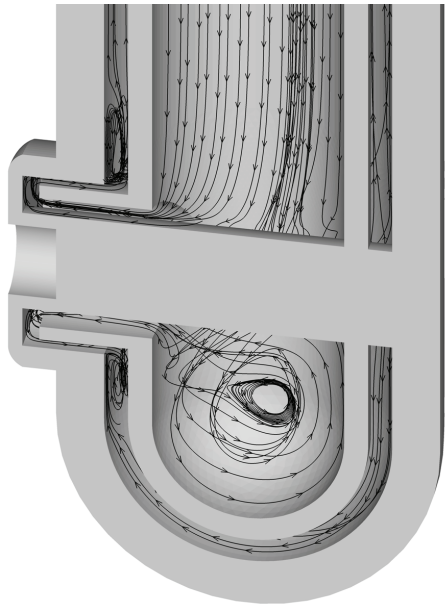

Figure 4.24: Stream traces in original probe design, $T_g = 1400$ K, $M = 0.5$, $P_o = 1$ bar

In an effort to eliminate the above-mentioned hot spot at the probe tip, different solutions are investigated. Drilling a hole through the hemispherical tip of the inner tube, creating an impinging flow at the probe tip and greatly increasing the circulation, is found to be the most effective solution reducing the tip temperature approximately by 40 K and creating a much more uniform temperature distribution for a total gas temperature of 1400 K, $M = 0.5$, $P_o = 1$ bar, $h_g = 2600$ W/m^{2}K and a coolant flow rate of 2ℓ/min, as shown in Figure 4.25.

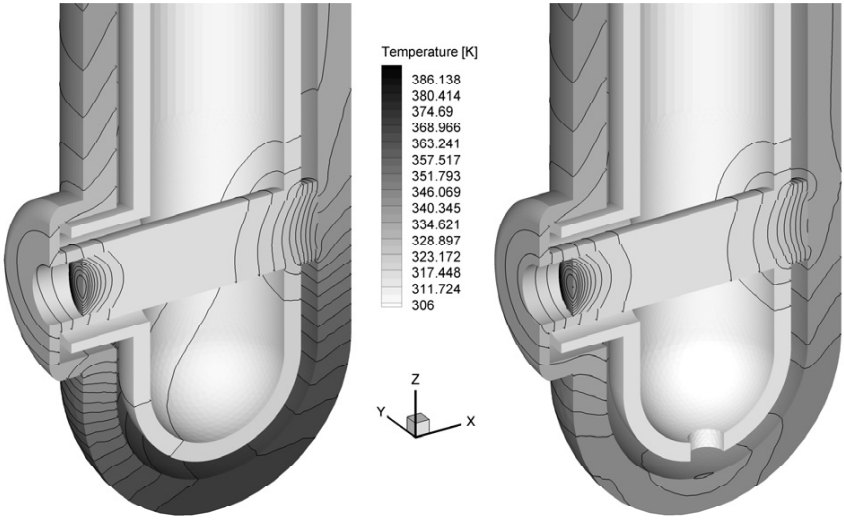

Figure 4.25: Temperature distribution in original and modified probe design, $T_g = 1400$ K, $M = 0.5$, $P_o = 1$ bar

Stream-traces for the modified probe head geometry, given in Figure 4.26, show that the impinging coolant in the probe tip is also instrumental in increasing the coolant flow rate at the tip region, creating a new coolant passage between the feed and return lines, also decreasing the unavoidable recirculation around the sensor, greatly improving the cooling performance without compromising the coolant flow around the sensor.

In order to conclude the three-dimensional simulation on the probe concept, two different probe materials are compared, which are copper and Inconel 600. The simulations were conducted for a probe immersion depth of 85 mm, without any TBC layer in an environment representative of a modern high pressure turbine, where $T_g = 1400$ K, $M = 0.5$, $P_o = 40$ bar. The results are presented in Figure 4.27.

The thermal gradient across the probe wall is much higher for Inconel 600 due to the low thermal conductivity (14.9 W/mK at 300 K, 27.5 W/mK at 1070 K) compared to copper (>400 W/mK). Temperature levels exceed 1000 K in the case of Inconel 600 where the values remain well

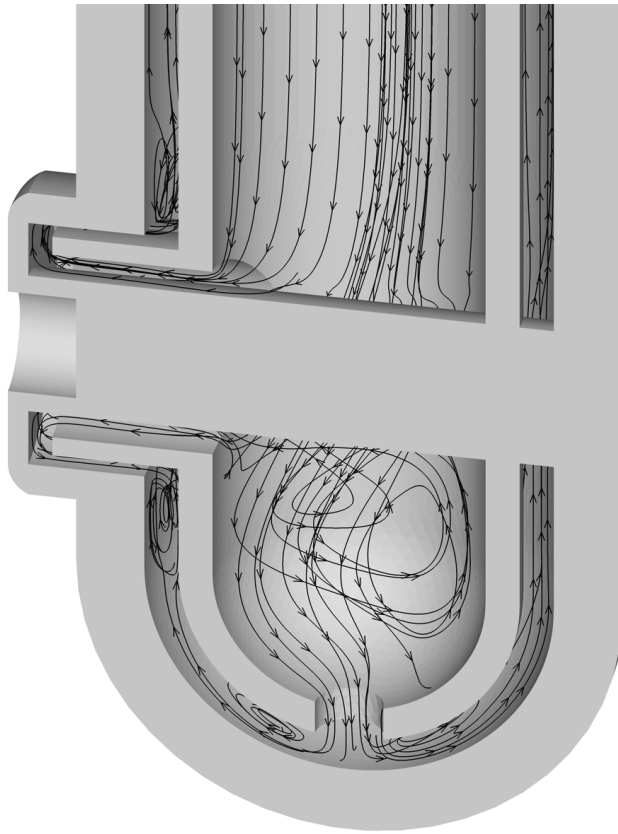

Figure 4.26: Stream traces in modified probe design, $T_g = 1400$ K, $M = 0.5$, $P_o = 1$ bar

below 800 K for copper, with a screen temperature around 700 K. As already stated earlier, the sensor diaphragm is capable to continuously withstand a maximum temperature of 780 K. On the coolant side, calculations show that the cooling water temperature locally reaches 460 K in small recirculation zones around the sharp corners near the sensor. In order to keep the coolant in the liquid phase, it was decided to pressurize the cooling system up to a pressure of 50 bar, where the water boiling temperature approaches 560 K. Pressurizing the probe internally also has the advantage to be able to equalize internal and external pres-

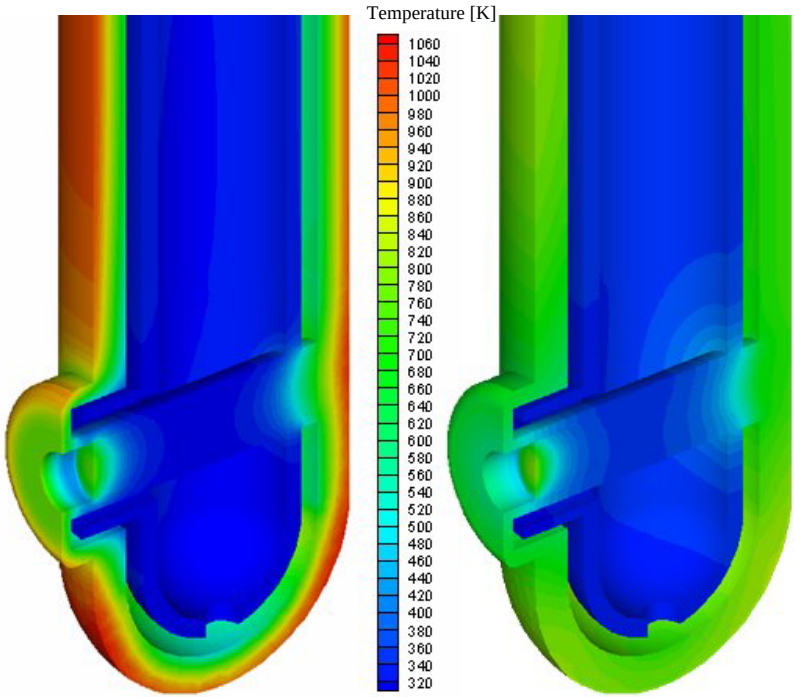

Figure 4.27: Temperature distribution in modified probe design, Inconel 600 (left), Copper (right), $T_g = 1400$ K, $M = 0.5$, $P_o = 40$ bar

sure levels depending on the environment, instrumental in minimizing the structural stresses.

4.4 Mechanical Design

The probe is first modeled as a pressure vessel using the AD-Merkblatt fact sheets [15], which are employed to certify the design of pressure vessels. The investigated cases include a pressurized probe (at 50 bar) in a vacuum environment, and a probe under vacuum in an environment pressurized to 50 bar.

4.4.1 Structural validation using AD-Merkblatt

The required shell thicknesses and the weld stresses are calculated using AD-Merkblatt [15] which is the common pressure vessel certification norm used. Calculations are carried out for 70bars of pressure difference for both pressurized probe in vacuum and probe under vacuum in a high pressure medium. The opening in the structure are taken into account as weakening factors. Finally, the brazing points are calculated.

To be on the safe side, a higher than expected pressure difference is selected while underestimating the material properties. However, no data regarding the brazing strength have been found so far. On the other hand, it is found that generally the welds have a strength at the order of one third of the base metal. In order to estimate this strength, data from a silver brazing process done formerly in-house is taken, assuming Inconel alloy will have a higher value.

Shell thicknesses for each component are far from being critical while the highest weld stress is found to be 26.40 daN/mm^2 found around the sensor holder piece. It has to be noted that the former silver brazing done has a strength of 35 daN/mm^2. On the other hand, laser welding is used for the welding of the pieces, which in theory only affects the strength of the material due to presence of heat-affected-zones.

Detailed calculations are given below in 4.4.1.2 and 4.4.1.3 for hot and room temperature strength values for Inconel 600. The formulas used from AD-Merkblatt [15] are given below in 4.4.1.

4.4.1.1 Structural validation formulas from AD-Merkblatt

B1: Cylindrical and spherical shells subjected to internal overpressure
For cylindrical or spherical shells subject to internal overpressure, the below given formulas are applicable provided that the ratio of outer to inner diameter is less than 1.2. For shells with outer diameter less than 200mm, the outer to inner diameter ratio limit extends to 1.7.

for cylindrical shells:

$$s = \frac{D_a p}{20\frac{K}{S}v + p} + c_1 + c_2 \tag{4.18}$$

for spherical shells:

$$s = \frac{D_a p}{40\frac{K}{S}v + p} + c_1 + c_2 \tag{4.19}$$

B6: Cylindrical shells subjected to external overpressure While the applicability criterion is the same as above in B1, the equation for maximum external pressure a shell can withstand is given as:

$$p = \frac{E}{S_k}\frac{20}{1-\nu^2}\left(\frac{s_e - c_1 - c_2}{D_a}\right)^3 \tag{4.20}$$

Required shell thickness for a certain external pressure can therefore be calculated.

B9: Openings in cylindrical, conical and spherical shells The below given formula is valid within the following range:

$0.002 \leq \frac{s_e - c_1 - c_2}{D_a} \leq 0.1$

$$s_A = \frac{D_a p}{v_A\left(20\frac{K}{S}v\right) + p} \tag{4.21}$$

The v_A values for nozzles perpendicular to the shell can be read with sufficient accuracy from figures 4.28 to 4.32 and 4.33 to 4.35. The wall thickness s_A in these figures is the required wall thickness determined by iteration. Intermediate values may be obtained by linear interpolation between the families of curves in the individual figures.

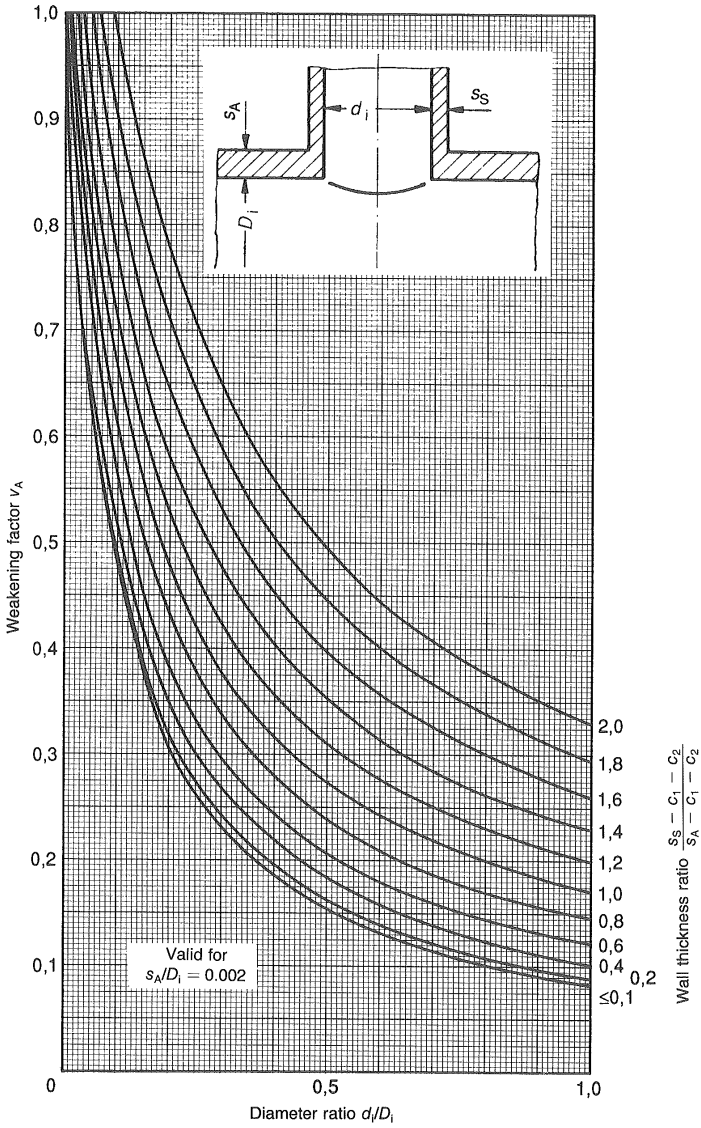

Figure 4.28: Weakening factor for openings and branches perpendicular to the shell in cylinders and cones

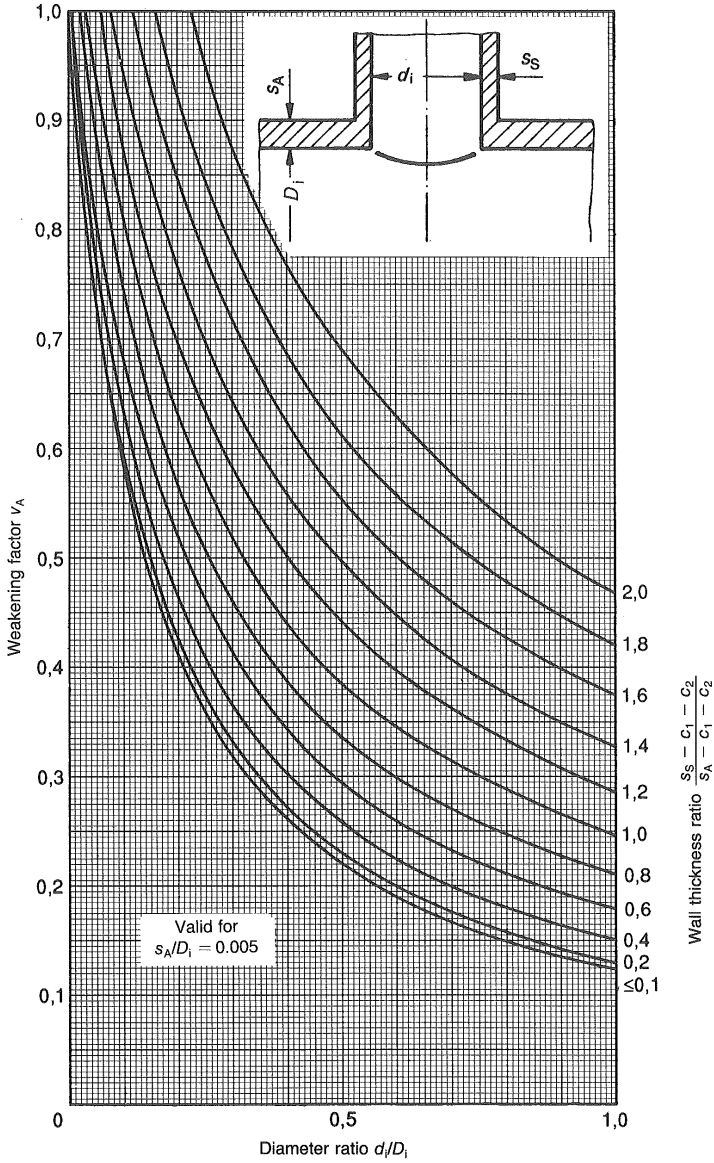

Figure 4.29: Weakening factor for openings and branches perpendicular to the shell in cylinders and cones

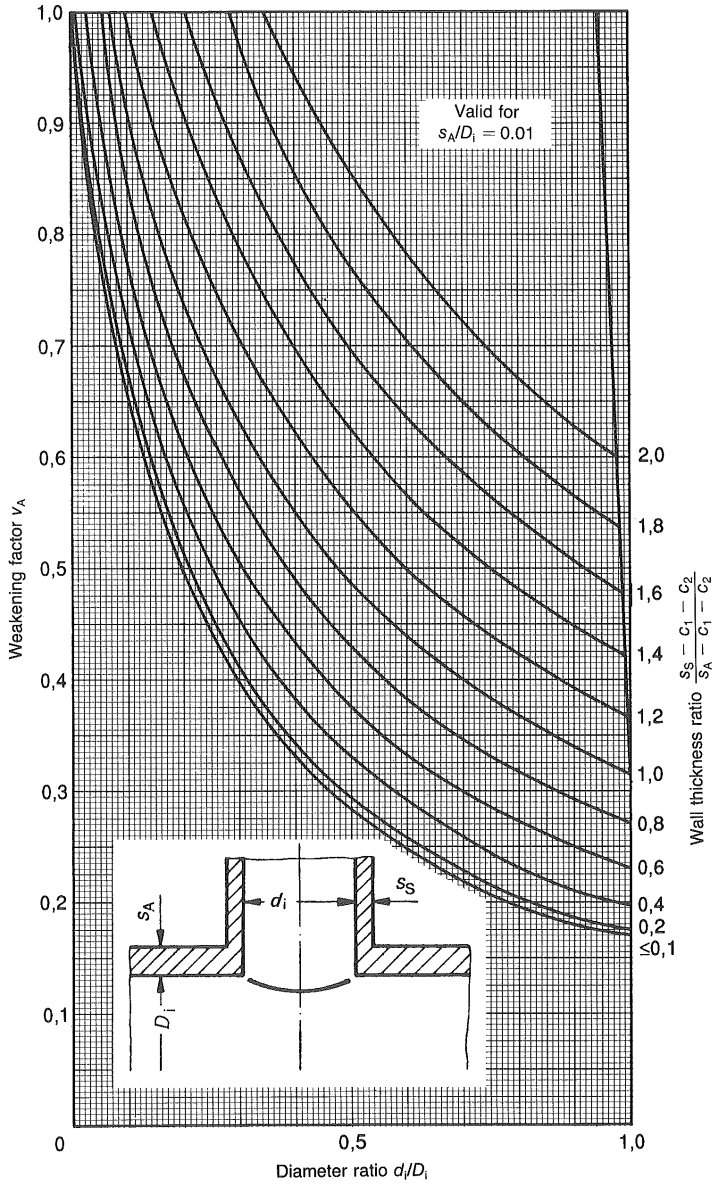

Figure 4.30: Weakening factor for openings and branches perpendicular to the shell in cylinders and cones

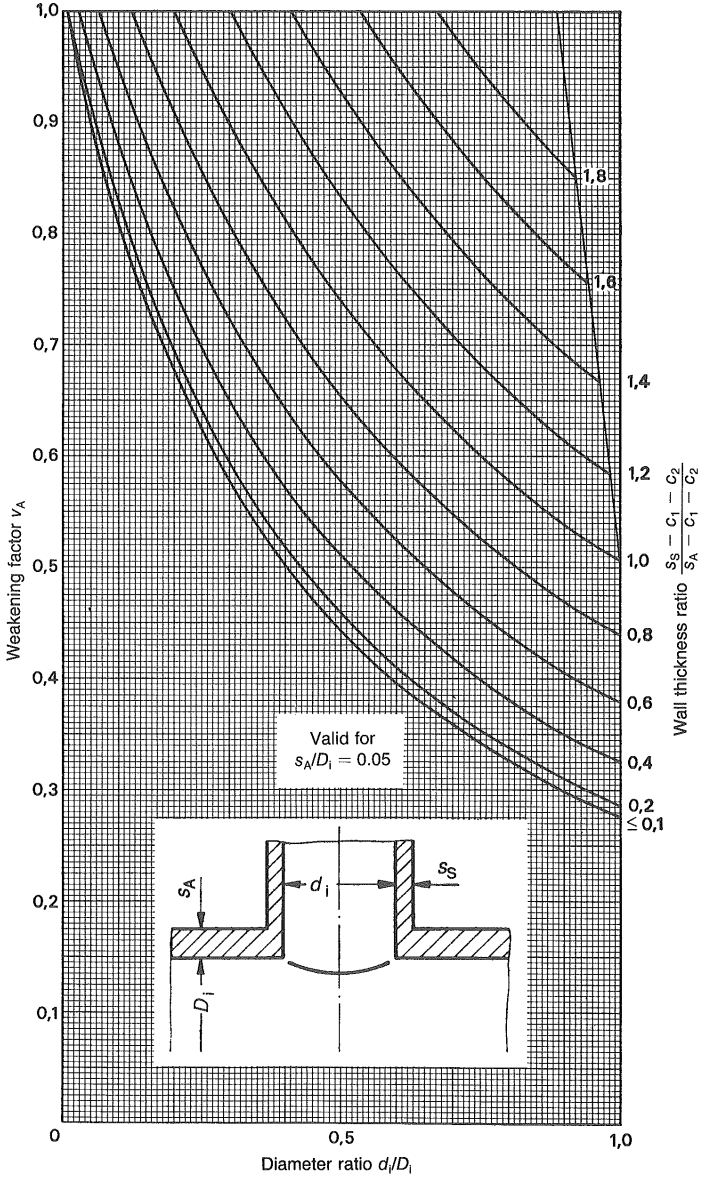

Figure 4.31: Weakening factor for openings and branches perpendicular to the shell in cylinders and cones

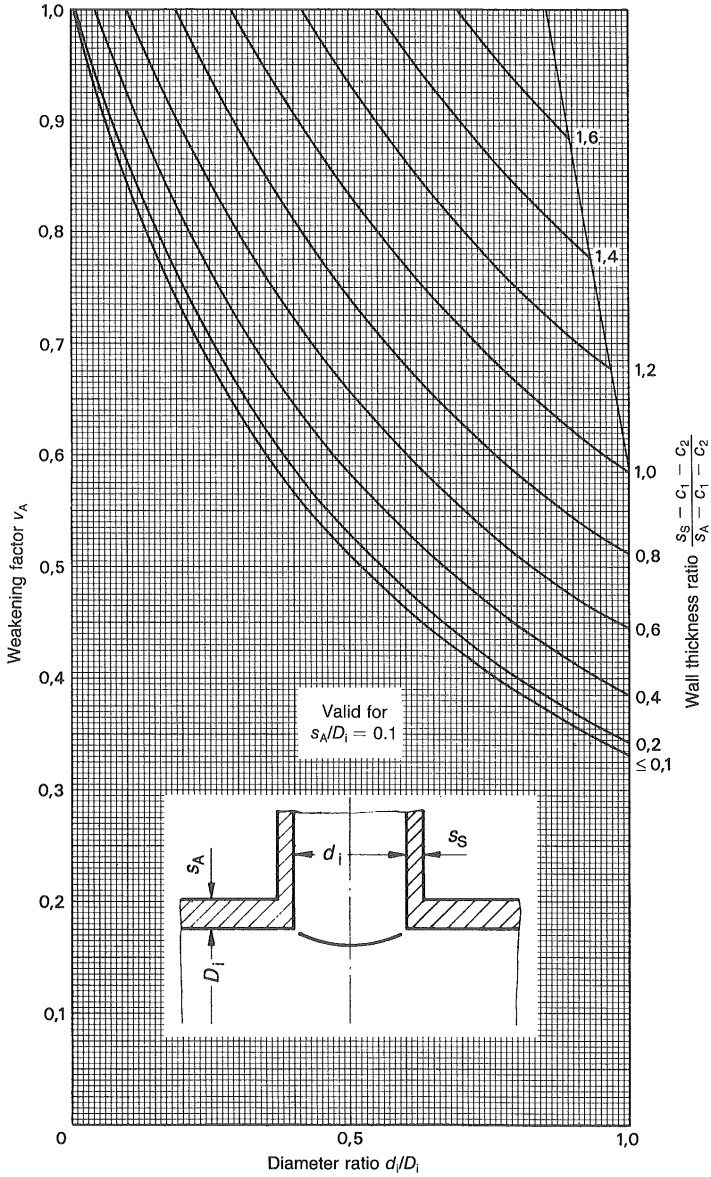

Figure 4.32: Weakening factor for openings and branches perpendicular to the shell in cylinders and cones

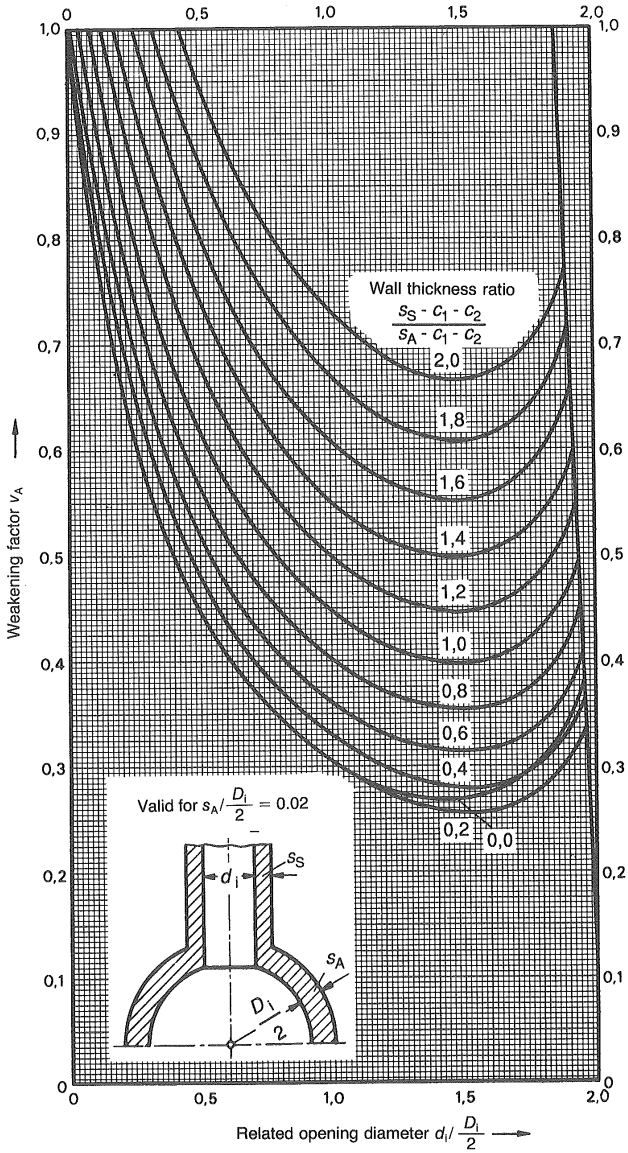

Figure 4.33: Weakening factor for openings and branches perpendicular to the shell in cones

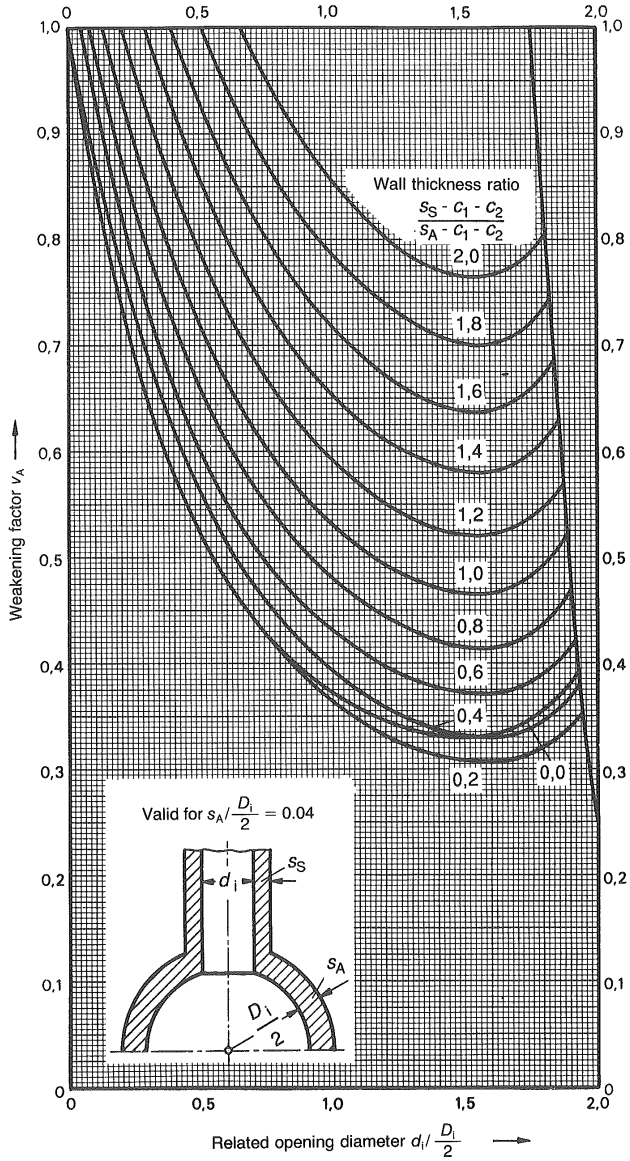

Figure 4.34: Weakening factor for openings and branches perpendicular to the shell in cones

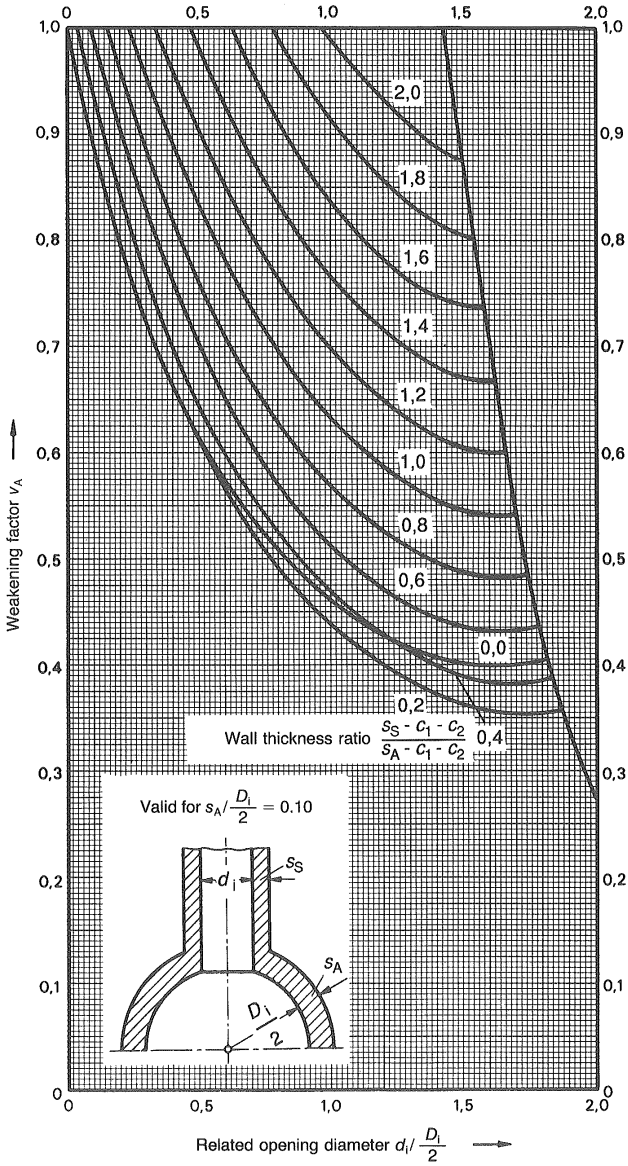

Figure 4.35: Weakening factor for openings and branches perpendicular to the shell in cones

4.4.1.2 Calculations at room temperature

Tube thickness calculation ∅10/8mm tube subject to internal pressure (According to AD-Merkblatt B1):

External diameter	10mm
Nominal pressure	50bar
Calculation pressure	70bar
Material strength	600N/mm^2
Safety factor	1.5
Tolerances	±0mm
Stress utilization	1.0
Calculations:	
Calculated thickness	0.09mm
Actual thickness	1.0mm

∅10/8mm tube subject to external pressure (According to AD-Merkblatt B6):

External diameter	10mm
Calculation thickness	1mm
Elastic Modulus	157000N/mm^2
Safety factor	3.0
Tolerances	±0mm
Poisson's ratio	0.3
Calculations:	
Calculated max. pressure	1150.18bar
Required thickness	0.39mm
Actual thickness	1.0mm

∅8/6mm tube subject to internal pressure (According to AD-Merkblatt B1):

External diameter	8mm
Nominal pressure	50bar
Calculation pressure	70bar
Material strength	600N/mm^2
Safety factor	1.5
Tolerances	±0mm
Stress utilization	1.0
Calculations:	
Calculated thickness	0.07mm
Actual thickness	1.0mm

∅8/6mm tube subject to external pressure (According to AD-Merkblatt B1):

External diameter	8mm
Calculation thickness	1mm
Elastic Modulus	157000N/mm^2
Safety factor	3.0
Tolerances	±0mm
Poisson's ratio	0.3
Calculations:	
Calculated max. pressure	2246.45bar
Required thickness	0.31mm
Actual thickness	1.0mm

∅5/4mm tube subject to internal pressure (According to AD-Merkblatt B1):

External diameter	5mm
Nominal pressure	50bar
Calculation pressure	70bar
Material strength	600N/mm^2
Safety factor	1.5
Tolerances	±0mm
Stress utilization	1.0
Calculations:	
Calculated thickness	0.04mm
Actual thickness	0.5mm

∅5/4mm tube subject to external pressure (According to AD-Merkblatt B1):

External diameter	5mm
Calculation thickness	0.5mm
Elastic Modulus	157000N/mm^2
Safety factor	3.0
Tolerances	±0mm
Poisson's ratio	0.3
Calculations:	
Calculated max. pressure	1150.18bar
Required thickness	0.2mm
Actual thickness	0.5mm

∅3.625/3.0254mm tube subject to internal pressure (According to AD-Merkblatt B1):

External diameter	6.625mm
Nominal pressure	50bar
Calculation pressure	70bar
Material strength	600N/mm^2
Safety factor	1.5
Tolerances	±0mm
Stress utilization	1.0
Calculations:	
Calculated thickness	0.06mm
Actual thickness	0.3mm

∅3.625/3.0254mm tube subject to external pressure (According to AD-Merkblatt B1):

External diameter	3.625mm
Calculation thickness	0.3mm
Elastic Modulus	157000N/mm^2
Safety factor	3.0
Tolerances	±0mm
Poisson's ratio	0.3
Calculations:	
Calculated max. pressure	651.94bar
Required thickness	0.14mm
Actual thickness	0.3mm

∅2.25/1.65mm tube subject to internal pressure (According to AD-Merkblatt B1)

External diameter	2.25mm
Nominal pressure	50bar
Calculation pressure	70bar
Material strength	600N/mm^2
Safety factor	1.5
Tolerances	±0mm
Stress utilization	1.0
Calculations:	
Calculated thickness	0.02mm
Actual thickness	0.3mm

∅2.25/1.65mm tube subject to external pressure (According to AD-Merkblatt B6):

External diameter	2.25mm
Calculation thickness	0.3mm
Elastic Modulus	157000N/mm^2
Safety factor	3.0
Tolerances	±0mm
Poisson's ratio	0.3
Calculations:	
Calculated max. pressure	2726.36bar
Required thickness	0.09mm
Actual thickness	0.3mm

Domed end of ∅10/8mm tube subject to pressure (According to AD-Merkblatt B1):

Radius of curvature	3mm
External diameter	8mm
Nominal pressure	50bar
Calculation pressure	70bar
Material strength	600N/mm^2
Safety factor	1.5
Tolerances	±0mm
Stress utilization	1.0
Calculations:	
Calculated thickness	0.03mm
Actual thickness	1.0mm

Calculation of the openings on the cylindrical body According to AD-Merkblatt B9:

Internal diameter of the tube	6mm
Diameter of the opening	4mm
Thickness of the tube	0.5mm
Weakening factor	0.54
Wall thickness/opening ∅	0.250
Wall thickness ratio	0.5
opening ∅/tube ∅	0.667
Calculations:	
Required thickness	0.129mm
Actual thickness	0.5mm

Calculation of brazed joint stresses Probe mount adapter and outer tube stem junction:

Tube diameter	10mm
Brazed length	12mm
Brazed surface	376.99mm^2
Nominal pressure	50bar
Calculation pressure	70bar
Calculations:	
Force on weld	549.8N
Stress on weld	14.58daN/mm^2

Outer tube and stem junction:

Tube diameter	8mm
Brazed length	8mm
Brazed surface	201.06mm^2
Nominal pressure	50bar
Calculation pressure	70bar
Calculations:	
Force on weld	351.9N
Stress on weld	17.5daN/mm^2

Sensor holder piece and outer tube junction:

Brazed surface	22.78mm^2
Nominal pressure	50bar
Calculation pressure	70bar
Calculations:	
Force on weld	60.1N
Stress on weld	26.4daN/mm^2

4.4.1.3 Calculations at maximum surface temperature

Tube thickness calculation ∅10/8mm tube subject to internal pressure (According to AD-Merkblatt B1):

External diameter	10mm
Nominal pressure	50bar
Calculation pressure	70bar
Material strength	300N/mm^2
Safety factor	1.5
Tolerances	±0mm
Stress utilization	1.0
Calculations:	
Calculated thickness	0.17mm
Actual thickness	1.0mm

∅10/8mm tube subject to external pressure (According to AD-Merkblatt B6):

External diameter	10mm
Calculation thickness	1mm
Elastic Modulus	157000N/mm^2
Safety factor	3.0
Tolerances	±0mm
Poisson's ratio	0.3
Calculations:	
Calculated max. pressure	1150.18bar
Required thickness	0.39mm
Actual thickness	1.0mm

∅8/6mm tube subject to internal pressure (According to AD-Merkblatt B1):

External diameter	8mm
Nominal pressure	50bar
Calculation pressure	70bar
Material strength	300N/mm^2
Safety factor	1.5
Tolerances	±0mm
Stress utilization	1.0
Calculations:	
Calculated thickness	0.14mm
Actual thickness	1.0mm

∅8/6mm tube subject to external pressure (According to AD-Merkblatt B1):

External diameter	8mm
Calculation thickness	1mm
Elastic Modulus	157000N/mm^2
Safety factor	3.0
Tolerances	±0mm
Poisson's ratio	0.3
Calculations:	
Calculated max. pressure	2246.45bar
Required thickness	0.31mm
Actual thickness	1.0mm

∅5/4mm tube subject to internal pressure (According to AD-Merkblatt B1):

External diameter	5mm
Nominal pressure	50bar
Calculation pressure	70bar
Material strength	300N/mm^2
Safety factor	1.5
Tolerances	±0mm
Stress utilization	1.0
Calculations:	
Calculated thickness	0.09mm
Actual thickness	0.5mm

∅5/4mm tube subject to external pressure (According to AD-Merkblatt B6):

External diameter	5mm
Calculation thickness	0.5mm
Elastic Modulus	157000N/mm^2
Safety factor	3.0
Tolerances	±0mm
Poisson's ratio	0.3
Calculations:	
Calculated max. pressure	1150.18bar
Required thickness	0.2mm
Actual thickness	0.5mm

∅3.625/3.0254mm tube subject to internal pressure (According to AD-Merkblatt B1):

External diameter	6.625mm
Nominal pressure	50bar
Calculation pressure	70bar
Material strength	300N/mm^2
Safety factor	1.5
Tolerances	±0mm
Stress utilization	1.0
Calculations:	
Calculated thickness	0.11mm
Actual thickness	0.3mm

∅3.625/3.0254mm tube subject to external pressure (According to AD-Merkblatt B1):

External diameter	3.625mm
Calculation thickness	0.3mm
Elastic Modulus	157000N/mm^2
Safety factor	3.0
Tolerances	±0mm
Poisson's ratio	0.3
Calculations:	
Calculated max. pressure	651.94bar
Required thickness	0.14mm
Actual thickness	0.3mm

∅2.25/1.65mm tube subject to internal pressure (According to AD-Merkblatt B1):

External diameter	2.25mm
Nominal pressure	50bar
Calculation pressure	70bar
Material strength	300N/mm^2
Safety factor	1.5
Tolerances	±0mm
Stress utilization	1.0
Calculations:	
Calculated thickness	0.04mm
Actual thickness	0.3mm

∅2.25/1.65mm tube subject to external pressure (According to AD-Merkblatt B1):

External diameter	2.25mm
Calculation thickness	0.3mm
Elastic Modulus	157000N/mm^2
Safety factor	3.0
Tolerances	±0mm
Poisson's ratio	0.3
Calculations:	
Calculated max. pressure	2726.36bar
Required thickness	0.09mm
Actual thickness	0.3mm

Domed end of ∅10/8mm tube subject to pressure (According to AD-Merkblatt B1):

Radius of curvature	3mm
External diameter	8mm
Nominal pressure	50bar
Calculation pressure	70bar
Material strength	300N/mm^2
Safety factor	1.5
Tolerances	±0mm
Stress utilization	1.0
Calculations:	
Calculated thickness	0.07mm
Actual thickness	1.0mm

Calculation of the openings on the cylindrical body According to AD-Merkblatt B9:

Internal diameter of the tube	6mm
Diameter of the opening	4mm
Thickness of the tube	0.5mm
Weakening factor	0.54
Wall thickness/opening ∅	0.250
Wall thickness ratio	0.5
opening ∅/tube ∅	0.667
Calculations:	
Required thickness	0.255mm
Actual thickness	0.5mm

Calculation of brazed joint stresses Probe mount adapter and outer tube stem junction:

Tube diameter	10mm
Brazed length	12mm
Brazed surface	376.99mm^2
Nominal pressure	50bar
Calculation pressure	70bar
Calculations:	
Force on weld	549.8N
Stress on weld	14.58daN/mm^2

Outer tube and stem junction:

Tube diameter	8mm
Brazed length	8mm
Brazed surface	201.06mm^2
Nominal pressure	50bar
Calculation pressure	70bar
Calculations:	
Force on weld	351.9N
Stress on weld	17.5daN/mm^2

Sensor holder piece and outer tube junction:

Brazed surface	22.78mm^2
Nominal pressure	50bar
Calculation pressure	70bar
Calculations:	
Force on weld	60.1N
Stress on weld	26.4daN/mm^2

4.4.2 Thermal stresses and FEM modeling

The effect of thermal stresses around the probe geometry are estimated using local Nusselt-Reynolds number distributions, shown in Figure 4.36, measured by Schmidt and Wenner [65].

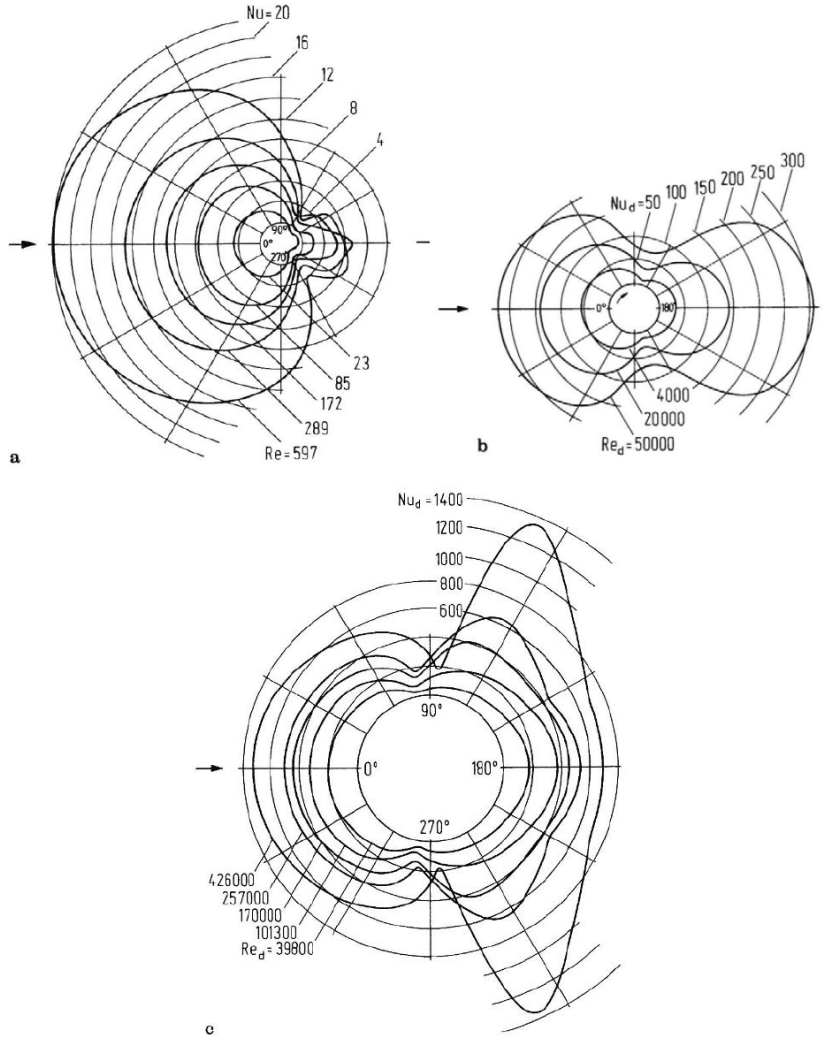

Figure 4.36: Nusselt number distributions around a circular cylinder for various Reynolds numbers, Schmidt and Wenner [65]

The minimum and maximum values of the Nusselt number for a given Reynolds number are determined and used to calculate maximum and

minimum temperatures, which are in turn applied as a discontinuity, neglecting the smoother distribution.

The thermal expansion calculated using this temperature difference is used as a strain value to solve for the corresponding thermal stress, which is found to be of the order of 40% of the yield strength of the material. It is also important to note that at the location where the thermal stress is of importance, the von Mises stress calculated using a finite-element-method solver (SolidWorks) is found to be one order of magnitude less than the yield stress.

The maximum thermal stress is found to be at the probe tip near the sensor, while the maximum bending stresses are at the probe supports due to the cantilever arrangement of the probe in a traverse gear.

The structural design of the probe is assessed using a three-dimensional finite-element solver for real engine environment with respect to different immersion lengths. With the current traverse gear, which supports the probe at $\sim$145 mm away from the engine outer casing due to a cooling tower assembly between the casing and the traverse as illustrated later in Figure 6.9, maximum immersion depth before yield is found to be around 70 millimeters.

However, this value is greatly enhanced using a different traverse gear which supports the probe nearer to the casing. Therefore, it is highly recommended to use a bush at the probe access hole location, which may also be combined with a seal to act as a structural simple support. While designing such bushings, it is of crucial importance to use materials such as Invar to avoid expansion in addition to the use of solid lubricants such as graphite molybdenum disulfide (MoS_2) in order to prevent jamming of probes.

Chapter 5

Prototype Manufacturing and System Integration

5.1 Material Selection

The probe material is selected using the heat transfer predictions described previously and other properties such as corrosion resistance, welding properties, structural and fatigue strength, resistance to creep and thermal stresses, et cetera. Other important factors affecting the material selection are the availability of technical data particularly at high temperatures, prior experience with the specific alloy under consideration and market availability in different forms such as tubes, rods, sheets or plates and finally material cost.

In the light of the simulations performed and in order to manufacture a probe with adequate service life corresponding to a test campaign, priority is given to superalloys as they exhibit excellent mechanical strength and creep resistance at high temperatures. Corrosion resistance and fatigue cycle life are other factors favoring the choice of superalloys, which are typically developed and extensively used in gas turbine industry for high temperature applications. In the present case, simple solution alloys such as Inconel 718, Inconel 600 and Nimonic 75 have been investigated in detail, several properties of which have been given in Table 4.1, and Inconel alloys were favored considering other criteria such as commercial availability in required forms and cost.

Inconel alloys may be compared to the Udimet alloys, for which the primary application is blading for aero-engines and power generation gas turbines, with a slight difference of having lower amounts of Niobium,

but it shall be noted that Inconel alloys were freely licensed which yields an extensive amount of data in the open literature, where Udimet alloys were kept proprietary. Niobium is added in Inconel alloys in order to have better strength at elevated temperature levels, and it is superior to other strengtheners since it provides a slower aging response. One other advantage of Niobium is the ability of thermal stress-relieving before a piece is cracked.

Inconel alloys are difficult metal alloys to shape and machine using traditional techniques due to rapid work hardening. After the first machining pass, work hardening tends to elastically deform either the workpiece or the tool on subsequent passes. For this reason, age-hardened Inconel alloys such as IN718 are machined using an aggressive but slow cutting process using a hard cutting tool, minimizing the number of passes required. Alternatively, the majority of the machining can be performed with the workpiece in a solutionized form, with only the final steps being performed after age-hardening. External threads are machined using a lathe to 'single point' the threads, or by rolling the threads using a screw machine. Holes with internal threads are typically made by welding or brazing threaded inserts made of stainless steel.

Most of the Inconel alloys are hard to weld due to cracking and microstructural segregation of alloying elements in the heat affected zone. However, several alloys have been designed to overcome these problems, one of which being Inconel 600 (i.e. IN600).

Inconel 600 is defined by its manufacturer Special Metals, which is also the patent owner of Nimonic and Udimet alloys, as a nickel-chromium alloy with good oxidation resistance at high temperatures and resistance to chloride-ion stress-corrosion cracking, corrosion by high-purity water, and caustic corrosion. IN600 is used for furnace components, in chemical and food processing, in nuclear engineering, and for sparking electrodes. The alloy is the standard material for nitriding containers because of its resistance to nitrogen at high temperatures.

Its resistance against oxidation at high temperatures, caustic corrosion and corrosion by high-purity water is essential for this application. High-purity distilled water is chosen as coolant for preventing any stains

left within the cooling channels. Caustic corrosion resistance is favored since it allows use of caustic substances which are used as cleaning agents like Sodium hydroxide used extensively to clear clogged drains.

The material has the ability to retain a protective oxide coating under conditions of cyclic exposure to the temperature. IN600 has good resistance to carburization. It also resists attack by sulfur compounds at moderate temperatures, but it is subject to sulfidation in high temperature, sulfur containing environments. Molybdenum disulfide, a lubricant sometimes used to aid parts assembly, should not be used if the material will be subsequently exposed to temperatures above 700 K.

5.2 Prototype Manufacturing and Assembly

Manufacturing a probe incorporating a delicate sensor inside pressurized water cooling requires the use of micro-machining and complex joining techniques. Creating the manufacturing blueprints requires extensive planning of the assembly. Given the probe needs to be hermetically sealed, several bushings and spacers with three-dimensional geometry are designed together with several assembly pins, allowing to carry the essential sensor mount-angle reference to the probe stem as shown in Figure 5.1.

Components shown in Figure 5.1, may be listed from top to bottom as alignment crown, signal cable housing, cable housing to sensor housing spacer ring, inner probe tube with an alignment pin and the inner tube to sensor housing spacer, outer probe tube, flow diverter, sensor package and finally the sensor housing.

Except for the sensor housing also incorporating the sensor screen, all the pieces are manufactured using conventional turning operations using CNC milling machines and lathes. The sensor housing is manufactured using a combination of turning and RAM EDM (Electric Discharge Machining) operations as the geometry is not suitable for cutting the water feed and return groove shown in Figure 3.2.

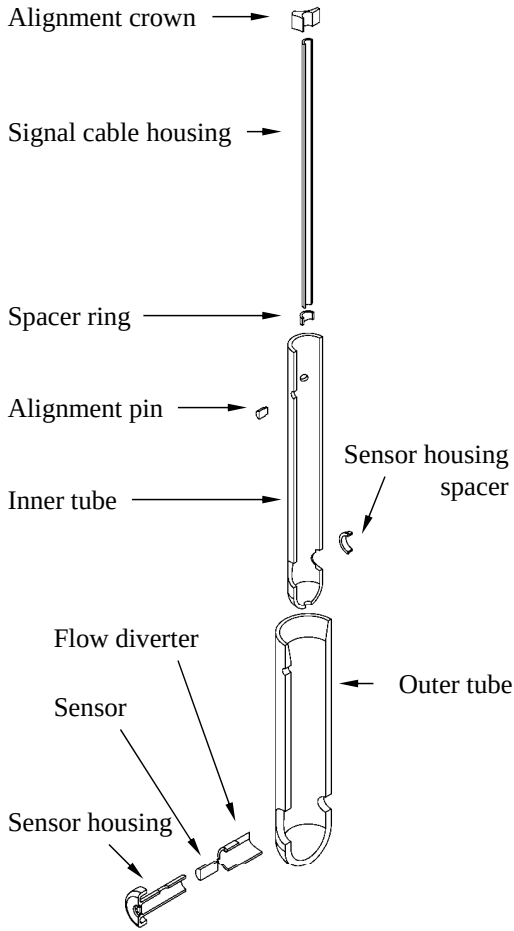

Figure 5.1: Exploded view of the probe tip

For joining the machined pieces, laser welding is used. Although initially brazing has been chosen, this method has not been preferred as the application of a brazing paste is required, which may lead to blockage of the cooling channels due to capillarity issues, in addition to being highly corrosive.

In order to verify and optimize the welding process, a dummy probe without sensor and simplified outer geometry (i.e. without a rounded tip), shown in Figure 5.2 has been built. Mechanical strength and sealing of the weld has been successfully checked on this dummy probe assembly via a hydraulic test with internal pressure up to 110 bar.

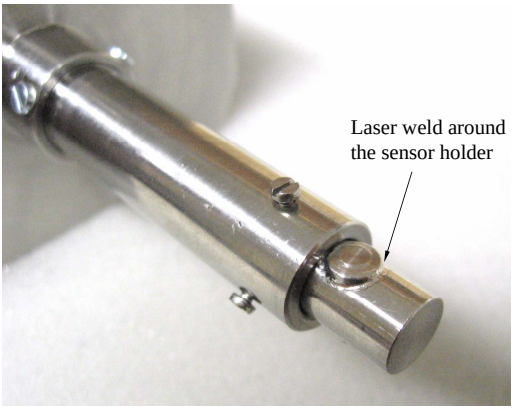

Figure 5.2: Dummy probe tip

A view of the laser weld around the sensor housing using a microscope is shown in Figure 5.3.

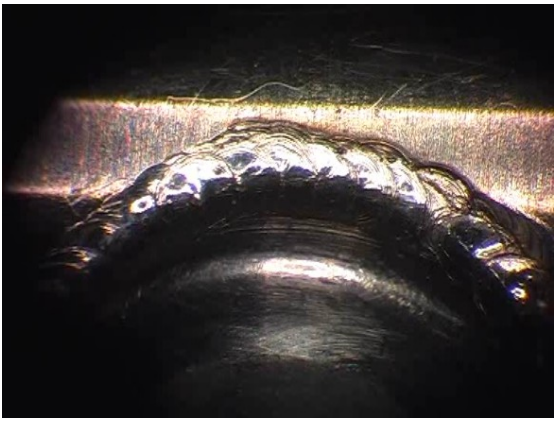

Figure 5.3: Laser welding around the sensor holder

Following the hydraulic verification on the dummy probe, the first prototype was assembled. The assembling process required is rather complicated, composed of sensor mount welding, sensor installation, soldering of the signal wire-harness for the preparation of probe head.

Once the head is assembled as shown in Figure 5.4, the hermetic seal of the wire-harness is ensured using elastic sealants before the inner stem tubes are welded.

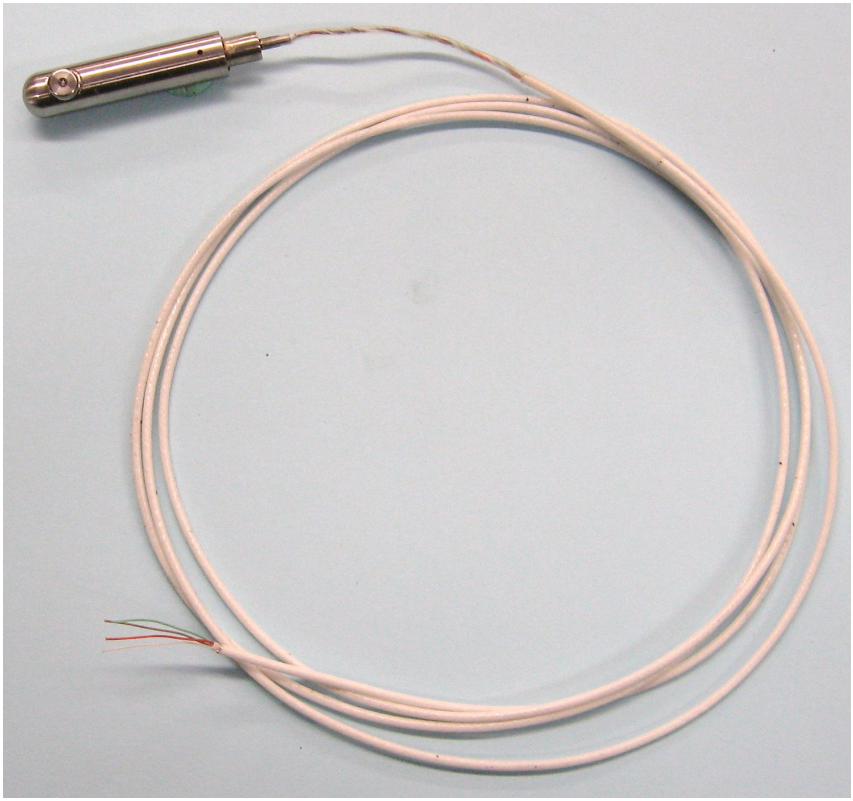

Figure 5.4: Welded probe tip with the sensor installed and sealed

The inner tube is welded before the outer tube, at which phase a pin, shown in Figure 5.5, is inserted in order to align the sensor axis to the probe stem reference.

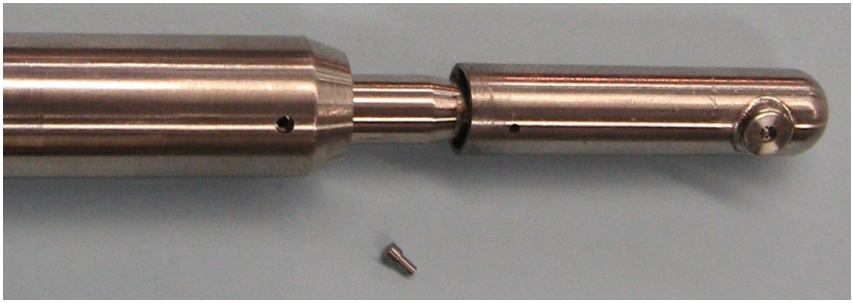

Figure 5.5: Head assembly of the probe

The final assembly is accomplished by installing the connection box, containing the coolant feed and return fittings, electronic connector for signal transmission and two PT100 temperature sensors, at the stem of the probe as shown in Figure 5.6a. The wires connected to the sensor are soldered to a pressure sealing socket placed at the stem of the probe. In order to seal the wires hermetically, the soldered regions are covered with epoxy resin. In Figure 5.6, the finished probe is shown.

Although a TBC layer has been foreseen initially, no coating has been applied on the prototype probe for two main reasons. First, the ceramic TBC coating requires firing in a furnace at temperatures above the metal recrystallization temperature, rendering the temper designation of the nickel superalloy employed obsolete and hence requiring a re-tempering process. Secondly, the thermal expansion of ceramic TBC coating does not match that of the superalloy used, causing surface cracks and hence grains that fall off the surface of the probe over time. Morevoer, it is impossible to re-apply a TBC coating on a finished probe due to the impossibility of scraping off the damaged layer, and due to the temperature limitation imposed by the sensor and wiring harness inside, not allowing the curing process required for hardening of the ceramic coating.

The threaded connector at the very top of Figure 5.6a is the socket for the sensor wires, where the two hoses on at the right are the coolant feed and return lines. At the left hand side are the PT100 RTD temperature sensors to monitor the coolant feed and return temperatures.

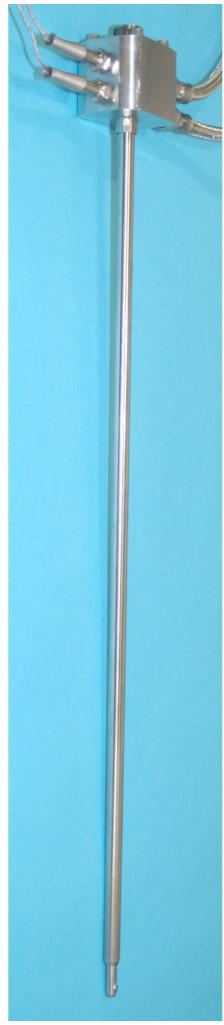

(a) Finished probe connected to the cooling system for hydraulic tests.

(b) Tip region of the probe after sealing and final welding.

Figure 5.6: First prototype of the VKI fast response cooled total pressure probe

Once the assembly is completed, the finished probe is tested using the cooling system in order to check for any possible leakages, and to verify the pressurization level required in order to achieve target mass flow rate.

5.3 Cooling System

The objectives of the design of the cooling system itself are twofold: first, the system was designed to provide the necessary coolant mass flow rate to the probe at high pressure. The objective of a highly pressurized water supply is in turn to increase the boiling temperature of the cooling water. The water boiling temperature at 50 bar is near 560 K ($\sim$287 °C). On the other hand, pressurizing the probe internally is also advantageous for equalizing internal and external probe pressures in an effort to minimize mechanical stresses at high temperatures.

Second, the system was conceived to reach the highest possible reliability and safety level in order to avoid any damage to an engine in case of failure of the system. The system is therefore designed with all necessary controls over pump speeds, filters, regulation valves, bypass valves or switches in case of filter clogging, etc and also equipped with appropriate alarms using a PLC computer used together with a dedicated data acquisition system.

A semi-closed loop system was favored in the present case, which is essentially a closed loop but with a non-pressurized reservoir. The main components of the system are a low pressure feed pump and a high pressure feed pump (up to 150 bar), a 32 kW plate heat exchanger and a double set of filters placed on the low pressure line. The complete system is made of stainless steel to avoid corrosion problems and distilled water is used to avoid any film formation such as lime stain inside the probe. The system also includes a high precision Coriolis mass flow meter and both coolant pressure and temperature values are monitored on the feed and return lines using Validyne variable reluctance pressure transducers and PT100 temperature sensors. Finally, the system is equipped with a data acquisition board and a remote control unit for operation from a test cell control room as far as 25 m from the system.

Figure 5.7 shows a photograph of the system, while the cooling system diagram is shown in Figure 5.8.

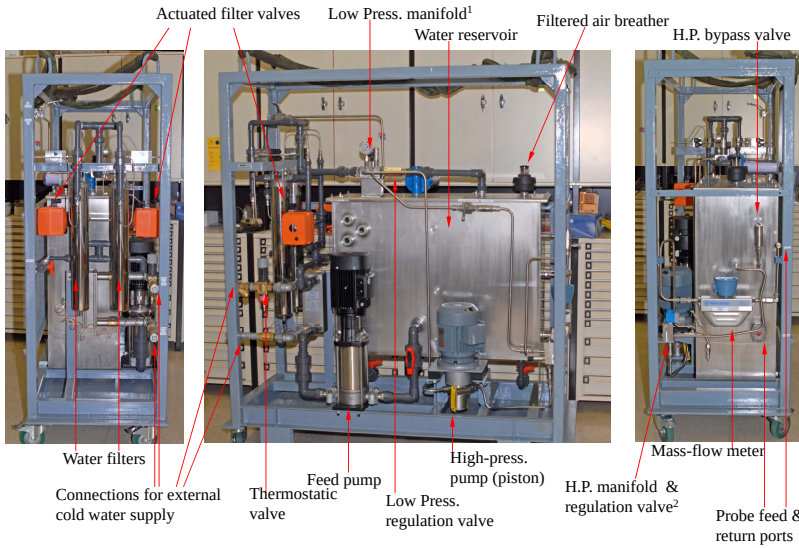

1. Low pressure manifold containing PT100 water temperature sensor, LP feed press. sensor and a manometer
2. High Pressure manifold containing PT100 water temperature sensor, HP pressure sensor, manometer and high pressure regulation valve (25-40 bar)

Figure 5.7: Left, front and right views of the cooling system

The knowledge of the mass flow rate and feed-return temperature difference is essential for the determination of the probe cooling rate. All system parameters are recorded via a LabView program for this purpose. The system is governed by a PLC (Programmable Logic Controller) system ensuring probe cooling under most adverse conditions, triggering relevant alarms such as filter clogging, inlet pressure variances, overheating, etc. essential for avoiding probe failure due to poor cooling and automatically running the system by switching filters and adjusting pump speeds in a fail-safe mode until the probe is retracted and the test rig is shut-down.

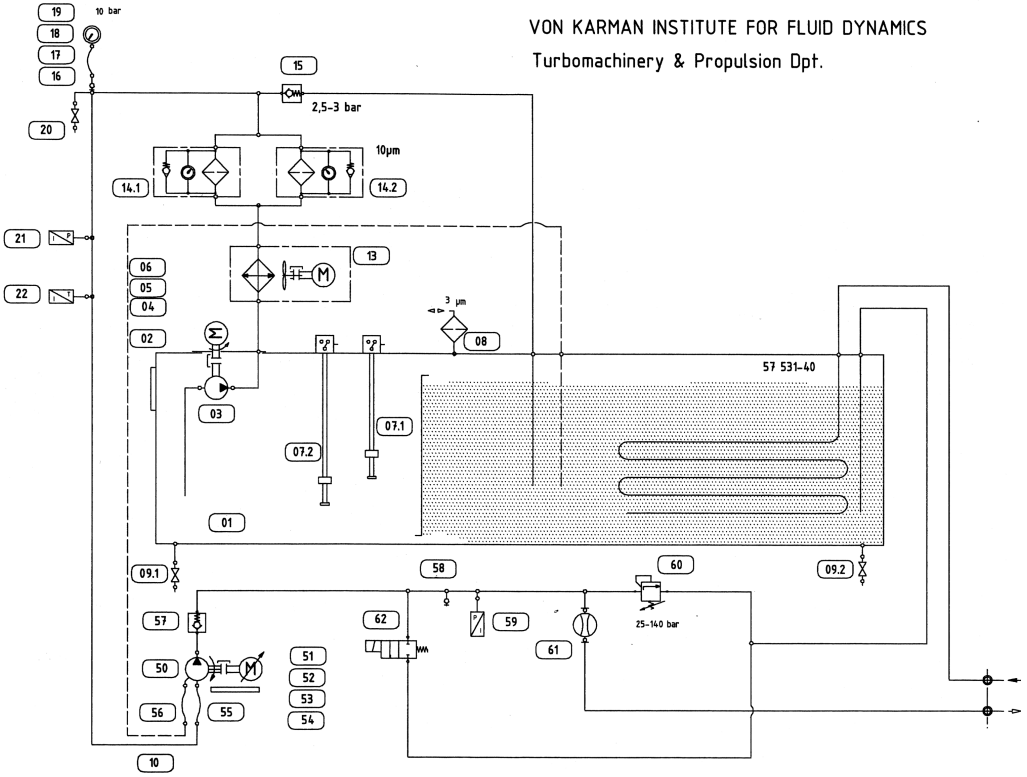

Figure 5.8: Cooling system diagram

Chapter 6

Prototype Testing

6.1 Calibration and Uncertainty

In order to present the measurement results obtained with the prototype probe, it is essential to give a thorough explanation on the calibration process, comprising static, dynamic and aerodynamic calibrations. While the static calibration determines the pressure to voltage conversion characteristics of the probe, the transfer function of the probe, indicating the natural frequencies and the signal amplification with respect to frequency, is obtained via dynamic calibration. Finally an aerodynamic calibration is performed in order to determine the total pressure recovery at various yaw angles.

It is worth mentioning that the uncertainty analyses presented in this work have been performed according to the ASME standard [3] and not the ISO standard [30]. As explained by Dieck [16], the two standards essentially yield the same values, while the difference is in grouping various uncertainty terms. In ASME type uncertainty analysis, various contributions to the overall uncertainty are categorized under systematic and random terms, greatly simplifying backwards traceability of uncertainty terms. First calibration of the first prototype probe is presented below in detail in order to give a thorough explanation of the calibration process and related uncertainty analyses.

6.1.1 Static Calibration

As explained in section 4.1, Kulite XCE-062 series has been employed in the probe design combined with an active compensation amplifier module requiring a full calibration map and as such, the probe has been calibrated for both temperature and pressure in a temperature controlled oil bath. Although the temperature calibration itself and its related uncertainty is irrelevant in measuring pressure which comprises the goal of this work, it is explained together with pressure uncertainty for the sake of presenting certain interesting aspects of the analyses carried out.

In order to accomplish this task, a K-type thermocouple has been calibrated initially to be used as temperature reference during the probe static calibration. It is therefore important to first present the uncertainty related to the thermocouple used as reference before presenting the uncertainty analyses of the pressure probe itself.

In order to calibrate the reference thermocouple, it is placed in a laboratory type oil bath inside a separate Erlenmeyer flask filled with methyl alcohol. An external laboratory mixer is employed to ensure temperature uniformity inside the alcohol filled flask. A mercury thermometer with a delimitation of 0.1°C is used as temperature reference for the calibration. 11 points have been acquired between 0 and 60°C with roughly 5°C intervals. The data has been acquired using a 14-bit transient recorder. Sampling frequency of 50 kHz and 10,000 data points have been set for the whole static calibration process.

The calibration voltages are fit into a 1^{st} order linear curve of the form:

$$T = SV + O \tag{6.1}$$

where T and V denotes temperature and voltage, S stands for slope and O stands for offset.

For Gaussian-normal data distribution, which is the case for the data presented as verified using a probability plot and not presented here as the subject is beyond the scope of this study, the scatter in the data is

characterized by the standard deviation, s_X defined as:

$$s_X = \sqrt{\frac{\sum_{i=1}^{N} (X_i - \overline{X})^2}{N-1}} \tag{6.2}$$

i = data index
N = number of data points
X_i = value for data index i
$\overline{X}$ = sample average
$N-1$ = the degrees of freedom, ν, for a 1st order fit

The term s_X is given for a limited sample size, which is used to estimate the true standard deviation σ_X for an infinite population.

Random uncertainty, defined as the standard deviation of the average, $\sigma_{\overline{X}}$ is then estimated by $s_{\overline{X}}$ given in eq. (6.3).

$$s_{\overline{X}} = \frac{s_X}{\sqrt{N}} \tag{6.3}$$

Combining the systematic and random terms, the uncertainty according to the U_{95} model, where 95 stands for 95% confidence, is given as:

$$U_{95} = \pm t_{95} \sqrt{b^2 + s_{\overline{X}}^2} \tag{6.4}$$

where

b =systematic uncertainty term
t_{95} =t-distribution value for 95% confidence interval and ν degrees of freedom (see Table 6.1)

The t-distribution values for selected values of confidences for various degrees-of-freedom are given in Table 6.1. In the U_{95} uncertainty model, values on the 2nd column given in the table, representing values for 95%

confidence are utilized. Similarly the confidence level may be adjusted by selecting the appropriate column (e.g. selecting values from 5^{th} column for 99.5% confidence). For the sake of simplicity, the t-distribution value for 95% confidence, t_{95} is taken as 2.00 for systems with degree-of-freedoms higher than 30.

For the thermocouple calibration presented in this section, the system has 10 degrees-of-freedom with a t_{95} value of 2.228, while the systematic uncertainty value, b, of the reference thermometer used is 0.1°C. The standard deviation, s_X, is found to be 0.28°C and finally the random uncertainty $s_{\overline{X}}$ is calculated as 0.08°C. Plugging all these values into eq. (6.4) the thermocouple uncertainty for 95% confidence is found to be 0.29°C. The value evaluated without the t_{95} term is 0.13°C, which is used together with the degree-of-freedom information in the later stage of the uncertainty analysis where the thermocouple calibrated is used as the temperature reference instead of a thermometer.

Following the thermocouple calibration, The calibrated thermocouple is installed on a pressure vessel together with the pressure probe which in turn is placed inside the oil bath. The vessel is connected to a Druck DPI-610 pressure calibrator with a stated uncertainty value of 0.5 mbar. The calibrator is zeroed while the atmospheric pressure level is recorded using a Druck DPI-150 indicator with a stated uncertainty value of 0.75 mbar. It is important to note that these values noted on calibration certificates without any degree-of-freedom information are considered to have infinite degrees-of-freedom as explained by Dieck [16].

A standard pressure calibration in the range of 0-2000 mbar gauge with intervals of 200 mbar has been repeated at 5 temperature levels between 20 and 60°C in order to accomplish the static calibration, yielding 55 calibration points. Due to certain sealants and chemicals used in probe construction, the temperature calibration range could not be extended although the front end of the pressure sensor may experience higher temperatures. The absolute pressure is obtained by adding the atmospheric pressure and the gauge pressure

The temperature output of the instrumentation amplifier is denoted V_s while the pressure output is called V_p. At the end of the calibration, data is sorted to construct two surfaces, one for gauge pressure ($P =$

Table 6.1: Values for t-distributions with ν degrees of freedom for various confidence levels

ν	90%	95%	98%	99%	99.5%	99.8%	99.9%
1	6.314	12.71	31.82	63.66	127.3	318.3	636.6
2	2.920	4.303	6.965	9.925	14.09	22.33	31.60
3	2.353	3.182	4.541	5.841	7.453	10.21	12.92
4	2.132	2.776	3.747	4.604	5.598	7.173	8.610
5	2.015	2.571	3.365	4.032	4.773	5.893	6.869
6	1.943	2.447	3.143	3.707	4.317	5.208	5.959
7	1.895	2.365	2.998	3.499	4.029	4.785	5.408
8	1.860	2.306	2.896	3.355	3.833	4.501	5.041
9	1.833	2.262	2.821	3.250	3.690	4.297	4.781
10	1.812	2.228	2.764	3.169	3.581	4.144	4.587
11	1.796	2.201	2.718	3.106	3.497	4.025	4.437
12	1.782	2.179	2.681	3.055	3.428	3.930	4.318
13	1.771	2.160	2.650	3.012	3.372	3.852	4.221
14	1.761	2.145	2.624	2.977	3.326	3.787	4.140
15	1.753	2.131	2.602	2.947	3.286	3.733	4.073
16	1.746	2.120	2.583	2.921	3.252	3.686	4.015
17	1.740	2.110	2.567	2.898	3.222	3.646	3.965
18	1.734	2.101	2.552	2.878	3.197	3.610	3.922
19	1.729	2.093	2.539	2.861	3.174	3.579	3.883
20	1.725	2.086	2.528	2.845	3.153	3.552	3.850
21	1.721	2.080	2.518	2.831	3.135	3.527	3.819
22	1.717	2.074	2.508	2.819	3.119	3.505	3.792
23	1.714	2.069	2.500	2.807	3.104	3.485	3.767
24	1.711	2.064	2.492	2.797	3.091	3.467	3.745
25	1.708	2.060	2.485	2.787	3.078	3.450	3.725
26	1.706	2.056	2.479	2.779	3.067	3.435	3.707
27	1.703	2.052	2.473	2.771	3.057	3.421	3.690
28	1.701	2.048	2.467	2.763	3.047	3.408	3.674
29	1.699	2.045	2.462	2.756	3.038	3.396	3.659
30	1.697	2.042	2.457	2.750	3.030	3.385	3.646
60	1.671	2.000	2.390	2.660	2.915	3.232	3.460
∞	1.645	1.960	2.326	2.576	2.807	3.090	3.291

$f(V_s, V_p)$) and one for temperature ($T = f(V_s, V_p)$), and a surface fit has been obtained as expressed in equations 6.5 and 6.6. The resulting calibration surfaces are presented in Figure 6.1.

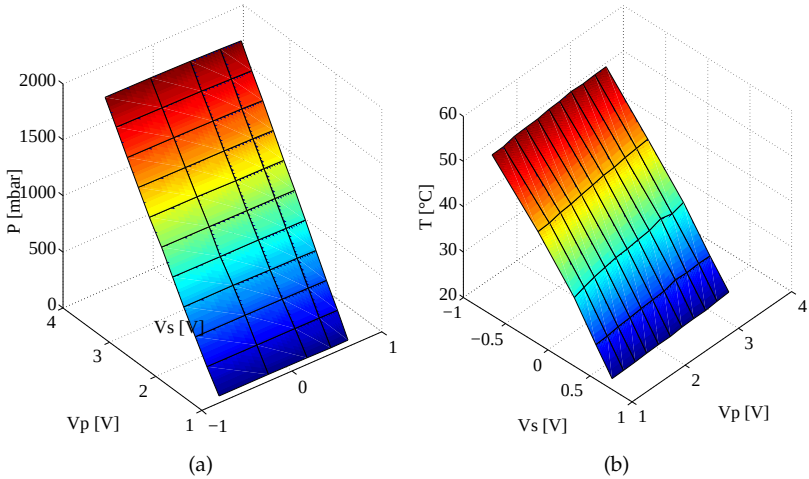

Figure 6.1: Static calibration pressure and temperature maps

$$P_{gauge} = c_1 + c_2 V_p + c_3 V_s V_P + c_4 V_s + c_5 V_s^2 \tag{6.5}$$

$$T = c_6 + c_7 V_p + c_8 V_s V_p + c_9 V_s + c_{10} V_s^2 \tag{6.6}$$

The random uncertainty of such a fit is estimated using 'standard estimate of error' or SEE which is defined as given in eq. (6.7) instead of s_X given in eq. (6.2).

$$SEE_{\mathbb{M}} = \sqrt{\frac{\sum_{i=1}^{N} (\mathbb{M}_i - \mathbb{M}_{fit,i})^2}{N - K}} \tag{6.7}$$

where

$$\begin{aligned}
\mathbb{M} &= \text{fitted parameter (i.e. } P_{gauge}, T) \\
\mathbb{M}_i &= \text{measured point} \\
\mathbb{M}_{fit,i} &= \text{value calculated from fit at point } i \\
K &= \text{number of coefficients of the fit (i.e. 5)} \\
N - K &= \text{the degrees of freedom, } \nu \text{, for the data fit}
\end{aligned}$$

Accordingly, the random uncertainty term $s_{\overline{X}}$ becomes:

$$s_{\overline{\mathbb{M}}} = \frac{SEE_{\mathbb{M}}}{\sqrt{N}} \tag{6.8}$$

The uncertainty for 95% confidence on pressure may therefore be written as:

$$U_{95_P} = \pm t_{95_P} \sqrt{b_P^2 + s_{\overline{P}}^2} \tag{6.9}$$

where $s_{\overline{P}}$ is calculated from eq. (6.8) as 0.16 mbar with $\nu_P = 225 - 5 = 220$ yielding a t_{95} value of 2. In order to compute the systematic uncertainty term b_P, one has to combine the stated uncertainties of two standards used in the calibration, the calibrator (0.5 mbar) and the atmospheric pressure indicator (0.75 mbar). The combined systematic uncertainty term achieved by root-sum-squaring the two contributing terms, is given in eq. (6.10) and is calculated as 0.90 mbar.

$$b_P = \sqrt{b_{DruckDPI610}^2 + b_{DruckDPI150}^2} \tag{6.10}$$

The uncertainty for absolute pressure for 95% confidence (i.e. 19:1 odds) is found to be 1.83 mbar.

Similarly the random uncertainty term for temperature is calculated as 0.04°C. Recalling the fact that a calibrated thermocouple with known degree-of-freedom is used as reference for the temperature calibration of the pressure probe, the combined degree-of-freedom value has to be

calculated for the uncertainty on temperature. The combined degree-of-freedom is calculated as 12 for temperature with the Welch-Satterthwaite approximation given in eq. (6.11).

$$\nu_{combined} = \frac{\left[\sum_{i=1}^{N}(b_i)^2 + \sum_{j=1}^{N}(s_{\overline{\mathbb{M}},j})^2\right]^2}{\left[\sum_{i=1}^{N}\frac{(b_i)^4}{\nu_i} + \sum_{j=1}^{N}\frac{(s_{\overline{\mathbb{M}},j})^4}{\nu_j}\right]} \tag{6.11}$$

where

$\nu_{combined}$ =number of degrees-of-freedom for the calibration result uncertainty

ν_i =degrees-of-freedom for the systematic uncertainty term

(i.e. for the reference thermocouple)

ν_j =degrees-of-freedom for the random uncertainty (i.e. N-K) for a data fit

It is of crucial importance to mention that the systematic uncertainty value used for this calculation is 0.13°C, which is the value calculated without the t_{95} term.

The calibration uncertainty value for temperature is then calculated similar to the pressure uncertainty term using eq. (6.12), and found to be 0.3°C for 95% confidence.

$$U_{95_T} = \pm t_{95_T}\sqrt{b_T^2 + s_{\overline{T}}^2} \tag{6.12}$$

6.1.2 Dynamic Calibration

The probe was tested in the VKI shock-tube facility in order to determine the transfer function and the natural frequencies of the screen-cavity system and the diaphragm. The experimental transfer function with respect to a theoretical step function obtained using shock-tube tests reveals the fundamental screen-cavity resonance around 63 kHz as seen in Figure 6.2. This mode is in line with the predictions obtained using the in-house code PreMeSys based on the line-cavity theory of Bergh & Tijdeman [6], presented in Figure 6.3.

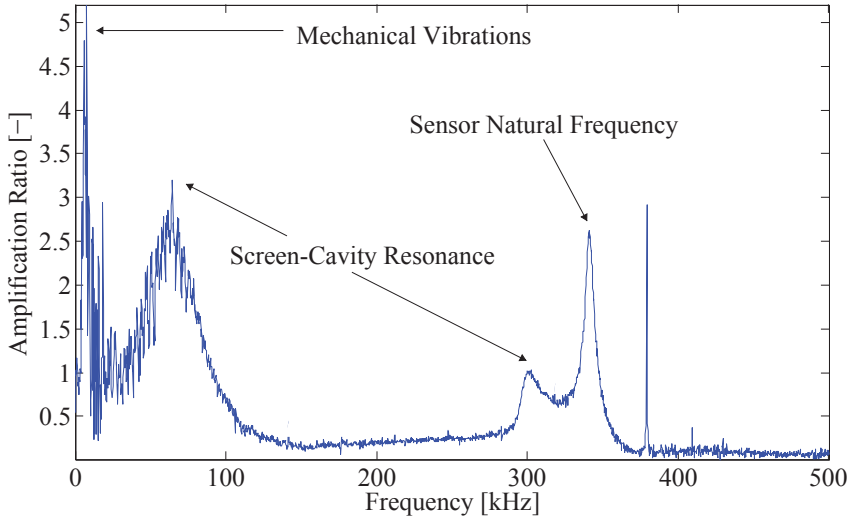

Figure 6.2: Frequency transfer function from the shock tube test of the probe tested

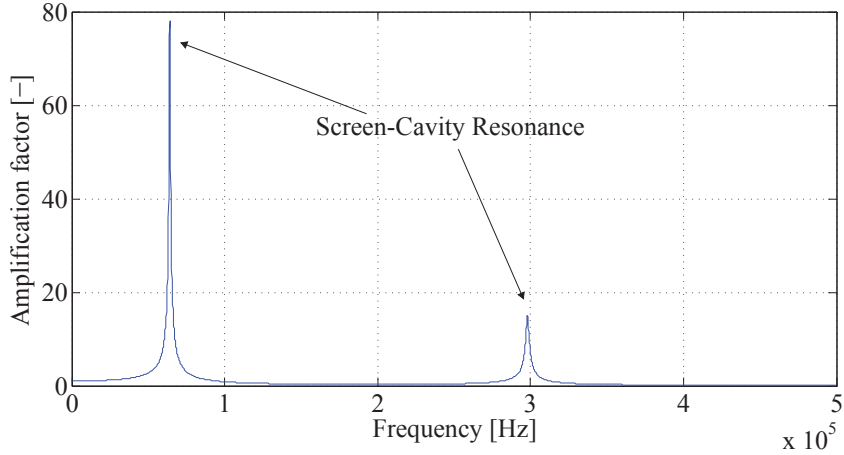

Figure 6.3: Frequency transfer function obtained with PreMeSys for the probe tested

PreMesys code does not allow an exact modeling of the screen, requiring one single diameter value for the line used. In order to overcome this limitation, an equivalent diameter for the 8 holes of the sensor screen is calculated in order to result in the same cross-sectional area. As the cavity volume in between the screen and the sensor membrane can not be measured directly, the cavity volume value is altered until a matching frequency of the first peak between PreMeSys result and the shock-tube test is achieved.

As it may be seen in Figure 6.3, the line-cavity system formed by the sensor-screen arrangement results in two peaks, one at $\sim$63 kHz and one in $\sim$300 kHz, in the frequency range of interest (i.e. 1 MHz) which are also clearly visible in the shock-tube test results. The lower frequency peak around 10 kHz seen in Figure 6.2 is due to mechanical vibrations either from the shock-tube itself, or from the probe–shock-tube interface. The sensor natural frequency is found to be $\sim$343 kHz.

6.1.3 Aerodynamic Calibration

Following the static calibration, the cooled probe was placed in the VKI-C4 open-jet calibration facility in order to determine the pressure recovery distribution with respect to the yaw angle. The probe has been yawed within a $\pm 90^\circ$ range for various freestream Mach numbers with a step of 2°. In Figure 6.4, given for a Mach number of 0.3, the pressure recovery ratio is on the ordinate whereas the yaw angle is the abscissa.

The pressure recovery ratio, C_p, is a measure of the total pressure recovered by the probe as given in eq. (6.13). A value of 1 indicates full total pressure recovery, where a value of 0 corresponds to a static pressure measurement. While negative values indicate a suction, a value above 1 is not physical. In an open-jet calibration nozzle, the static pressure is equal to the ambient pressure of the discharge environment, which corresponds to the atmospheric pressure in the VKI C-4 facility. Production errors such as impossibility of aligning the sensor element perfectly with the probe's geometric zero results in a shift of the calibration curve as seen in Figure 6.4, underlining the importance of an aerodynamic calibration even if the probe will be utilized perfectly centered to the flow direction.

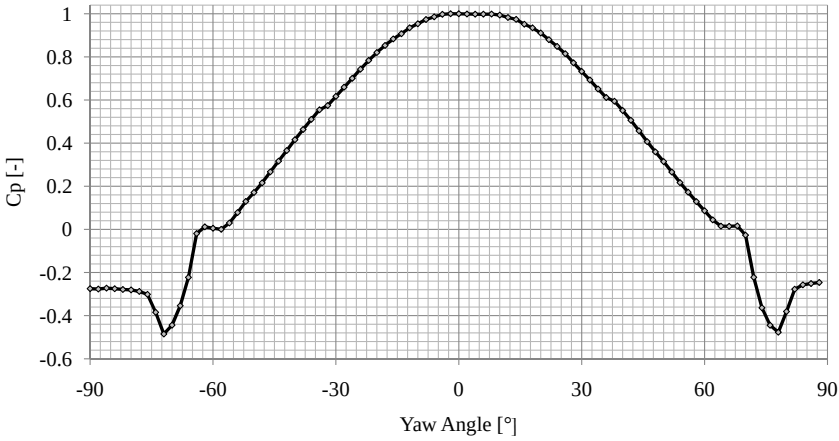

Figure 6.4: Yaw calibration in the VKI-C4 Calibration Facility, Pressure recovery ratio plot, M=0.3

$$C_{p_o} = \frac{P_{o,probe} - P_s}{P_o - P_s} \tag{6.13}$$

The uncertainty analysis for the aerodynamic calibration is slightly more complicated than it is for the static calibration. In the static calibration, the probe has been calibrated against a reference, such as the pressure calibrator, with a given uncertainty value. However, in the case of the aerodynamic calibration, the value for the pressure recovery ratio, C_{p_o}, is derived using values emanating from an atmospheric pressure indicator, a transducer measuring chamber pressure of the calibration nozzle and the transducer in the pressure probe itself.

In the lack of a calibration reference for C_{p_o} The systematic uncertainty terms are propagated using a Taylor's series expansion as shown below in eq. (6.14), where the terms $\delta P_{o_{probe}}$, δP_o and δP_{atm} are the uncertainty without the t-distribution value for the probe, the chamber pressure and the atmospheric pressure indicator respectively.

$$b_{c_{P_o}} = \sqrt{\left(\frac{\partial c_{P_o}}{\partial P_{o_{probe}}}\delta P_{o_{probe}}\right)^2 + \left(\frac{\partial c_{P_o}}{\partial P_o}\delta P_o\right)^2 + \left(\frac{\partial c_{P_o}}{\partial P_{atm}}\delta P_{atm}\right)^2} \quad (6.14)$$

By evaluating the partial derivates in eq. (6.14), one obtains:

$$b_{c_{P_o}} = \left[\left(\frac{1}{(P_o - P_{atm})}\delta P_{o_{probe}}\right)^2 + \left(\frac{(P_{o_{probe}} - P_{atm})}{(P_o - P_{atm})^2}\delta P_o\right)^2 + \left(\frac{(P_{o_{probe}} - P_s) - (P_o - P_{atm})}{(P_o - P_{atm})^2}\delta P_{atm}\right)^2\right]^{1/2} \quad (6.15)$$

Once the values are substituted, the systematic uncertainty term for the total pressure recovery ratio is calculated as 0.0023.

In order to evaluate the random uncertainty values, a curve of the form given in eq. (6.16) is fit to the distribution presented in Figure 6.4, which is also used for evaluating the values of C_{p_o} at different yaw angles.

$$c_{P_{o_{fit}}} = \sum_{i=1}^{8} c_{1_i} Sin(c_{2_i}\phi + c_{3_i}) \quad (6.16)$$

The standard estimate of error is then calculated as:

$$SEE_{c_{P_o}} = \sqrt{\frac{\sum_{i=1}^{N}(c_{P_o i} - c_{P_{o_{fit_i}}})^2}{N - K}} \quad (6.17)$$

The random uncertainty term is then written as:

$$s_{\overline{c_{P_o}}} = \frac{SEE_{c_{P_o}}}{\sqrt{N}} \quad (6.18)$$

where N=91 for the calibration and K=24, corresponding to 24 coefficients of the curve fit. The random uncertainty term is calculated as 0.0005.

When the static pressure level is unknown, as in typical test environment, instead of C_{p_o}, an alternate total pressure recovery term may be defined as given in eq. (6.19), and plotted in Figure 6.5.

$$K_{P_o} = \frac{P_o - P_{o_{probe}}}{P_o} \tag{6.19}$$

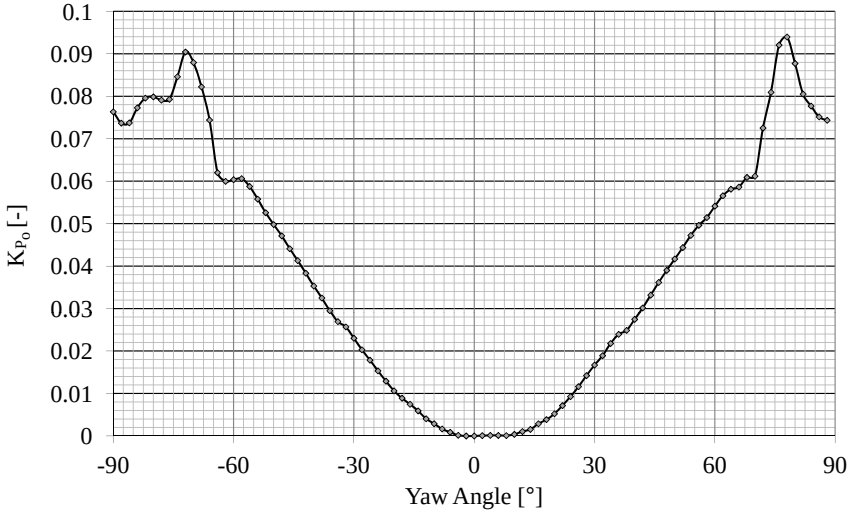

Figure 6.5: Yaw calibration in VKI-C4 Calibration Facility, K_{P_o} plot, M=0.3

In order to quantify the uncertainty, again the problem is tackled in two groups, the systematic and random uncertainty contributions. The systematic uncertainty is once again propagated using Taylor's series expansion as given in eq. (6.20).

$$b_{K_{P_o}} = \sqrt{\left(\frac{\partial K_{P_o}}{\partial P_o}\delta P_o\right)^2 + \left(\frac{\partial K_{P_o}}{\partial P_{o_{probe}}}\delta P_{o_{probe}}\right)^2} \tag{6.20}$$

The maximum systematic uncertainty is calculated as 0.0017. In order to determine random uncertainties, once again the curve presented in Figure 6.5 has been fit using an equation of the form:

$$K_{P_{o_{fit}}} = \sum_{i=1}^{8} c_{1_i} Sin(c_{2_i}\phi + c_{3_i}) \tag{6.21}$$

The standard estimate of error is then calculated just as before in eq. (6.17) as:

$$SEE_{K_{P_o}} = \sqrt{\frac{\sum_{i=1}^{N} (K_{P_o i} - K_{P_{o_{fit}}})^2}{N - K}} \tag{6.22}$$

The random uncertainty term is then written as:

$$s_{\overline{K_{P_o}}} = \frac{SEE_{K_{P_o}}}{\sqrt{N}} \tag{6.23}$$

where N=91 for the calibration and K=24, corresponding to 24 coefficients of the curve fit. The random uncertainty term for K_{P_o} is calculated as 0.0002. the uncertainty on K_{P_o} for 95% confidence is then calculated as 0.0031.

The total pressure may then be reconstructed according to the following formula:

$$P_o = \frac{P_{o_{probe}}}{1 - K_{P_o}} \tag{6.24}$$

After applying the aerodynamic calibration, one may evaluate the uncertainty on reconstructed total pressure by propagating the uncertainty as:

$$\delta P_o = \sqrt{\left(\frac{\partial P_o}{\partial P_o}\delta P_{o_{probe}}\right)^2 + \left(\frac{\partial P_o}{\partial P_o}\delta K_{P_o}\right)^2} \tag{6.25}$$

After substituting the partial derivate terms, one obtains:

$$\delta P_o = \sqrt{\left(\frac{1}{1-K_{P_o}}\delta P_{o_{probe}}\right)^2 + \left(\frac{-P_{o_{probe}}}{(1-K_{P_o})^2}\delta K_{P_o}\right)^2} \tag{6.26}$$

In order to evaluate the total uncertainty, one needs the values of pressure level measured by the probe and the yaw angle, as it may be seen in eq. (6.26).

The total pressure recovery ratio allows correcting the total pressure values measured when the relative flow angle is known; and furthermore, allows to operate the probe in the virtual 3-hole mode, which is explained later in section 6.2.4, yielding a number of additional flow parameters including yaw angle, static pressure and Mach number.

6.2 Gas Turbine Exhaust Measurements

6.2.1 Experimental Set-Up

The very first testing opportunity for the probe and the cooling system in an industrial environment was provided by Rolls-Royce plc within the EU-FP6 HEATTOP project. A two-day long testing slot was made available on the Viper Mk.201 test engine, shown in Figure 6.6.

The Viper turbojet engine has originally been designed by Armstrong-Siddeley and renamed as Bristol-Siddeley and Rolls-Royce Viper through company acquisitions. The engine has entered service in 1953 and remained in use until 2011 with Hawker Siddeley Dominie T1, a BAe 125/de Havilland DH125 variant, aircraft of the British Royal Air Force. It has found wide applications in BAC Jet Provost trainer, GAF Jindivik target drone, Bell X-14 VTOL aircraft, Handley Page HP.115 delta-wing research aircraft and Aeromacchi MB-326 light military jet aircraft to name a few.

The engine, rated for 12 kN at 13,800 rpm, has a length of 1,625 mm and a frontal diameter of 624 mm and weighs 249 kg. It has an axial

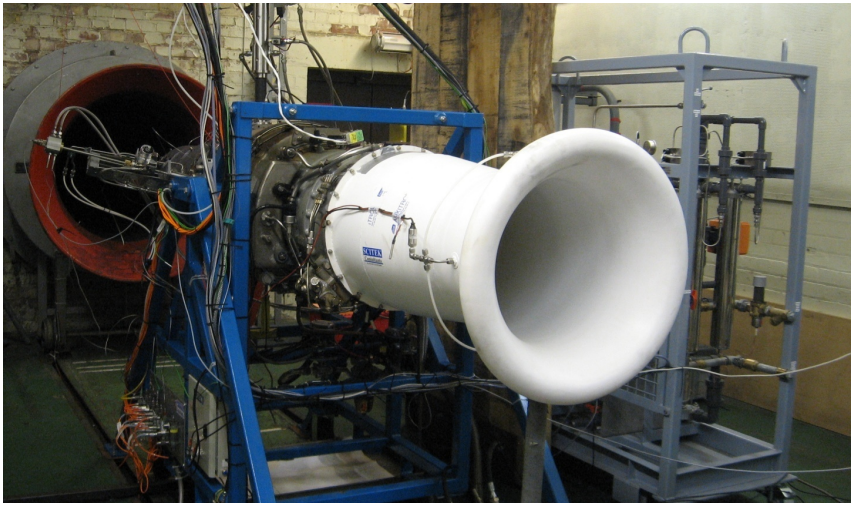

Figure 6.6: Photograph of the Rolls-Royce Viper test engine

compressor comrised of 7 stages, with an annular combustion chamber comprising 24 burners, and has a single stage turbine.

The traverse gear arrangement mounted on the turbine casing is shown in Figure 6.7 where the probe head from the rear side of the engine jet pipe behind the turbine rotor is shown in Figure 6.8. The probe was installed approximately 3 axial chords downstream of the turbine and traversed radially over approximately 75 mm as shown in Figure 6.9.

The probe was calibrated in pressure and temperature in the laboratory before the test campaign, as explained above in section 6.1, and an additional static pressure calibration was performed on site before the tests to ensure the validity of calibration.

A summary of the testing conditions is provided in Table 6.2 together with the main operational conditions for the probe. Tests were performed starting at idle, performing traverses respectively at 8000, 10000 RPM, and full throttle. At full throttle, the turbine speed is approximately 12800 RPM and the exhaust gases reach a temperature of 750°C as measured by jet pipe thermocouples. The probe survived all tests including the full throttle conditions. However due to severe noise in-

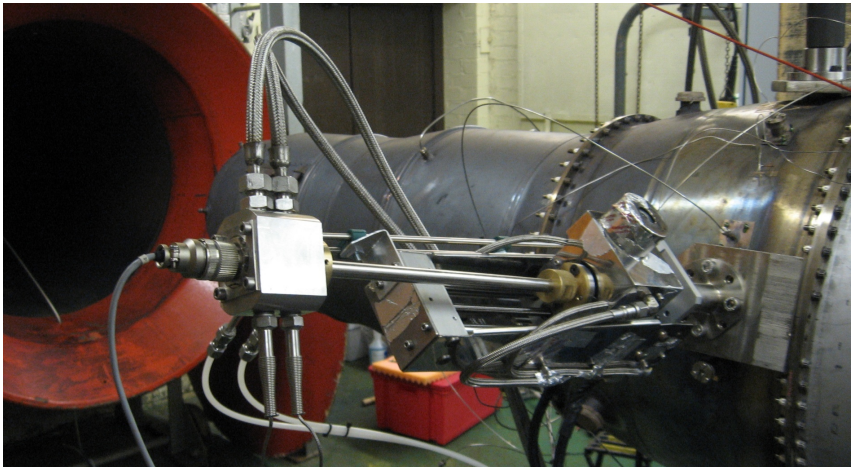

Figure 6.7: Photograph of the probe installed on the traverse gear mounted on the Viper turbine casing

Figure 6.8: Photograph of the probe inside the Viper engine jet pipe

terferences on the electronics, no pressure data could be retrieved at full-thrust conditions. This motivated the use of a Faraday cage in further test campaigns to host amplifiers and data acquisition system as well as a UPS power supply including an isolation transformer to avoid interferences from the power grid.

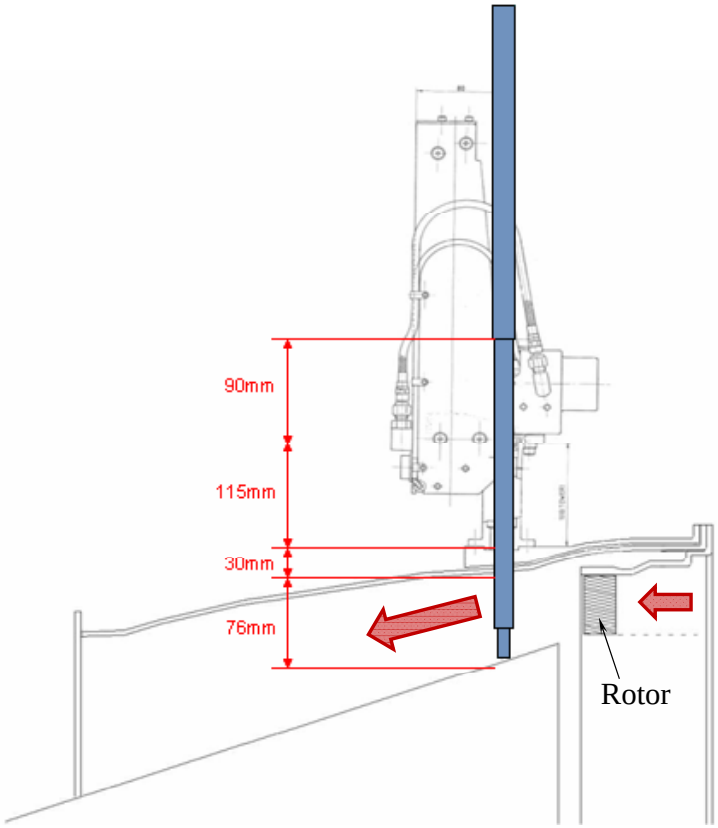

Figure 6.9: Schematic view of the probe traverse arrangement behind the Viper turbine rotor

6.2.2 Time-Averaged Measurement Results

The flow direction at part speed being unknown, the probe was traversed at zero degree set angle with respect to the machine axis. An example probe traverse is shown in Figure 6.10a in terms of time-averaged total pressure at 8000 and 10000 RPM, where the exhaust gas temperature was 440°C and 503°C respectively. With the cooling pressure and flow rates indicated in Table 6.2, the sensor diaphragm has reached a maximum temperature of 99.3°C and the corresponding sensor temper-

Table 6.2: Summary of test conditions and probe data for the Viper engine runs

Engine RPM	8000	10000	12800
Exhaust Gas Temp	440°C	480°C	750°C
Comp. Delivery Press.	1.67 bar	2.26 bar	3.6 bar
Cooling Mass Flow Rate	1.02 ℓ/min	1.13 ℓ/min	1.62 ℓ/min
Cooling Pressure	50 bar	60 bar	72 bar
Water In Temp.	19.25°C	20°C	22.2°C
Water Out Temp.	25.5°C	28.25°C	36.35°C
Heat Extracted	0.5 kW	0.7 kW	1.75 kW
Sensor Membrane Temp.	73.5°C	94.9°C	99.3°C

ature distribution is presented in Figure 6.10b.

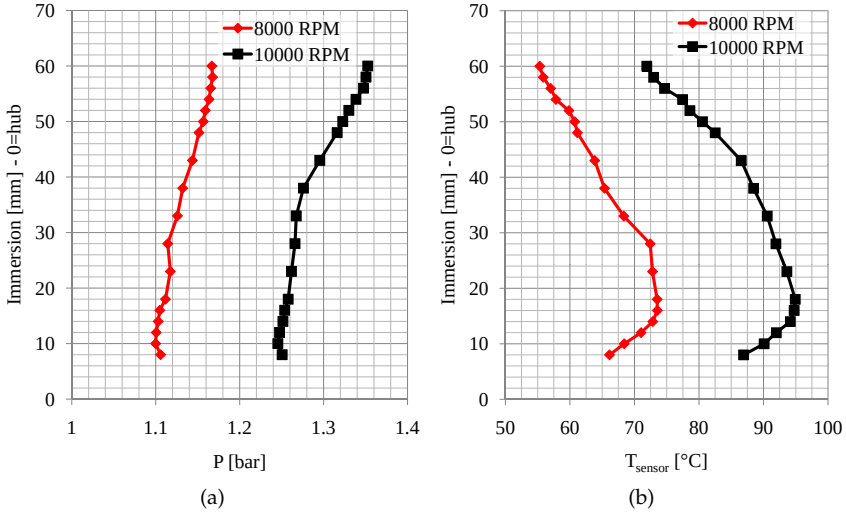

Figure 6.10: Average total pressure (left) and sensor temperature (right) distributions behind the rotor at 8000 RPM and 10000 RPM

At full throttle conditions, the cooling water temperature increase did not exceed 15°C, yielding a maximum heat power extracted of 1.75 kW

at almost full immersion.

Yawing the probe at a fixed immersion depth yields the typical bell curves expected from angular calibrations. As it can be seen from the corresponding curves of Figure 6.11 at 8000 and 10000 RPM, the probe shows an approximate angular insensitivity range of 15 degrees. The turbine exit absolute flow angle at this radial position can be assumed to be around -15° from this data.

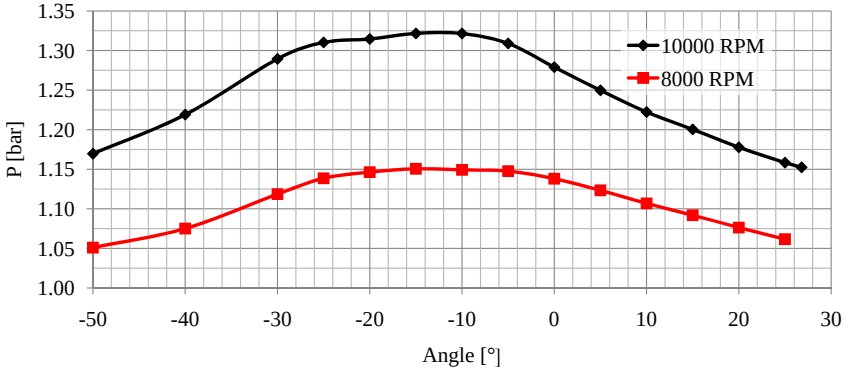

Figure 6.11: Probe angular response in engine at 8000 and 10000 RPM

6.2.3 Unsteady Measurement Results

The sensor signal was acquired on a high speed 14-bit data acquisition system at a sampling rate of 1 MHz. At full throttle conditions (12800 RPM), with 113 rotor blades, this yields a blade passing frequency of 23.9 kHz, i.e. a resolution of 42 points per blade passage. The maximum storage capacity of the system being 262144 points, more than 6241 blade passages were recorded, or 55 full rotor revolutions.

6.2.3.1 Frequency Analysis

The recorded signals are first analyzed in the frequency domain. Figure 6.12 shows the power spectrum of a recording during a traverse

at 10000 RPM. The fundamental frequency of blade passing, which is 18.84 kHz, can be clearly seen as well as 3 harmonics up to 75.36 kHz. Another very clear frequency peak can be seen around 340 kHz which is the diaphragm natural resonance frequency for the 25 psi sensor, very highly excited by the high blade passing frequency.

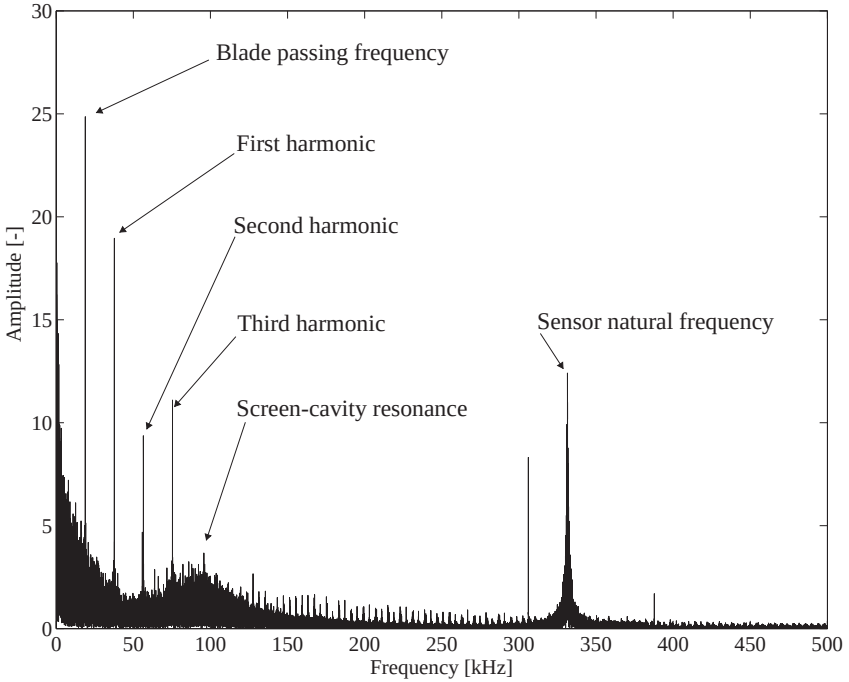

Figure 6.12: Single-sided amplitude spectrum of the signal recorded at 10000 RPM, immersion depth = 43 mm, $T_{gas} = 503°C$

The resonance in the 90 kHz range is attributed to the sensor screen cavity resonance. It has to be noted that the temperature of the gas in the recess cavity of the sensor-screen configuration affects the frequency response in such a way to increase the resonance frequency. As explained before in section 4.2.2, this phenomenon is governed by the Helmholtz equation, as given before in eq. (4.1) and repeated below:

$$f_n = \frac{a}{2\pi}\sqrt{\frac{\pi d^2}{4LV_c}}$$

In Figure 6.13, the increase in Helmholtz frequency is plotted versus temperature and compared to the screen-cavity resonance frequency calculated using PreMeSys. An average temperature inside the cavity in front of the sensor can then be determined on the basis of the frequency found in the probe spectrum under hot conditions. The three points on Figure 6.13 show the cavity temperature estimated from the natural frequency of the screen-cavity resonance obtained by frequency spectra using this principle. According to this plot, the cavity temperature is estimated approximately at 350°C, 470°C and 730°C at 8000, 10000 and 12800 RPM respectively whereas the respective gas turbine exhaust temperatures were 440°C, 505°C and 750°C.

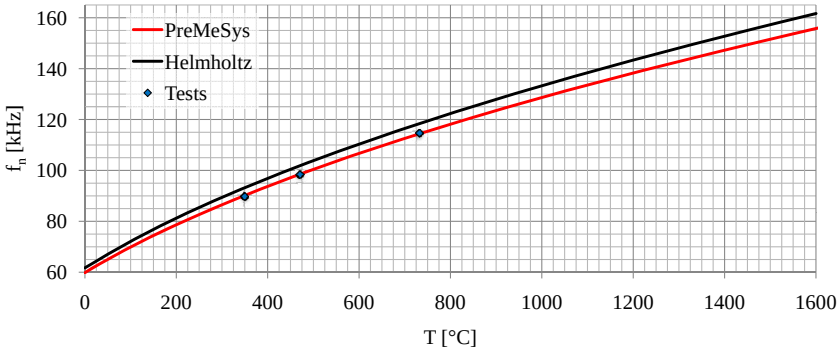

Figure 6.13: Comparison of screen-cavity resonance frequencies calculated using PreMeSys and Helmholtz formulation in eq. (4.1)

6.2.3.2 Raw Signal and Signal-to-Noise Ratio

Returning to the time domain, an example of raw signal is shown in Figure 6.14 over 10 blade passages. The simplest information to be extracted from the signal is of course the time averaged pressure level

presented in Figure 6.10a as well as the corresponding pressure fluctuations. These are presented in terms of RMS in Figure 6.15 along the radial traverses at 8000 and 10000 RPM. The overall pressure fluctuations are seen to increase with engine RPM and show a region of higher fluctuations in the hub region with peak values of 40 mbar at 10000 RPM.

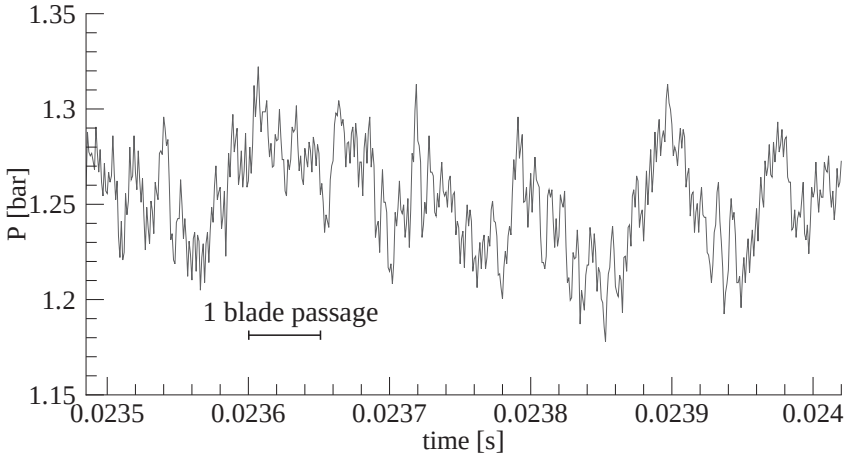

Figure 6.14: Example of raw pressure signal at 10000 RPM, immersion depth = 5 mm, $T_{gas} = 503°C$

The signal-to-noise ratio is generally defined as:

$$SN = 20\ log\ \left(\frac{RMS_{signal}}{RMS_{noise}}\right) \tag{6.27}$$

The RMS value of the noise is taken from recordings with no flow prior to the engine runs. After amplification, the background electronic noise on the sensor was found to remain below ± 3.52 mbar RMS without the engine running. This value was found to increase to ± 7.18 mbar when the engine was running, the probe being retracted which corresponds to approximately four times of the static calibration uncertainty. The hypothesis of no flow conditions on the sensor is of course questionable in this case. It was found that the triple-phase generator on the engine,

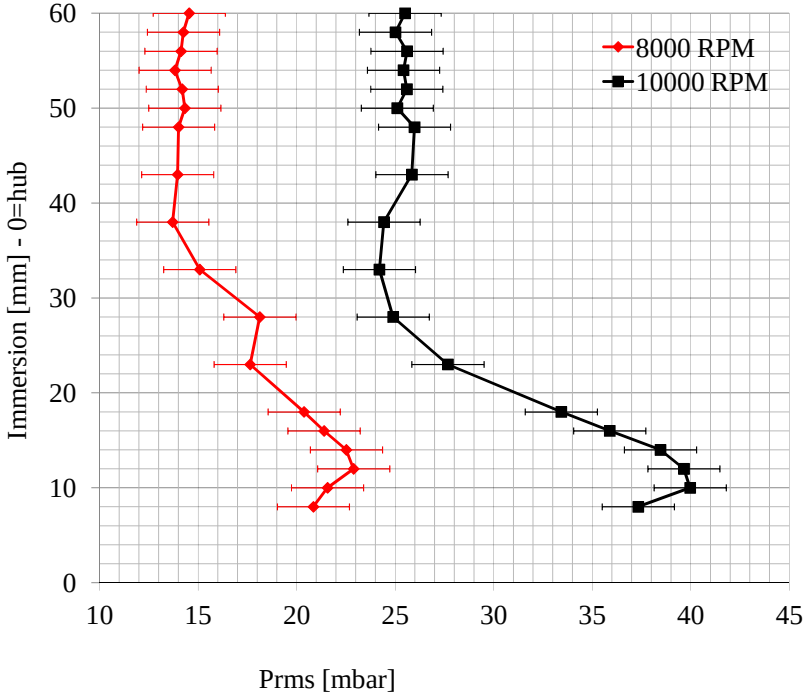

Figure 6.15: Pressure fluctuations at 8000 and 10000 RPM, $T_{gas} = 503°C$at 1000 RPM

also used to generate a once-per-rev signal, was introducing electric interferences on the sensor signal increasing with engine RPM.

The signal-to-noise ratios computed according to Equation 6.27 yield 14.32 when the engine was running at 10000 RPM, corresponding to $\sim$25 mbar RMS at midspan, which is found to be satisfactory.

6.2.3.3 Phase Locked Averaging

In order to retrieve the average pressure fluctuation over a blade passing period, a phase-locked averaging (PLA) is applied. The phase-locked averaging procedure applied to the raw data is based on the determination

of the highest peak, corresponding to the blade passing frequency, in the frequency spectrum of the signal. This value is used for determining the time period over which the signal is phase-locked averaged. This time period is then divided into N points which are chosen as the ratio of the sampling frequency to the blade passing frequency in an effort to match the number of points to the sampling rate. The phase-locked average of the signal is then calculated by interpolation of the raw signal at time steps defined by those N points within each blade passing period.

A great advantage of the probe designed is having the probe continuously immersed in the hot gas path, allowing the analysis of various effects such as length of the signal used at processing, effects of RPM variations, blade-to-blade non-uniformities or random unsteadiness of the flow.

An important factor is the determination of the signal length used for phase-locked averaging. Ideally, a once-per-revolution signal is used to correct for RPM variations during a recording by re-sampling the recorded pressure signal while performing phase-locked-average computations.

The Viper test rig is equipped with a once-per-revolution signal that emanates from a triple-phase generator on the engine and was reconstructed from one of the three sine waves, which is unfortunately unstable with respect to RPM. Therefore in this test, due to the lack of a reliable once-per-rev trigger signal, the variations in the engine speed could not be taken into account. Moreover, the phase information is lost.

In the absence of a trigger, the phase-locked averaging operations are performed for different lengths of the signal as shown in figure 6.16, and it is decided to use 2 revolutions corresponding to 226 blade passages.

The effects of filtering on the signal are also evaluated. Statistics, such as minimum, maximum and RMS of the phase-locked averages for raw, high-pass and low-pass filtered signals are shown in Figure 6.17.

RMS of the phase-locked averages are expressed using error bars. Applying a 10^{th} order low-pass Butterworth filter with a cut-off frequency of 250 kHz slightly reduces the RMS of the phase-locked average. On the other end of the spectrum, a 4^{th} order high-pass Butterworth filter

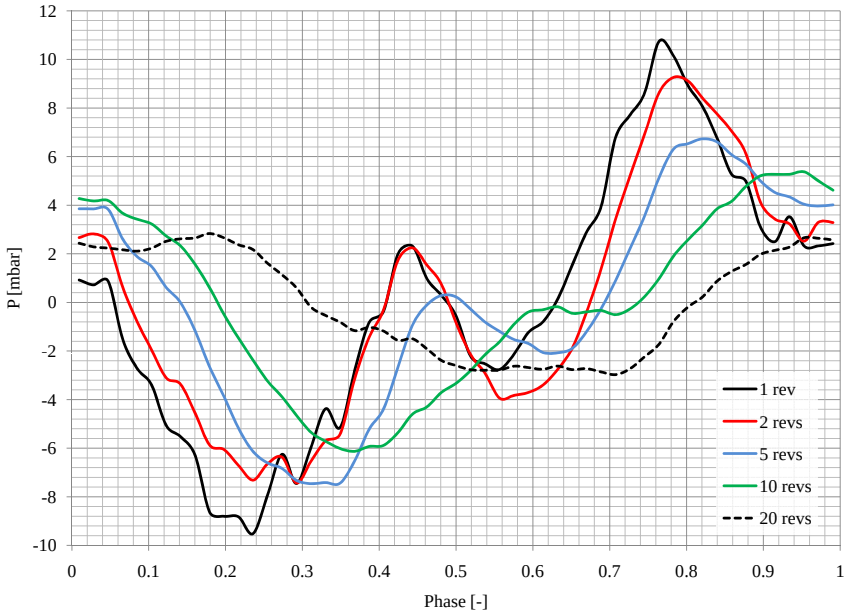

Figure 6.16: Phase-locked average of the pressure signal at 10000 RPM for different number of blade passages, immersion = 23 mm from hub, $T_{gas} = 503°C$

with a cut-off frequency of 10 kHz greatly reduces the RMS values as the low frequency content of the signal is also filtered out narrowing the min/max band. The low-pass filter applied only has a small effect on minimum and maximum values linked to the sensor natural frequency. It is worth to mention that the PLA of the three signals fit perfectly on top of each other.

The peak-to-peak value of the PLA is around $\sim$8 mbar (i.e. $\pm$4 mbar), a value far less than the RMS value of $\sim$25 mbar at the same location. This peak-to-peak value corresponds to the periodic content of the signal and may be influenced by factors such as the total number of passages taken into account for the statistics, blade-to-blade non uniform flow conditions and/or geometry, the scatter on the blade passing frequency peak in the power spectrum indicating the turbine rotational speed stability and finally a low frequency component in the signal. For these reasons

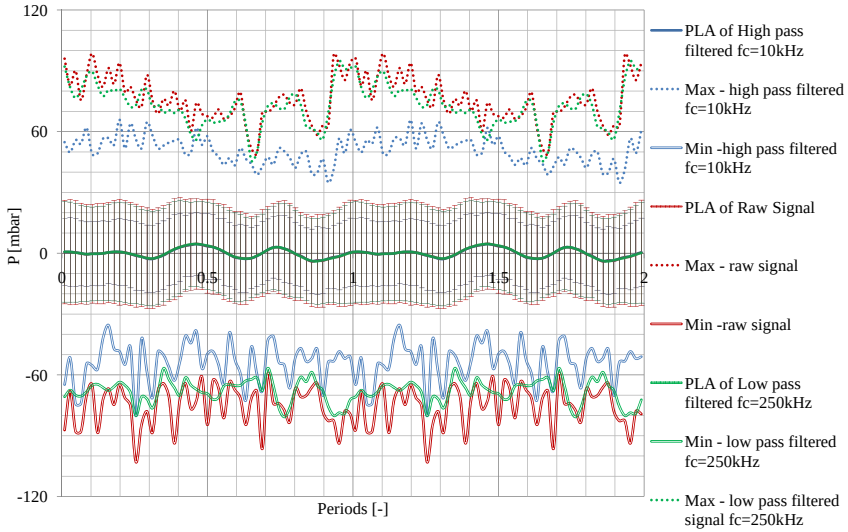

Figure 6.17: Phase-locked average of the pressure signal at 10000 RPM, immersion = 23 mm from hub, $T_{gas} = 503°C$

depicted, the phase-locked averaging is applied on the high-pass filtered signal.

In order to present the periodic component of the unsteady flow within a blade passage, the resulting phase-locked averages obtained from a radial traverse are combined. This is accomplished by creating a phase-span contour plot, showing the unsteady pressure contours over several blade passages or even over a full rotor revolution, as given in Figure 6.18 for the radial traverse at 10000 RPM.

6.2.4 Virtual Three-Hole Mode

Even though the probe developed is a single-sensor probe, its angular calibration properties may be further exploited as if a three-hole directional probe is utilized. As a matter of fact, by yawing the probe at two different symmetric angular positions, the recordings will be equivalent

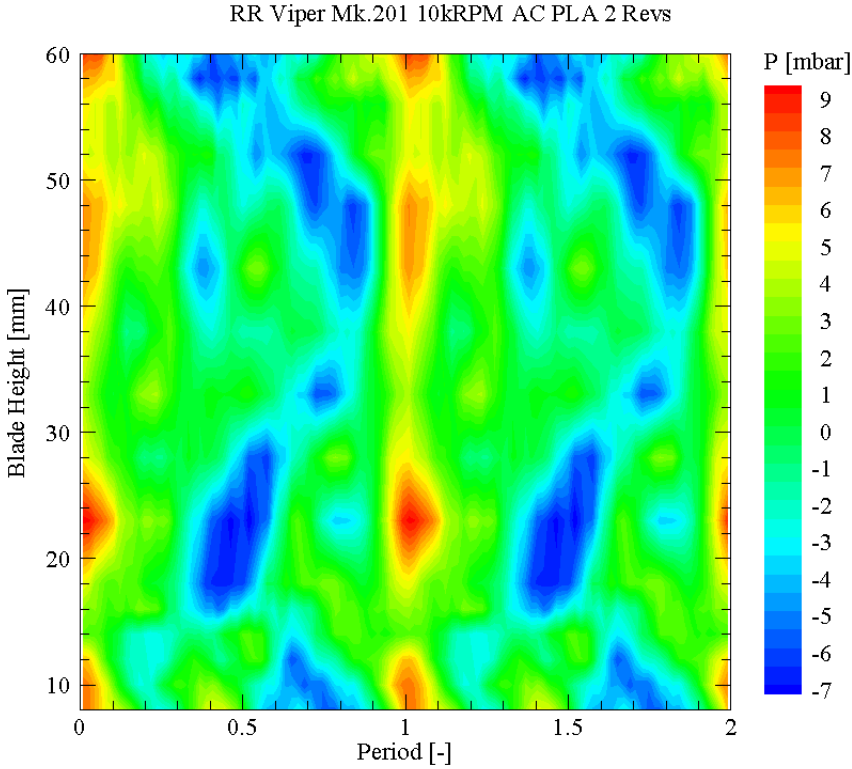

Figure 6.18: Phase-locked average map of the turbine exit total pressure at 10000 RPM, $T_{gas} = 503°C$

to those obtained from the left, right and center pressures of a conventional three-hole directional probe except for time-correlation.

The angular calibration curve of the virtual three-hole probe is obtained by shifting the angular calibration curve for the single hole probe, given above in Figure 6.4, by a pre-selected angular displacement. Lower values of the angular displacement results in reduced sensitivity, while higher values result in a limited calibration range for a fixed yaw range of the aerodynamic calibration. For the present study, this displacement between the three holes is chosen as 35°.

The yaw angle calibration coefficient for a three-hole probe, which is

purely numerically constructed, is given in eq. (6.28). The second term in the denominator, which is the arithmetic mean of the readings from the left and the right pressure holes represent the static pressure measured by the probe. The yaw angle calibration coefficient, K_{yaw}, representing the ratio of the pressure difference between two side holes with respect to the dynamic pressure measured by the probe is plotted with respect to the yaw angle in Figure 6.19. This coefficient allows the determination of the yaw angle using left, right and center pressure values from subsequent recordings at given angular increments.

$$K_{yaw}(\varphi) = \frac{P_L(\varphi) - P_R(\varphi)}{P_{o,probe}(\varphi) - \frac{P_L(\varphi)+P_R(\varphi)}{2}} \tag{6.28}$$

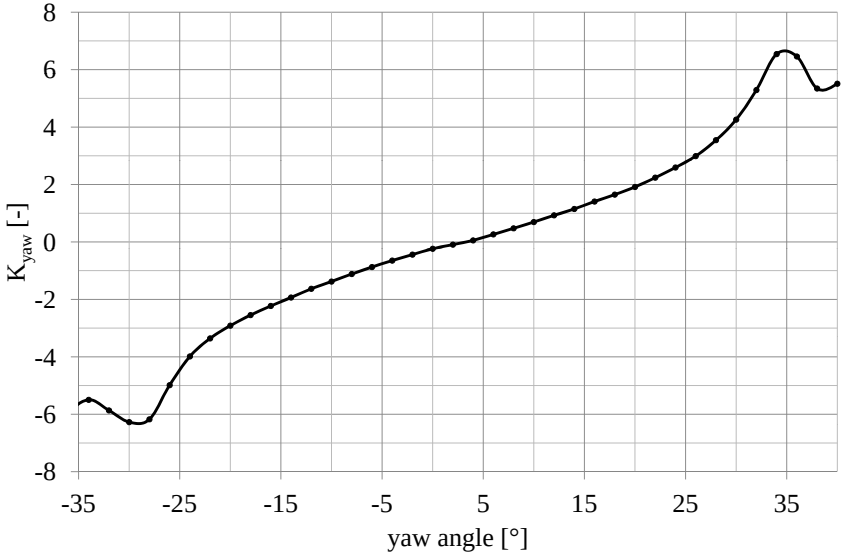

Figure 6.19: Yaw coefficient with respect to yaw angle for a probe setting angle of 35°

It is very important to mention that the recordings are not simultaneous. Hence, only the periodic content of the fluctuations can be retrieved, provided that the flow conditions remain constant. Therefore, it is impossible to apply the concept of a virtual three-hole probe in cases

where the rotational speed of the machine under study is not fixed and where a proper trigger signal ensuring measurements are done on the very same machine phase is not present.

For the reasons explained above, the calculations presented in this study should be taken as a demonstration of the capabilities of the probe developed and not a thorough unsteady turbine flow analysis on the Rolls-Royce Viper engine.

In the present case, the mean flow angle has been determined by yawing the probe within the hot gas path as previously shown in Figure 6.11. The flow angle is roughly determined to be around -15°. Using this information as an input, the unsteady pressure signals recorded at -50°, -15° and +20° are respectively chosen to be the left, center and right holes of the virtual three-hole pressure probe presented.

The unsteady yaw angle calculated by the aid of yaw angle calibration coefficient given in eq. (6.28) is presented as raw yaw angle distribution in Figure 6.20.

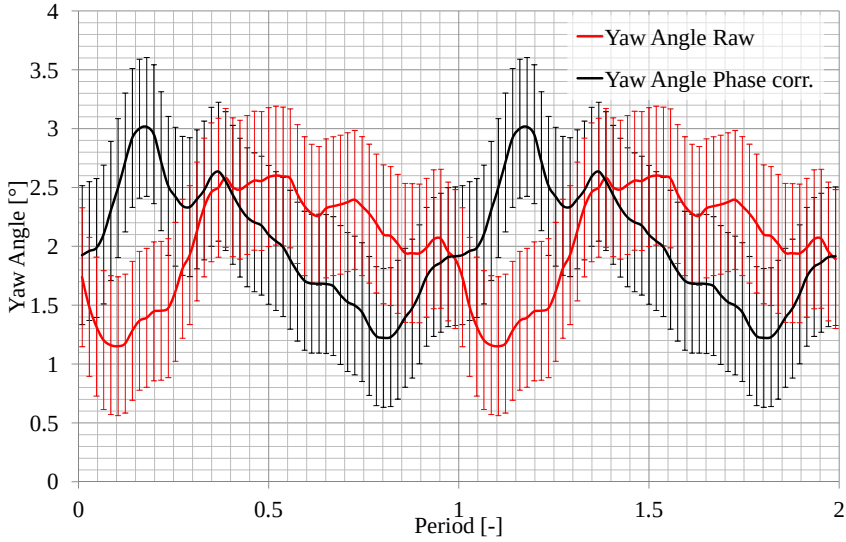

Figure 6.20: Unsteady yaw angle calculated – raw and phase shifted – at 10000 RPM, immersion = 23 mm from hub, T_{gas} = 503°C

In Figure 6.20 and the following graphs concerning the virtual-three-hole probe arrangement, two curves are presented for raw and phase-shifted quantities. The phase shifting procedure and its reasoning will be explained in detail in section 6.2.4.1.

With the knowledge of the unsteady yaw angles, values for the unsteady total pressure are corrected for non-zero incidence effects using the total pressure calibration coefficient, given in eq. (6.29). The corrected unsteady total pressure distribution is presented in Figure 6.21.

$$K_o(\varphi) = \frac{P_o - P_{o,probe}(\varphi)}{P_{o,probe}(\varphi) - \frac{P_L(\varphi)+P_R(\varphi)}{2}} \tag{6.29}$$

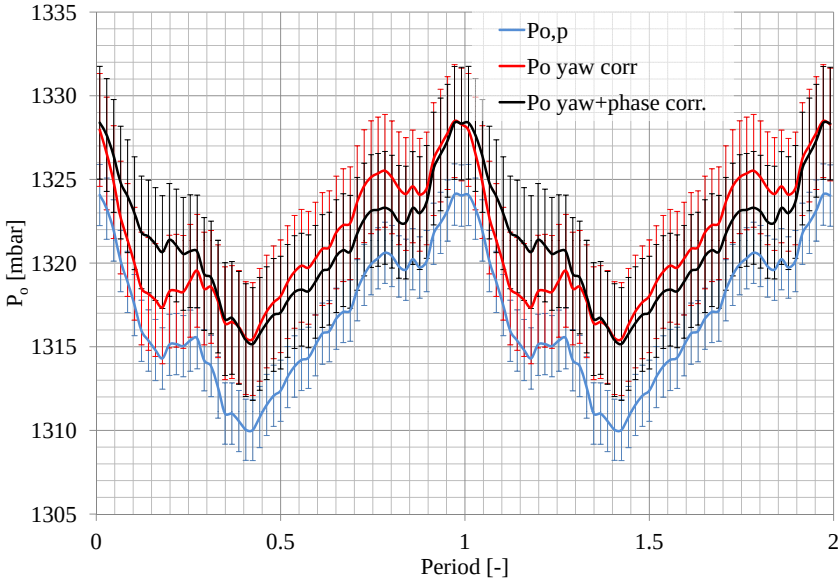

Figure 6.21: Total pressure distribution – Raw, Corrected for yaw angle, Corrected for phase shift and yaw angle – at 10000 RPM, immersion = 23 mm from hub, $T_{gas} = 503°C$

Using the virtual three-hole mode, one may also exploit the Mach number from a given set of data by defining a dynamic pressure calibra-

tion coefficient and a static pressure calibration coefficient as shown in eq. (6.30) and eq. (6.31) respectively.

$$q_{probe}(\varphi) = P_{o,probe}(\varphi) - \frac{P_L(\varphi) + P_R(\varphi)}{2} \tag{6.30}$$

$$K_{stat}(\varphi) = \frac{P_o - P_s}{q_{probe}(\varphi)} \tag{6.31}$$

Using the dynamic pressure coefficient, the corrected total pressure and the static calibration coefficient defined in eq. (6.31), the static pressure is calculated as shown in Figure 6.22.

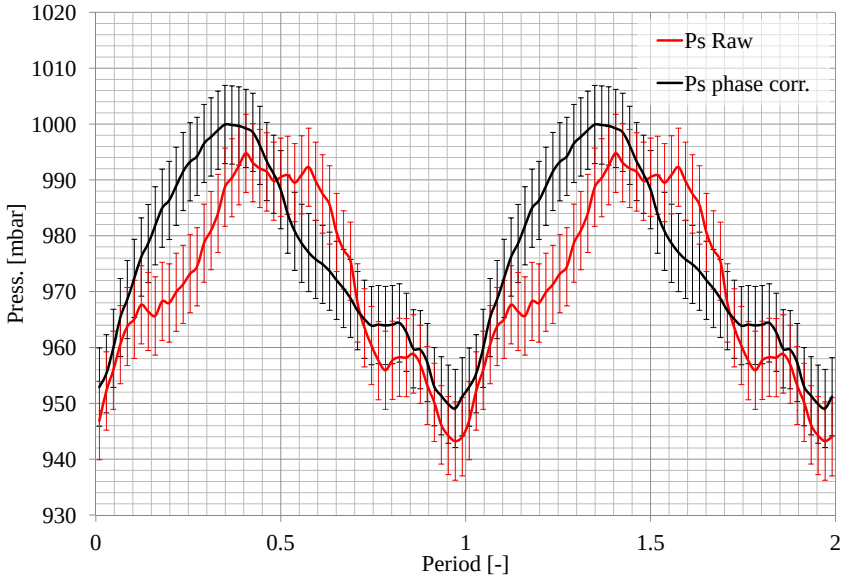

Figure 6.22: Pseudo-static pressure distribution at 10000 RPM, immersion = 23 mm from hub, $T_{gas} = 503°C$

The obtained static pressure together with the total pressure is then fed into an isentropic flow relation in order to calculate the unsteady Mach number, given in Figure 6.23.

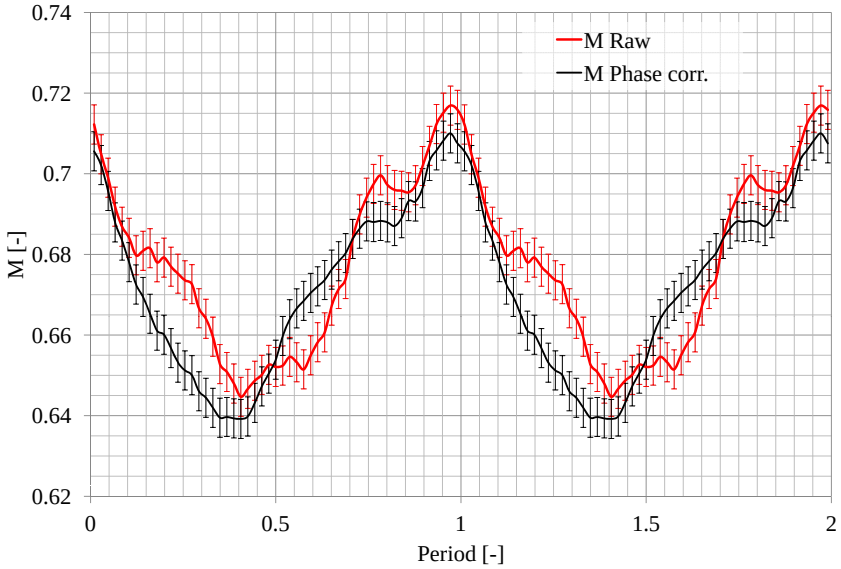

Figure 6.23: Mach number distribution at 10000 RPM, immersion = 23 mm from hub, $T_{gas} = 503°C$

6.2.4.1 Phase Correction

It is crucial to ever remember that the virtual holes are not at the same position with the center hole. Hence, the left and right virtual holes are experiencing blade arrival events at different phases compared to the central hole. Applying the corresponding phase shift of ∼19.270% of a blade pitch to the left and right recordings yields the phase corrected unsteady yaw angle curve in Figure6.20. Using this curve, the phase corrected curves for unsteady total pressure, static pressure and Mach number are re-calculated, as previously shown in corresponding Figures 6.21, 6.22 and 6.23.

6.2.4.2 Blockage Effects

Many of the unsteady aerodynamic errors affecting fast response pressure probes such as added mass effects, unsteady lift, dynamic stall,

von Karman vortex interactions, et cetera are proportional to probe size for a given probe geometry. Cylindrical probes have been shown to be the least sensitive to these errors as explained by Kupferschmiedet al. [35] and Humm [27]. However in the present case, blockage effects and phase corrections are mandatory, even if one may consider the probe diameter of 8 mm relatively small for a cooled probe.

The Viper turbine rotor is a very high solidity design having 113 blades with a blade pitch of 12.54 mm. Although the probe was placed approximately 3 axial chords downstream of the rotor trailing edge, the effects of the introduced blockage must be taken into account. This is accomplished using the relation by Wyler [75], given in eq. (6.32) for cylindrical probes inserted sidewards halfway into an axisymmetric jet.

$$\frac{\delta M}{M} = \frac{1}{\pi}\left[\frac{1+\frac{\gamma-1}{2}M^2}{1-M}\right][1.15+0.75(M-0.2)]\left(\frac{D}{W_{bp}}\right) \tag{6.32}$$

The resulting corrected unsteady Mach number distribution is presented in Figure 6.24. The average corrected Mach number is now around 0.61, rather than 0.68, which matches with an expected approximate value of 0.6, but underlines once more the difficulty of obtaining available comparison data for validation at those temperature levels.

6.2.4.3 Uncertainty

The uncertainty for the virtual 3-hole mode has been calculated by the propagation method described in section 6.1.3 for each of the derived terms. The yaw angle uncertainty in the virtual 3-hole mode is calculated as 0.59°, whereas the aerodynamic calibration uncertainty on the total pressure corrected for incidence is found to be 3.37 mbar. The uncertainties for static pressure and Mach number are calculated as 7.00 mbar and 0.005 respectively.

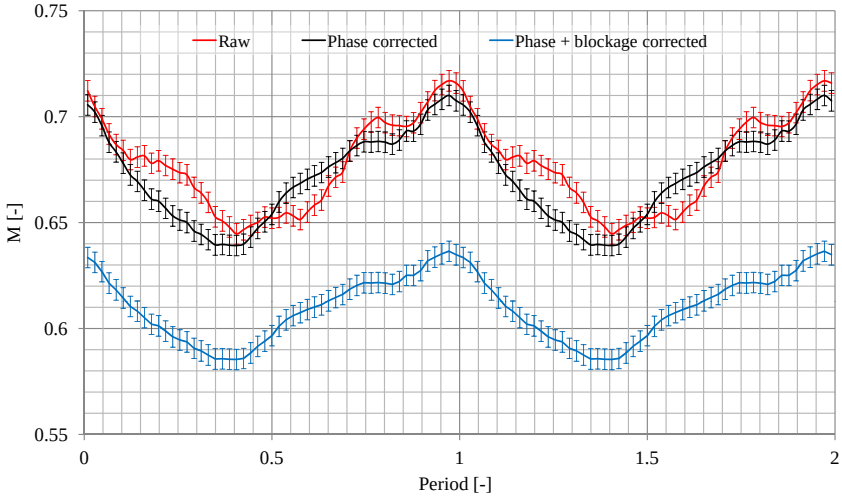

Figure 6.24: Mach number distribution with added blockage effect correction at 10000 RPM, immersion = 23 mm from hub, $T_{gas} = 503°C$

6.3 Combustion Rig Measurements

The second testing opportunity for the probe and cooling system in an industrial environment was again provided by Rolls-Royce within the EU FP-6 HEATTOP project. A two-days testing slot was made available on the intermediate pressure combustion rig shown in Figure 6.25.

6.3.1 Experimental Set-Up

The intermediate pressure combustion rig (a.k.a. IP rig) is designed and built for testing of single or twin burners at pressures up to 7 bar. The IP rig is composed of a central flame tube which is either metallic or quartz and has optical access through a side quartz window as shown in Figures 6.26 and 6.27.

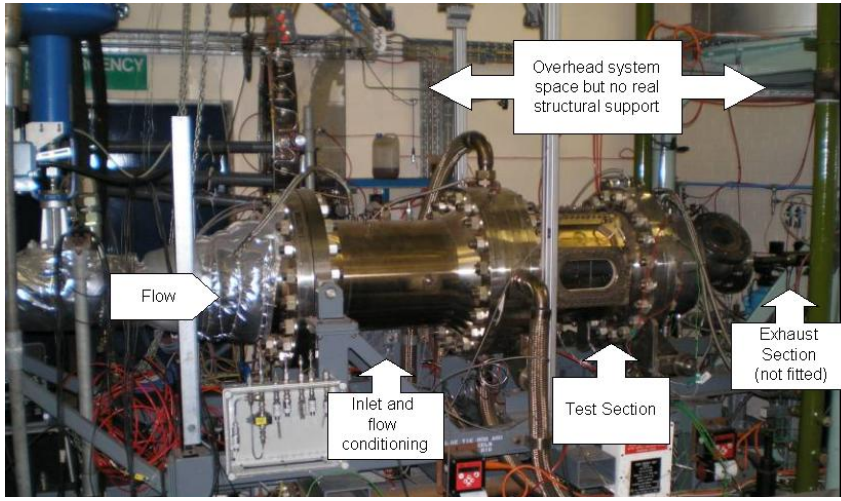

Figure 6.25: Rolls-Royce IP Combustion Rig at Derby, UK

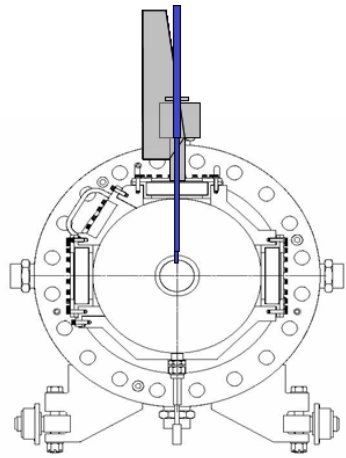

Figure 6.26: Rolls-Royce IP Combustion Rig, cross-sectional view and probe traversing arrangement

The co-centered arrangement of the rig creates a passage for the secondary air flow around the central flame tube used for cooling. The tem-

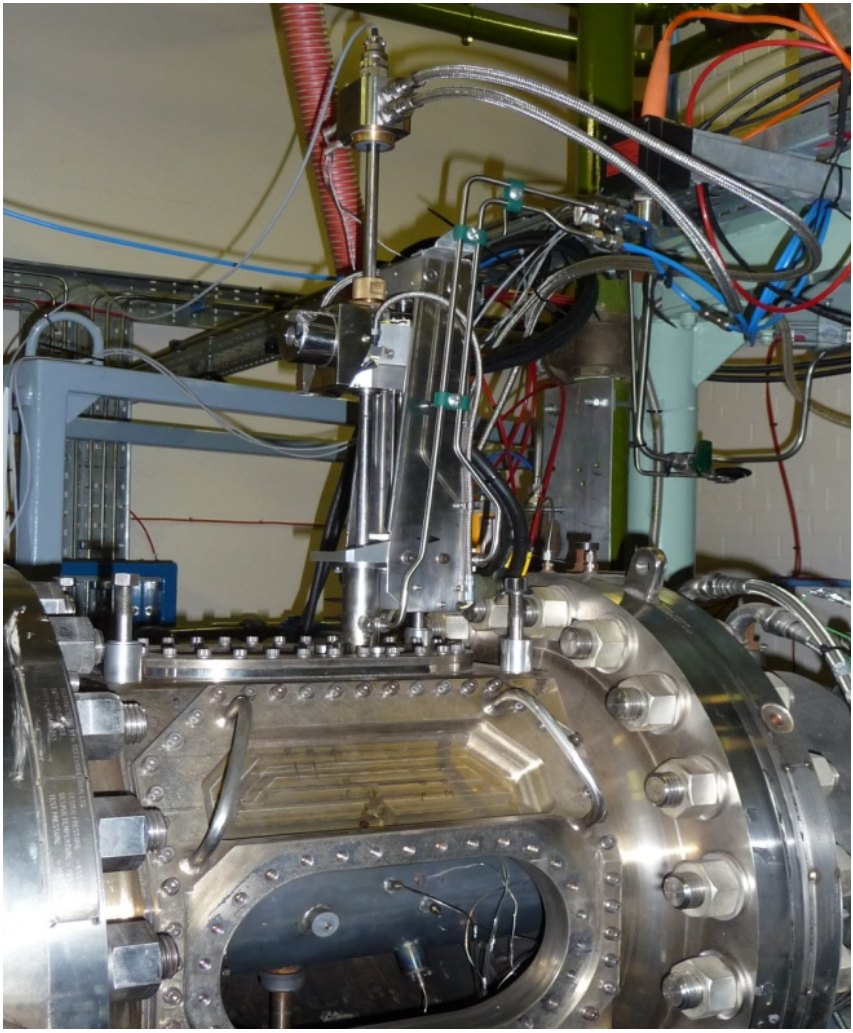

Figure 6.27: Rolls-Royce IP Combustion Rig, optical access window, probe and traverse gear mounted

perature of the cooling air is of the order of 20°C. During the test campaign, the flame tube was instrumented with thermocouples and with a wall-mounted high temperature piezoelectric static pressure transducer

and a pneumatic pressure tap to monitor the burner can pressure and temperature.

The tests were conducted on a twin burner running on kerosene at various air-fuel ratios up to the maximum allowable burner can wall temperature of approximately 1000°C. The test conditions are given in Table 6.3. The rig was operated at pressure levels below 2.4 bar in order not to exceed both the static calibration range of the probe and the rated pressure range of the probe sensor used, which is 25 psi (∼1.72 bar) absolute. The flame temperature can not be measured due to the impossibility of using optical techniques when a metal burner can is used, and is therefore calculated for flame-core and mixed out conditions by Rolls-Royce engineers using an in-house code for which the details have not been disclosed. The most severe conditions with highest temperature obtained is 1658°C bulk temperature.

In Figure 6.28 the flame tube is shown at test point 10, where the maximum allowable burner can temperature is reached.

Table 6.3: Rolls-Royce IP Combustion Rig, summary of test conditions

Point	T_{can} [°C]	$P_{s_{can}}$ [bar†]	T_{bulk} [°C]	$T_{exhaust}$ [°C]
1	337	1.42	648	544
2	472	1.66	868	637
3	550	1.68	953	658
4	583	1.69	1018	689
5	640	1.66	1176	751
6	580	1.69	916	645
7	882	1.82	1521	840
8	922	1.8	1585	862
9	951	1.84	1658	886
10	984	2.28	1556	912

† Gauge Pressure

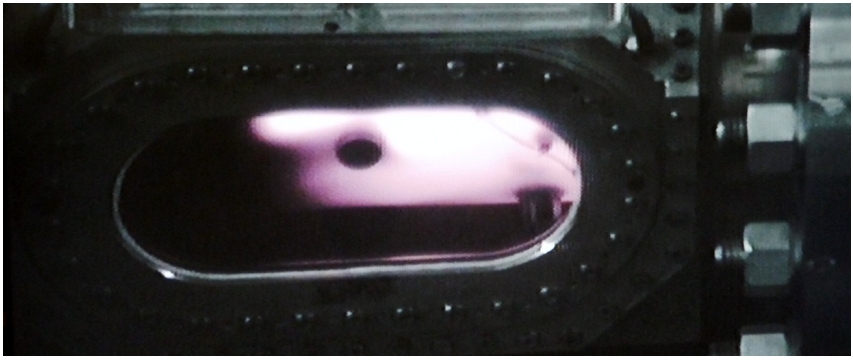

Figure 6.28: Rolls-Royce IP Combustion Rig, flame tube shown at maximum allowable temperature ($T_{wall} = 984°C$, $T_{bulk} = 1556°C$)

6.3.2 Results

The probe was traversed through the secondary air flow down inside the central flame tube as shown in Figure 6.26. During burner start-up the probe was retracted from the flame tube, staying in the secondary air flow jacket shown in Figure 6.29.

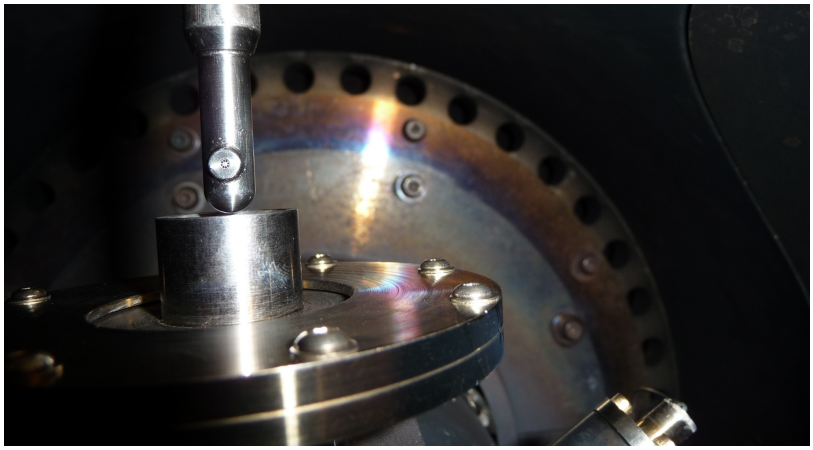

Figure 6.29: Rolls-Royce IP Combustion Rig, probe retracted in the secondary air flow channel, before tests

The data were sampled at 1 MHz on a high speed data acquisition system for measurements at a fixed location in the flame tube or at 2 kHz during continuous traverses into the flame tube over slightly more than 120 seconds. The acquisition system was set-up in the test cell inside a Faraday cage and a UPS power supply was used with an isolation transformer against electrical noise or spikes from the power grid.

An example of signal recorded during a continuous traverse down to the center of the flame tube is shown in Figure 6.30. The continuous line indicates the can pressure measured by the pneumatic pressure transducer. Under those conditions ($T_{bulk} = 1521$°C, $P_{can} = 1.82$ bar gauge), and with a cooling rate of approximately 10 ℓ/min at 32 bar water pressure, the sensor diaphragm temperature has reached 210°C. The probe survived all tests, up to these extremely harsh conditions.

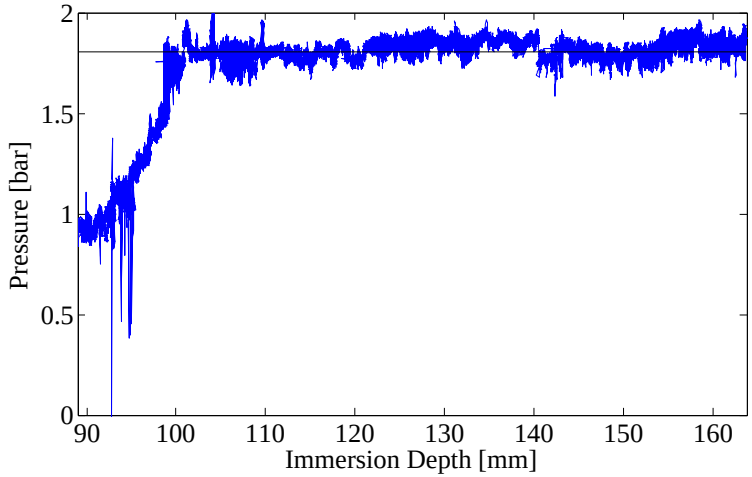

Figure 6.30: Rolls-Royce IP combustion rig, total pressure measured along a continuous probe traverse down to the center of the flame tube. $T_{bulk} = 1521$°C, $P_{can} = 1.82$ bar gauge

An example of raw pressure signal showing fluctuations under rumble conditions is shown in Figure 6.31. Again, the continuous line indicates the can pressure as measured by the pneumatic pressure transducer. Under the same probe cooling settings, the measured sensor diaphragm

temperature was 178°C, for a flame temperature of $T_{bulk} = 1556$°C for a different air-to-fuel ratio and hence a different temperature distribution.

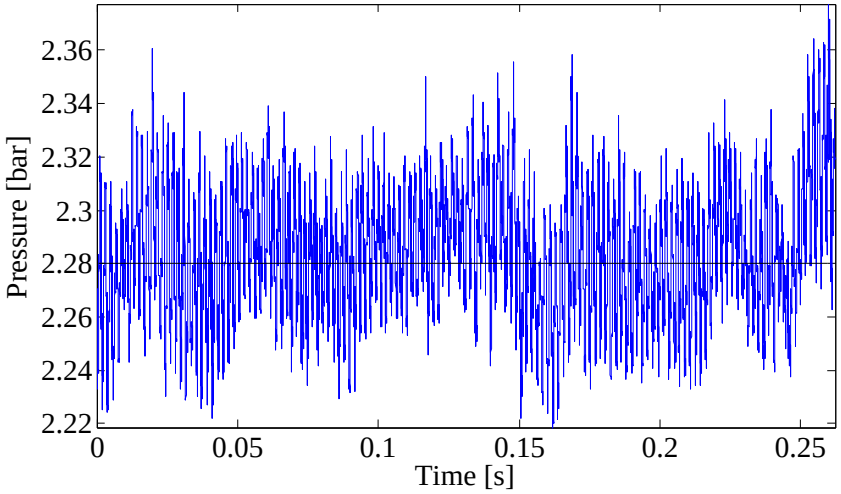

Figure 6.31: Rolls-Royce IP combustion rig, time series of fluctuating pressure at rumble conditions. $T_{bulk} = 1556$°C, $P_{can} = 2.28$ bar gauge

Regarding frequency analysis, the power spectrum of a recording at the center of the flame tube is shown in Figure 6.32 during rumble (i.e. low frequency flame instability) conditions. Contrary to the measurements behind the turbine rotor of the Viper engine, the sensor natural resonance frequency is barely visible, practically not excited due to the low frequency instabilities. The screen cavity resonance is also barely visible for the same reasons. No significant frequency content can be found beyond 40 kHz and most of the frequencies of interest are to be found in the range of a few kHz, representing flame instability frequencies, as shown in Figure 6.33. Unfortunately the exact value of the combustor natural frequency, f, can not be given as it is considered 'commercially sensitive' by Rolls-Royce. However, the probe has been successful in resolving the natural frequency as well as two harmonics.

Figure 6.34 shows a view of the probe after the IP rig test campaign.

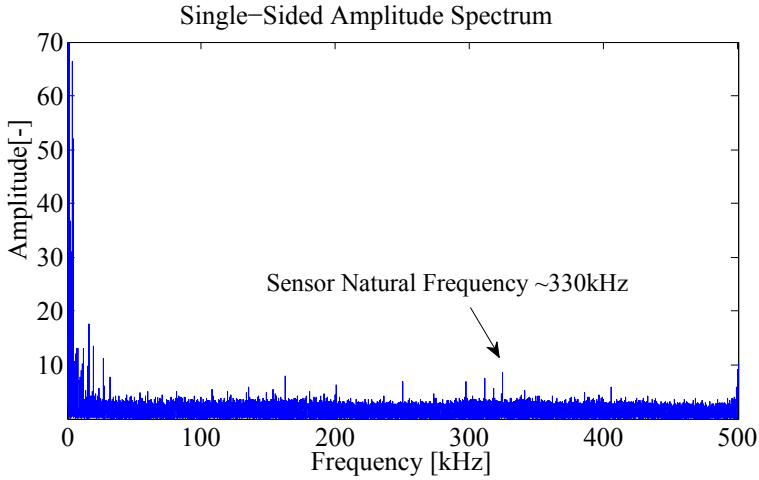

Figure 6.32: Rolls-Royce IP combustion rig, full power spectrumat rumble conditions. $T_{bulk} = 1556°C$, $P_{can} = 2.28$ bar gauge

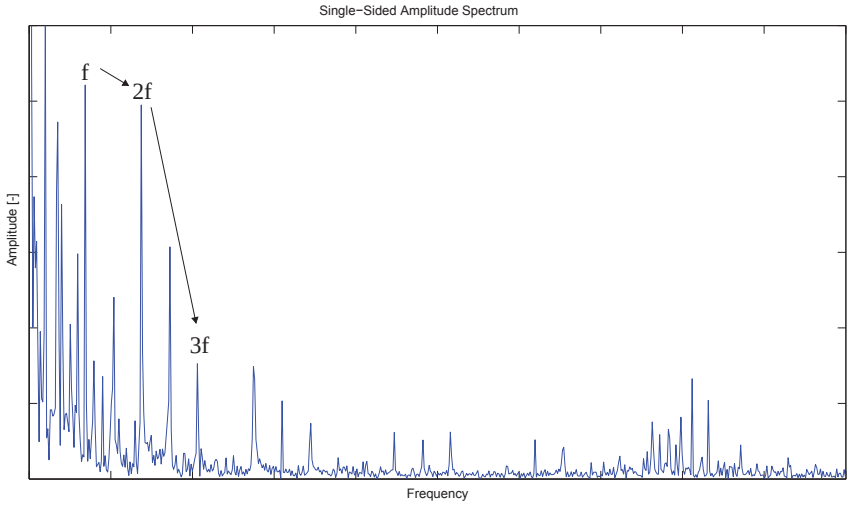

Figure 6.33: Rolls-Royce IP combustion rig, low frequency content at rumble conditions. $T_{bulk} = 1556°C$, $P_{can} = 2.28$ bar gauge

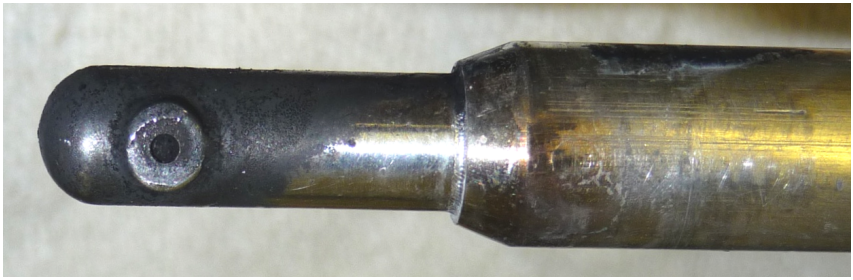

Figure 6.34: First prototype of the VKI fast response cooled total pressure probe after testing in the RR IP combustion rig

6.4 Summary

Summarizing the prototype testing phase of the work, the probe designed and manufactures successfully survived the harsh environment found at the exit of the Rolls-Royce Viper single-spool turbojet engine as well as the Rolls-Royce Intermediate Pressure Combustion Rig. Moreover, the steady signal has been found to be in agreement with reference instrumentation in the Rolls-Royce IP Rig.

During the first test campaign very low signal-to-noise ratios were obtained underlining the importance of isolation and shielding against electromagnetic interferences. Following the employment of a Faraday cage enclosing all the data acquisition and signal conditioning hardware and an isolation transformer combined with an on-line UPS system which first filters the grid electricity through a set of batteries and then reconstructs a stable power source, significant improvements were obtained, allowing successful test data.

The probe has been calibrated aerodynamically allowing the use of a virtual 3-hole mode. However, due to the lack of a proper trigger signal required for phase-locked averaging, data obtained is limited.

In total the probe survived three test campaigns, including the extremely harsh conditions shown in Figure 6.28, surpassing expected design life of a single test campaign.

Chapter 7

Second Generation Probes

Following the testing of the first prototype probe manufactured, a new generation of the cooled probe has been designed. In the second generation, the electrical splicing layout has been altered, hermetically sealing the sensor wires from the coolant.

Another change for the second prototype is the use of a leadless sensor, where the sensor chip is brazed to the lead wires instead of a wire bonding process. The leadless sensor chip is shown together with a wire-bonded sensor in Figure 7.1. Four probes of the second generation, two having a 50 psi (∼3.44 bar) absolute pressure range and two having a 200 psi (∼13.8 bar) absolute pressure range, have been manufactured as shown in Figure 7.2.

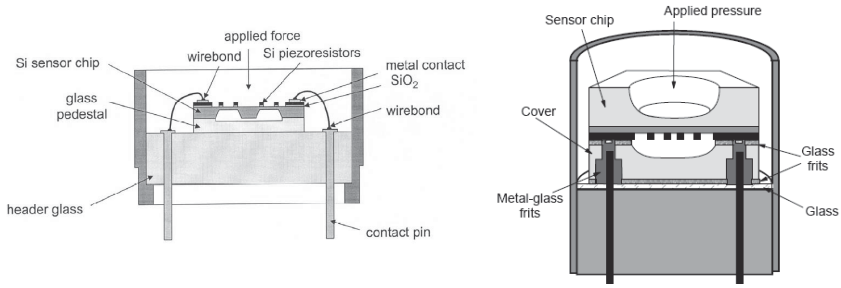

Figure 7.1: Absolute wire-bonded sensor (left), and absolute leadless sensor (right) [38]

In this configuration, unlike a conventional ultra-miniature pressure transducer, the sensor chip is flipped in order to create a direct contact

Figure 7.2: First prototype probe (left) v.s. four probes of the second generation (right)

between the contact pins and the sensor bond pads. The sensor chip is baked under vacuum, sealing the reference pressure cavity and creating the electrical contacts between the header and the chip itself thanks to a conductive resin. The absence of the fragile gold wires and the complete isolation of the piezo-resistive elements ensure added durability

and robustness. On the other hand, considerable improvements in the signal-to-noise ratio are achieved by avoiding exposure of the lead wires to the flow.

Conventional sensors are frequently coated with a room temperature vulcanizing silicone rubber (RTV) in order to protect the piezo-resistive elements and transmission lines from foreign object damages (FOD), decreasing the natural frequency of the sensor. As these elements on a leadless sensor are practically immune to foreign object damages, an RTV coating is avoided.

Another difference in the leadless sensor layout is the presence of a cavity facing the flow, which may act favorably in terms of aerodynamic characteristics, creating a flatter response around zero incidence and hence increasing angular insensitivity. A variable thickness distribution between the measurand and the piezo-resistive elements should not pose a problem in terms of thermal gradient across the membrane at the back end when the sensor is utilized in uncooled applications in a steady temperature environment. However, adverse effects are observed for cooled applications, as will be discussed later in this thesis.

For the second generation probes, Kulite XCEL-072 series leadless ultra-miniature pressure transducers are selected. These transducers, which were the smallest existing leadless transducers at the time, are slightly larger in diameter compared to the XCE-062 series used in the first prototype probe. The increase in diameter from 0.062" ($\sim$ 1.6 mm) to 0.072" ($\sim$ 1.8 mm) necessitated a slight enlargement of the sensor head piece.

Additionally, the connection box located on the stem of the probe has been redesigned. The hermetic sealing of the wires removed the necessity to use a pressure sealing signal lead socket, allowing the use of gold-plated plugs offering much higher signal-to-noise ratios. The decreased the mass at the end of the probe due to a more compact connection box thanks to a much smaller socket is also favorable for the mechanical vibration characteristics of the probe.

In this design, shown in Figure 7.3, the PT100 RTD temperature sensors are moved from the probe stem to the cooling system. Modifying the coolant feed and return line connections, the capability to install the sec-

Figure 7.3: Head (top), connection box (bottom) of the second generation probe

ond generation probes into gas turbines offering much tighter accesses, essential for stationary gas-turbine testing, is achieved.

Although a batch of four probes of the second generation have been manufactured, only one probe, with a pressure range of 50 psi (∼3.45 bar) has been tested in an industrial test environment.

Once again, before presenting test results, the calibration procedure is explained in detail.

7.1 Signal Conditioning and Calibration

In order to record the average sensor temperature, no temperature compensation module is used as explained before in section 4.1. Unlike the signal conditioning unit used for the prototype probe, shown in Figure 4.2, a new amplifier circuitry, shown schematically in Figure 7.4, is employed for the second generation probes. In this new amplifier topology, a sense resistor is again added to the Wheatstone bridge in series but with the difference of being much smaller in resistance compared to the equivalent bridge resistance (10Ω v.s. 1.6kΩ) to avoid altering the bridge supply voltage with increasing temperature. A mirror system composed of an equivalent bridge resistance at room temperature, 1.6kΩ, and another sense resistor of the same value is implemented in order to track the change in bridge resistance with temperature. An amplifier is placed at the bridge to get a signal proportional to pressure, named V_p, and another with a higher gain of 1000 is placed across the sense resistors, yielding a signal, V_{sense}, proportional to the temperature of the sensor. This arrangement, like the one used before, allows a real-time monitoring of the sensor temperature in operation.

7.1.1 Static Calibration

The probe is calibrated in an oil bath using a special enclosure built for calibrating such probes which incorporates two sheathed thermocouples. The probe has been calibrated between -500 and 4500 mbar gauge pressure and between 20 °C and 180 °C with 100 calibration points.

Without the use of a temperature compensation module, the slope of the calibration together with the offset changes considerably as a function of temperature, and this fact necessitates the calibration of the probe in both temperature and pressure. The resulting calibration surfaces, one for temperature and one for pressure are given in Figure 7.5.

Using a 16-bit transient recorder for a range of 4.5 bar, and with a span of ±5 V DC for the pressure signal and a span of ±10 V DC for the temperature signal, the static calibration uncertainty on the pressure signal is found to be 1.58 mbar for 95% confidence. The combined uncertainty

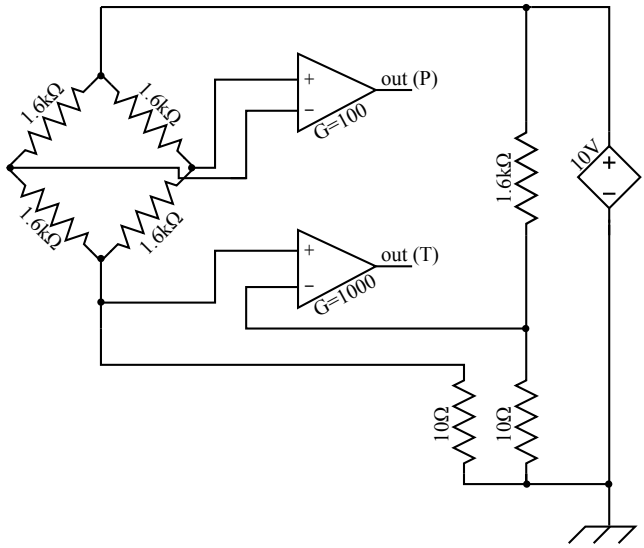

Figure 7.4: Amplifier circuit diagram showing pressure and temperature outputs

values of the two thermocouple used for temperature calibration are found to be 0.143°C. The corresponding sensor temperature calibration uncertainty is 0.16°Cfor 95% confidence.

One problem that is faced in this procedure is the temperature limitations both by calibration tools and probe assembly. The advantage of using a cooled probe is to be able to employ sensors and other materials beyond their normal operating margins. In the second generation design, the probe is limited to 200°C without cooling imposed by certain sealants used.

While the sensor membrane is capable of withstanding temperatures at the order of 500°C, the sensor electrical cables are limited to much lower temperatures (i.e. 275°C). Therefore, the limiting factor on the static calibration envelope is determined by the sealants used for hermetic sealing of the sensor lead wires.

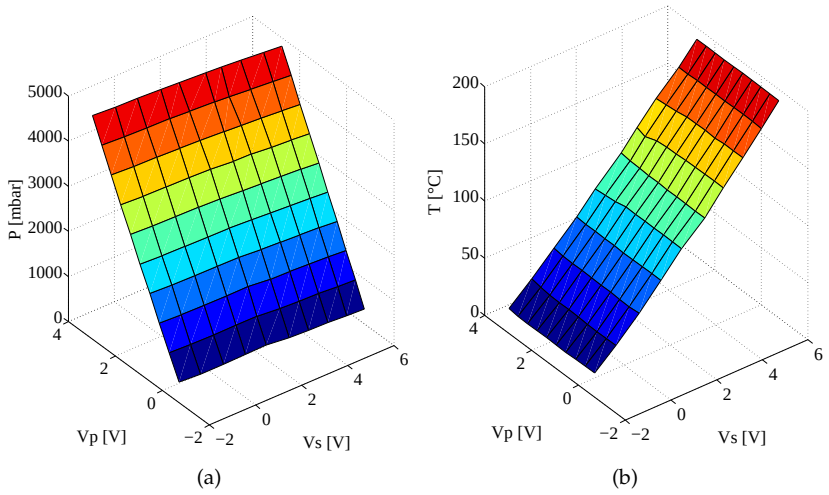

Figure 7.5: Static calibration pressure and temperature maps

7.1.2 Dynamic Calibration

The probe has been tested in the VKI shock-tube facility in order to determine the transfer function and the resonance frequency of the line cavity system formed by the screen in front of the sensor. The resulting power spectrum density plot is given in Figure 7.6, where the resonance frequency of the line-cavity system is found to be around 35 kHz at room temperature. The peaks seen on the lower end of the frequency spectrum (i.e. <20kHz) in Figure 7.6 are due to mechanical vibrations related to poor vibrational insulation of the probe from the shock tube. In order top improve the quality of the shock tube test results, the probe mounting scheme needs to be modified in the future.

7.1.3 Aerodynamic Calibration

The probe has been calibrated using the VKI C-4 free jet calibration facility at five different Mach numbers ranging from 0.3 to 0.7 for yaw angles ranging from -70° to 70° as shown in Figure 7.7. The pressure

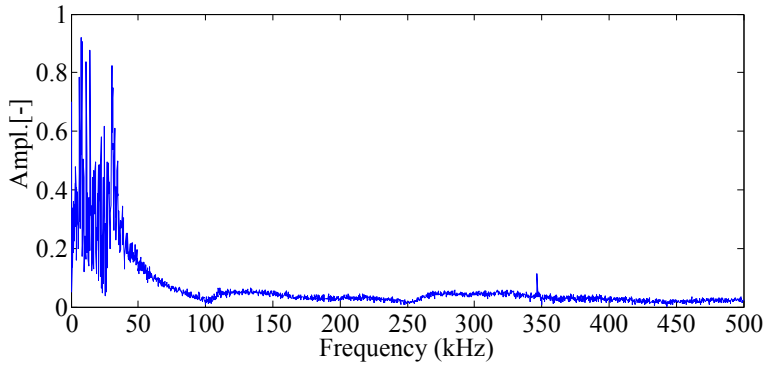

Figure 7.6: Shock tube test power spectrum density plot

recovery ratio is given before in eq. (6.13). This allows to correct for the total pressure values measured when the flow angle is known.

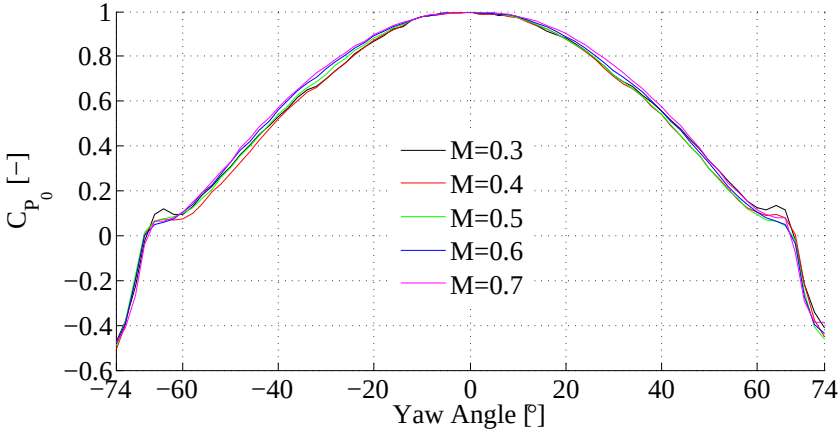

Figure 7.7: Pressure recovery ratio (C_{p_o}) curves for different Mach numbers

However the use of C_{p_o} term requires the knowledge of static pressure as explained before in section 6.1.3. Therefore, the alternate pressure recovery definition, given before in eq. (6.19), is used for tests where the static pressure is unknown and is plotted in Figure 7.8 for several Mach

numbers.

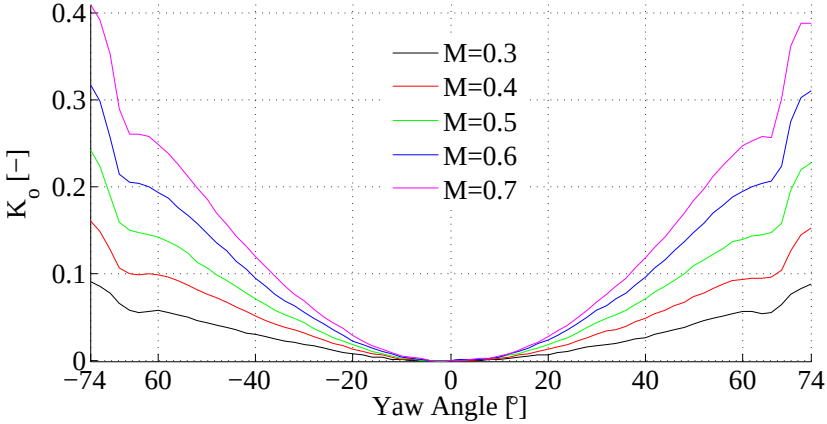

Figure 7.8: Pressure recovery ratio (K_{p_o}) curves for different Mach numbers

The uncertainty is calculated for the pressure recovery ratios are given in Table 7.1.

Table 7.1: Calculated uncertainty values for pressure recovery ratio for 95% confidence

M	0.3	0.4	0.5	0.6	0.7
δC_{p_o}	0.0062	0.0057	0.0052	0.0048	0.0043
δK_{p_o}	0.0032	0.0032	0.0032	0.0031	0.0031

7.2 Testing

7.2.1 Experimental Setup

The probe has been tested on a Volvo Aero RM 12 military engine. The engine, the test cell and the support personnel have been provided by Volvo Aero within the HEATTOP Project. The RM 12, a low-bypass ratio, two-spool after-burning military turbofan, is a derivative of the General Electric F404, originally developed for the F/A-18 Hornet fighter.

The RM 12 has an increased performance, greater resistance to bird strikes and improved reliability for single engine certification thanks to a new compressor and an afterburner designed and produced in Trollhättan, Sweden. It is equipped with a full authority digital engine control (FADEC) system with a maximum rated thrust of 54 kN in dry conditions and 80.5 kN in wet conditions, powering the Saab JAS 39 Gripen (Griffin) fighter and is in service since 1987. The engine has a frontal area of 0.72 m^2, weighs 1050 kgs with a maximum air flow of 67.9 kg/s while the low pressure shaft speed is limited to 13050 rpm.

A special permit issued by General Electric to Volvo Aero as licensee of the F404 engine was required for measurements in this engine, which brought its own set of limitations. For this reason, certain properties and specifications of the test vehicle have not been disclosed.

The probe is installed via a remote controlled traverse gear at one of the four instrument rake ports, downstream the low pressure turbine and ahead of the afterburner flame holders, passing through the bypass duct and the liners. Reference Pitot and thermocouple rakes were also installed on other available ports which were at the same axial location, equally placed along the periphery. In Figure 7.9, the RM 12 engine test cell is shown while the engine is running with the afterburner lit, where in Figure 7.10, a cutaway of the engine is shown.

The engine has been run at several conditions ranging from idle to full wet thrust of 80 kN, with turbine exhaust temperature (TT56) values reaching 900°C. In this thesis, results obtained at full dry thrust of $\sim$50 kN and N1$\sim$12500 RPM are presented, where the gas temperature TT56 is $\sim$800°C.

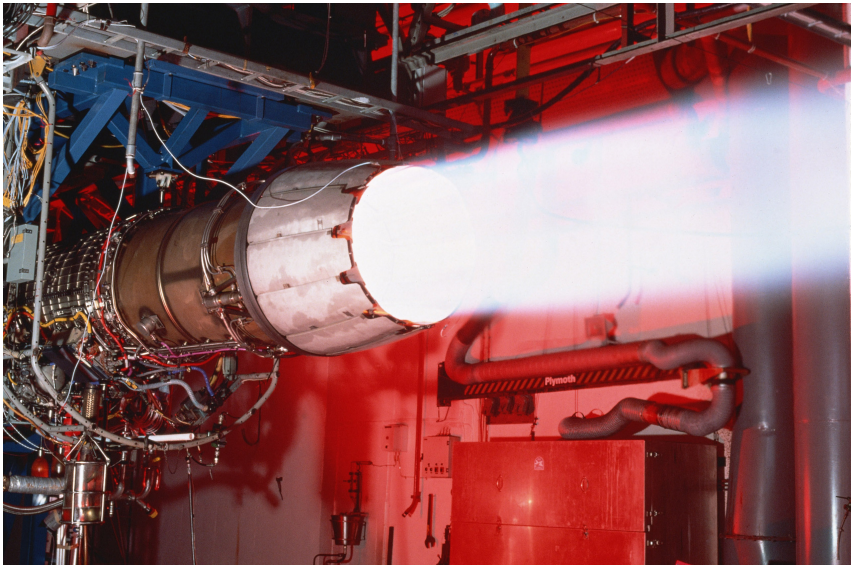

Figure 7.9: Volvo RM 12 in the test cell with the afterburner lit

7.2.2 Raw Signal and Signal-to-Noise Ratio

An example of raw signal is shown in Figure 7.11 plotted here over 4 blade passages.

The simplest information to be extracted from the signal is of course the time averaged pressure level presented in Figure 7.13 as well as the corresponding pressure fluctuations. These are presented in terms of RMS values in Figure 7.12 along the radial traverse, for full dry thrust (S4) and full wet thrust (S5), showing fluctuations as high as $\pm$180 mbar in the tip region.

It has to be noted that the quality of the signal is excellent. The RMS value of the noise is taken from recordings prior to the engine startup, while the cooling system and traverse gear were running. After amplification, the background electronic noise on the sensor was found to remain around $\pm$2.477 mbar RMS without the engine running.

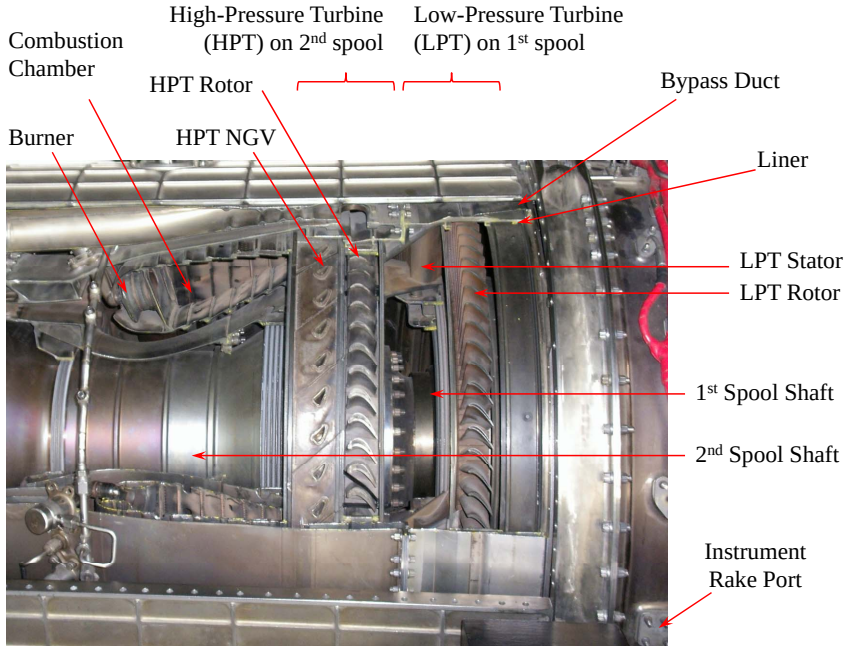

Figure 7.10: Volvo RM 12 cutaway located at the entrance hall of Volvo Aero site Trollhättan, Sweden

The signal-to-noise ratio, SN, was defined before in eq. (6.27). The results of the calculation of the signal-to-noise ratio according to eq. (6.27) when the engine was running yield 77.70 for midspan conditions at 12500 RPM, which is superior to the first prototype, which has a signal-to-noise ratio of 14.32 in a similar environment. This is to be attributed to the extreme care which was taken in shielding cables and electronics (by the use of a Faraday cage to install the electronics and data acquisition system) in the test cell. The additional use of an on-line uninterruptible power supply (UPS) together with an isolation transformer greatly reduced the noise levels as well.

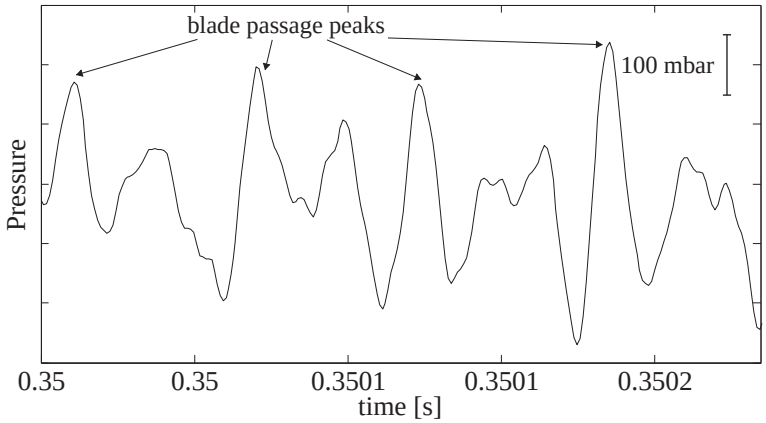

Figure 7.11: Example of raw pressure signal at 12500 RPM, hub distance = 49.9 mm

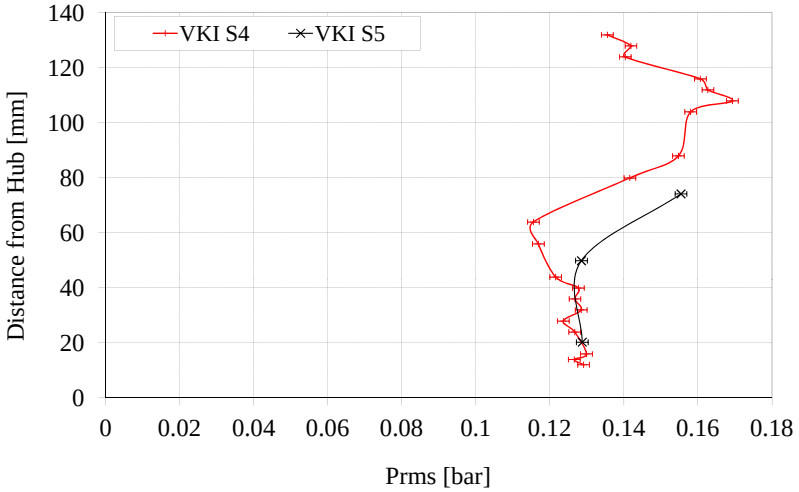

Figure 7.12: Pressure fluctuations at full dry thrust (S4) and full wet thrust (S5)

7.2.3 Time-Averaged Measurement Results

The probe was traversed radially over the blade height at two different operating conditions. The S4 condition corresponds to full dry thrust without the afterburner lit while S5 corresponds to full wet thrust with the afterburner lit. The resulting mean pressure distribution is plotted with respect to the Volvo reference Pitot rake measurements in Figure 7.13.

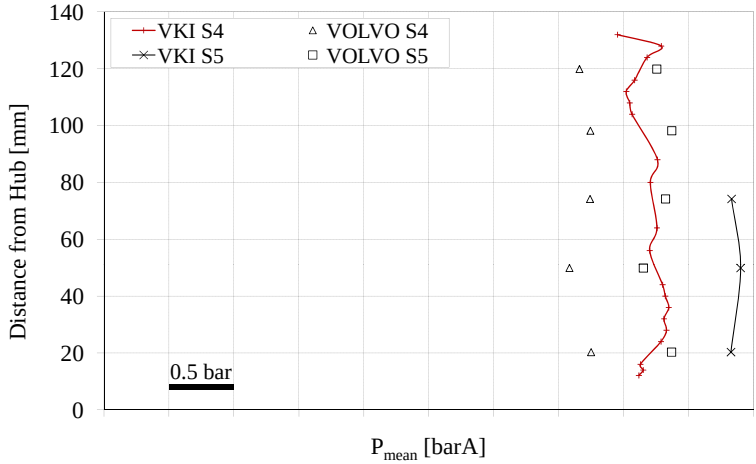

Figure 7.13: Mean Pressure Distribution

As mentioned before, the second prototype batch has been manufactured using sensors of two pressure ranges (50 psi ∼3.45 bar and 200 psi ∼13.8 bar absolute). The mean pressure level at the turbine exit of the test vehicle being around 3.5 bar (∼65.27 psi), one of the 50 psi (∼3.45 bar) probes was used for testing, resulting in a decreased sensitivity corresponding approximately to one fourth of the sensor range.

Once again, these measurement results underline the need for an appropriate sensor pressure range whenever possible, or better, using a differential pressure sensor. Unfortunately, none of those options were possible in the present case.

A pressure over read of approximately 0.5 bar with respect to the rake

pressures is observed after conversion by the appropriate calibration data. The reasons behind this measurement bias need further examination. As a first insight, a possible influence of temperature non-uniformity of the sensor membrane introducing an additional bridge unbalance is suspected.

In an effort to justify this hypothesis, The change in bridge resistance with respect to temperature has been measured using the static calibration setup and a precision ohm-meter. The resulting curve is presented in Figure 7.14. As it may be seen in the figure, the bridge resistance has been measured from both ends, namely the supply end (Brown-White) and the signal end (Green-Yellow). It is a known fact that when a Wheatstone bridge is composed of four equal resistances, the equivalent bridge resistance equals the value of an individual resistor. Hence, it is not surprising to obtain two nearly overlapping linear fit curves for both ends of the bridge. The slight imperfection is justified with the manufacturing imperfections of the individual resistances which is quoted as a 'residual unbalance' of 5 mV.

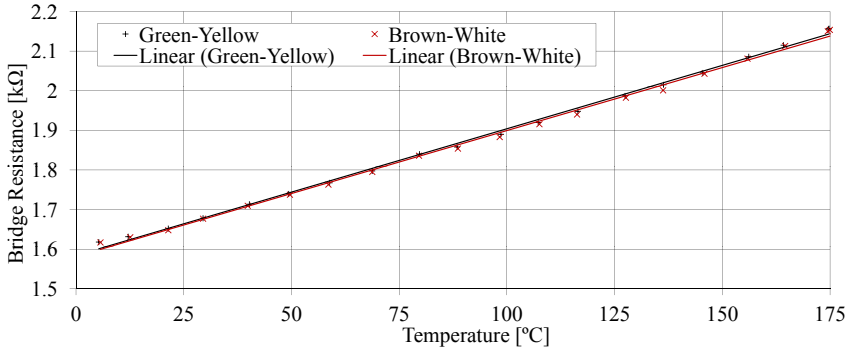

Figure 7.14: Bridge resistance calibration

Given that the sensor has a full scale output of 100 mV when supplied with 10 V and has a range of 3.45 bar, the imbalance required for 0.5 bar over-read is calculated as:

$$\left(\frac{0.5bar}{3.45bar}\right) 100mV = 14.5mV \tag{7.1}$$

According to Kirchhoff's circuit laws, for a bridge supplied with 10 V, the current passing through each side of the circuit is calculated as 3.125 mA. In order to create an imbalance of 14.5 mV, the required resistance imbalance is then calculated as:

$$\frac{14.5mV}{3.125mA} = 4.63\Omega \tag{7.2}$$

which corresponds to less than 1 per cent (0.073%) of the individual resistance value.

According to the curves shown in Figure 7.14, the resistance slope is calculated as $3.2\Omega/^{\circ}C$, which yields a temperature gradient as low as 1.456°Cunderlining the sensitivity of the sensor used to temperature gradients.

A new design of the electronic circuit allowing to track the individual resistance changes related both to pressure and temperature is developed, however could not be tested under a thermal gradient during the course of this study as calibration of such a system requires a laboratory setup capable of inducing controlled temperature gradients across the sensor membrane.

At full dry thrust condition, the turbine exit temperature varies between 740 and 840°C, where at full wet condition the temperature ranges between 800 and 905°C along the blade height. The amount of heat extracted and membrane temperature are shown in Figure 7.15. While the mean sensor membrane temperature did not exceed 175°C, the heat power extracted from the probe at a cooling rate of 4 ℓ/min exceeded 7 kW. The coolant feed and return temperature difference was found to be below 27°C at the most severe conditions.

It is worth mentioning that the sensor cooling is proven to be effective since the system is able to keep the sensor temperature below 200°C while the gas temperature is around 900°C.

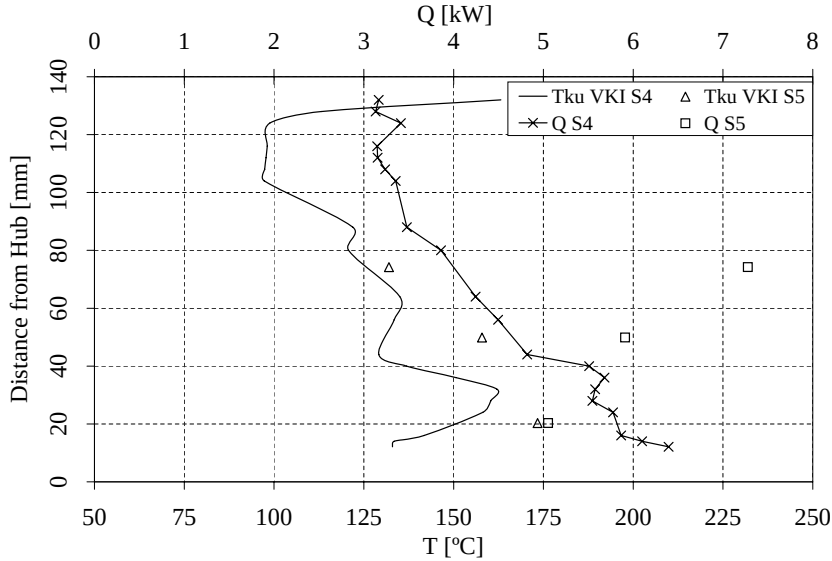

Figure 7.15: Average sensor membrane temperature and probe cooling heat power extracted

7.2.4 Unsteady Measurement Results

The high frequency signals are acquired using a 16-bit transient recorder at 1 MHz. At full dry thrust conditions, the blade passing frequency is found to be 17.046 kHz, which corresponds to a resolution of 59 points per blade passage. With these settings and having a rotor with 82 blades, more than 8700 blade passages, corresponding to more than 106 full rotor revolutions are recorded during the acquisition time of $\sim$0.5 s.

7.2.5 Frequency Analysis

The signals were first analyzed in the frequency domain. In Figure 7.16 the FFT of a recording at 12500 RPM is given. The fundamental blade passing frequency is 17.05 kHz, and 5 harmonics, (1) to (5), are clearly seen. The resonance around 137 kHz, (6), is the line-cavity resonance frequency at the flow temperature.

It shall be noted that this frequency, found to be around 35 kHz at room temperature, is increasing with cavity gas temperature just as presented earlier in Figure 6.13 following the relation given by Helmholtz presented earlier in eq. (4.1), for the prototype probe tested on Viper test engine.

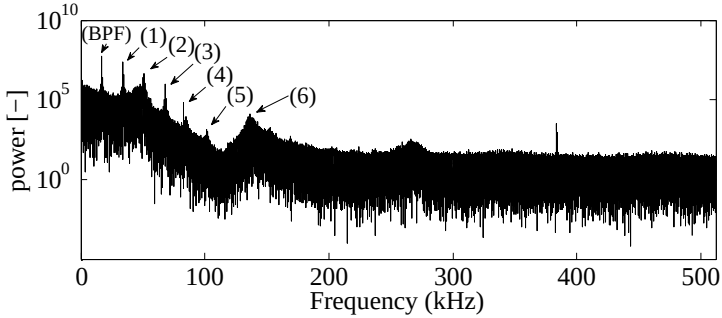

Figure 7.16: Fast-Fourier transform plot of the pressure signal at S4 (12500 RPM), hub distance = 49.9 mm

7.2.6 Phase Locked Averaging

The signals recorded are phase-locked averaged in order to retrieve the periodic pressure fluctuations. The tip timing sensor monitoring the first fan rotor having 42 blades on the same spool is fed into an electronic box suppressing all blades but the first one, yielding a once-per-revolution signal, which is used to trigger the acquisitions. The full blade tip timing signal and the trigger signal are both recorded, where the once-per-revolution signal is used for taking the rotational speed changes during acquisitions into account for phase-locked averaging.

The RPM values are calculated during an acquisition time using the once-per revolution signal. The mean RPM values together with related standard deviations during each acquisition at full dry thrust conditions (S4) along the blade height are plotted in Figure 7.17.

In Figure 7.18 the AC component of the raw signal over 2 blade passages for the first 10 revolutions are plotted. In addition the phase-locked aver-

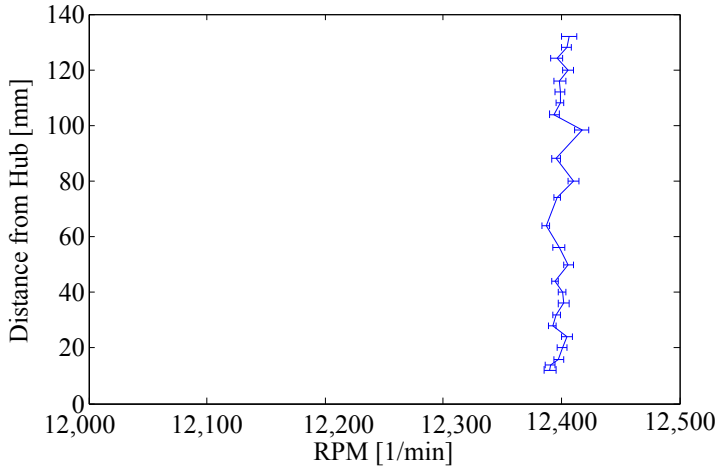

Figure 7.17: RPM, and standard deviation of the RPM during an acquisition along the radial traverse at S4

age (i.e. averaging with respect to a blade passage), standard deviation of the PLA around itself, the ensemble average (i.e. averaging with respect to a full revolution) and the standard deviation of the ensemble average around itself are plotted for the signal acquired at the midspan at S4.

The agreement between the phase-locked average (PLA), which is an average of all the blade passages over the rotor disc copied once to indicate two blade passages, and the ensemble average (EA), which is an average over one full revolution, showing only the first two blade passages is noteworthy. Moreover, the standard deviations from these two averages are also in agreement.

When the raw signals plotted in Figure 7.18 are combined together, the plot shown in Figure 7.19 is obtained, where an oscillating behavior of the signal peak location is visible. In order to better demonstrate this behavior, a vertical line is drawn around a peak of the ensemble average, where the oscillations around the peak value are at the order of 20% of a blade pitch, corresponding to flow outlet angle variations at the order of 0.88° given the blade pitch is 4.39°.

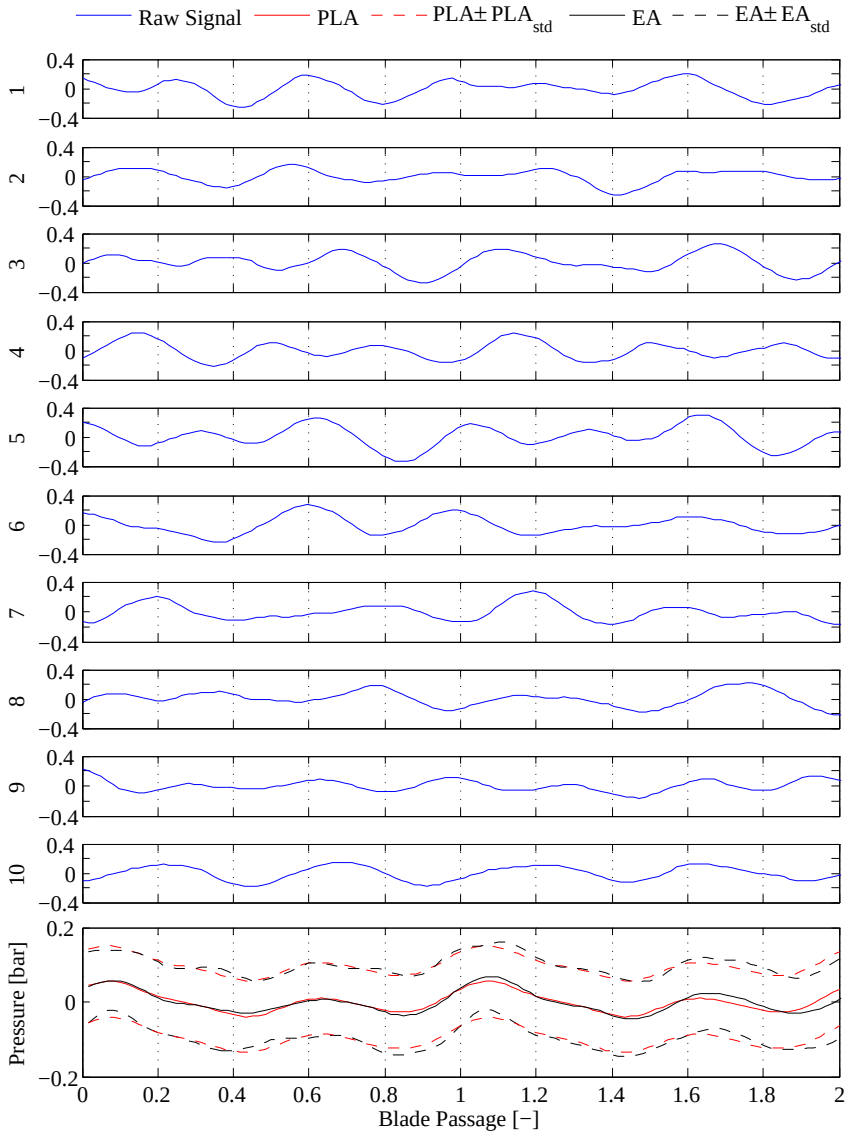

Figure 7.18: Raw signal for the first 10 revolutions, phase locked average, standard deviation of the PLA, ensemble average and standard deviation of the ensemble average over the first two blade passages at S4, hub distance= 74.2 mm

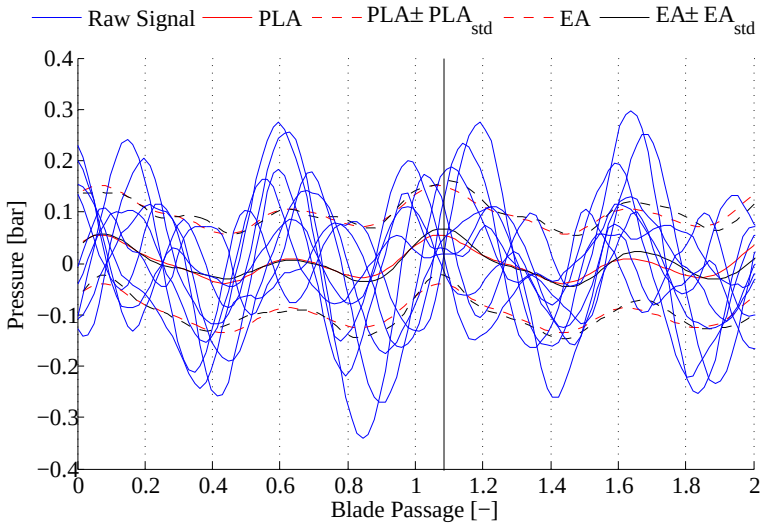

Figure 7.19: Raw signals combined for the first 10 revolutions, phase locked average, standard deviation of the PLA, ensemble average and standard deviation of the ensemble average over the first two blade passages at S4, hub distance= 74.2 mm

This effect, which seems to be mainly on the outlet flow angle may be explained by several aerodynamic reasons among which unstable shock-boundary layer interactions and the influence of wakes from upstream may be listed. More importantly, assuming a high acceleration in the stator passage upstream, where the flow starts in laminar regime over the rotor passage, a flipping behavior of transitional flow may also explain such an effect.

By stacking all the phase-locked averages obtained over the radial traverse to form a surface plot, the phase-span contour plot shown in Figure 7.20 is obtained.

Similarly, by plotting all the ensemble averages obtained over the radial traverse, a phase-span contour is also obtained over a full revolution, shown in Figure 7.21 only over two blade passages for in order to allow a comparison.

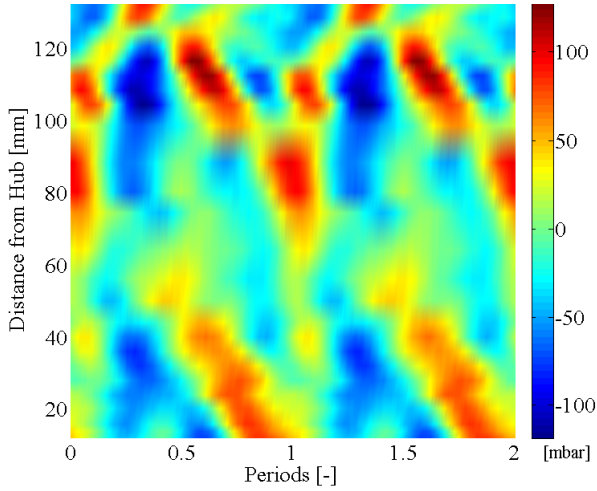

Figure 7.20: Phase-locked average map of the turbine exit total pressure field

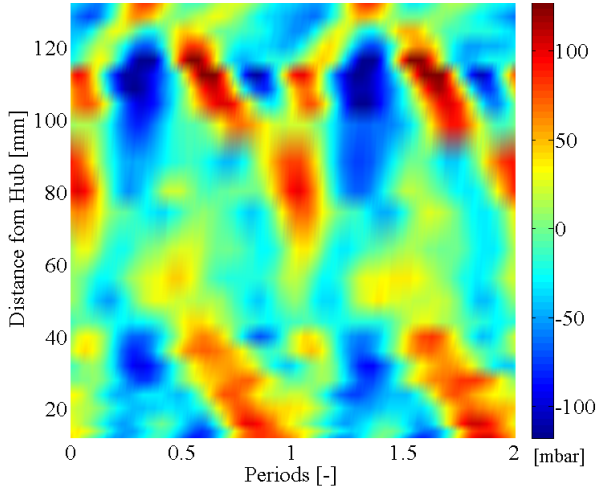

Figure 7.21: Ensemble average map of the turbine exit total pressure field

As explained before, an agreement is found between the phase-locked average map and the ensemble average map. The coarser nature of the ensemble average map is due to the fact that the number of data points used for the averaging process in the ensemble average is 82 times less than that of the phase-locked average by definition.

Likewise a similar agreement is found between the standard deviation maps of the phase-locked average and the ensemble average, presented in Figures 7.22 and 7.23 respectively.

Given the lack of information on engine specifications and running conditions apart from the trigger signal on the same shaft, no further conclusions may be drawn from the obtained maps.

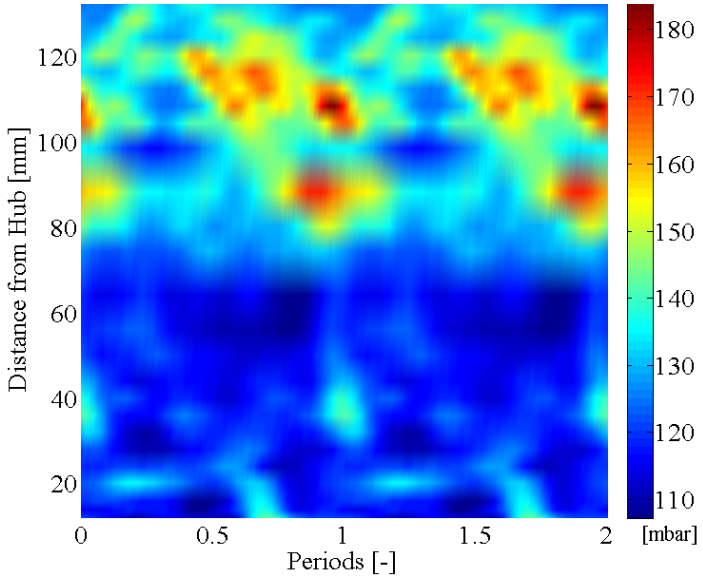

Figure 7.22: RMS of the phase-locked average map of the turbine exit total pressure field at S4

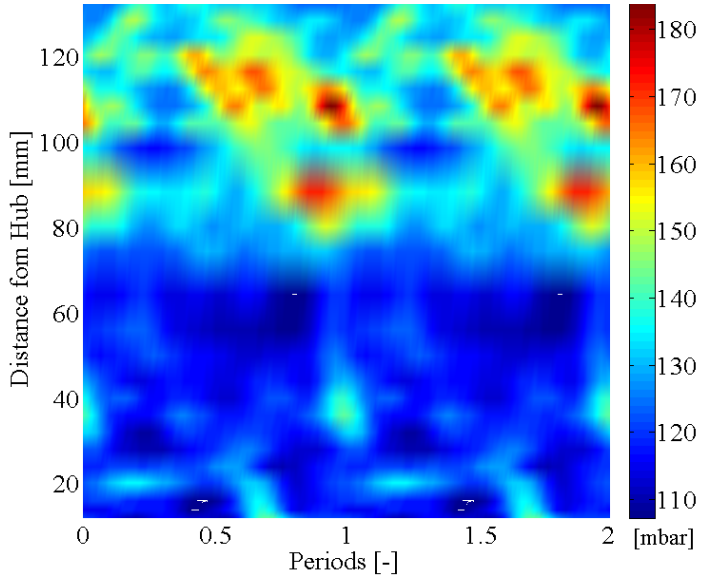

Figure 7.23: RMS of the ensemble average map of the turbine exit total pressure field at S4

7.3 Summary

Following the prototype testing phase, a new probe has been designed with numerous improvements which include the use of a leadless sensor and a different harness layout for better shielding of the signal against electromagnetic interferences and hence a higher signal-to-noise ratio. Furthermore, the probe stem has also been modified for facilitating rigging in facilities with access constraints.

Significant improvements were achieved on the signal quality. However, a significant steady signal mismatch has been observed which is attributed to the use of a leadless sensor, creating a temperature gradient across the transducer membrane in cooled applications.

Once again, the probe has survived the harsh conditions of Volvo RM-12 two-spool military turbofan engine without any issue.

Chapter 8

Conclusions

Measuring flow quantities in turbomachinery environments remains a strongly desired area of research since the advent of the first turbojet engines. The 1970s mark the well established steady-state measurement techniques, and a booming research activity on unsteady methods.

Although several probes for steady-state measurements already exists, unsteady measurements in the hot sections of modern aero-engines and gas-turbines such as the rear stages of compressors, combustion chambers and turbines is still a domain that needs in-depth investigation.

During the course of this study, hot sections of turbomachines are accessed for the first time to the knowledge of the author using fast-response instrumentation and successful measurements are accomplished where a temperature capability of 2000 K is demonstrated in a kerosene burner rig. Following this milestone, the new area of research in turbomachinery instrumentation field will be the quantification and correction of measurement errors in high-temperature environments.

Concerning the measurement of unsteady pressure values, two different approaches stand out, which are sensors based on piezo-electric and piezo-resistive technology. As the piezo-electric sensor is in fact a force transducer, a diaphragm very much looking like the inlet valve found on piston engines is used to transmit the pressure onto the piezo element, requiring large diaphragm diameters while only measuring fluctuating components. The piezo-resistive sensors on the other hand, can measure both the steady and the fluctuating components and can be manufactured with membrane sized as small as 0.6 mm in diameter, allowing total sensor size as small as 1 mm by 1 mm.

Prior research on unsteady pressure measurement techniques has indicated the suitability of piezo-resistive transducers for the design of pressure probes intended for measuring turbomachinery flows.

The superiority of cylindrical probes, which are immune to certain unsteady aerodynamic effects such as dynamic stall and lift, compared to wedge probes has been proven during the studies conducted at the von Karman Institute over the last two decades.

An effort started two decades ago has grown fruits establishing the VKI among other institutions such as Oxford University, Cambridge University and Swiss Federal Institute of Technology Zürich (ETH) in the field of unsteady measurement techniques. Important experience has been gained on key techniques such as sensor packaging and manufacturing of miniature probes using non-conventional techniques such as electric-discharge machining and micro-machining. Various probes based on conventional piezo-resistive sensors as small as Ø1.5 mm in diameter that can withstand continuous temperatures around 120°C have been successfully manufactured and used. Several error sources such as unsteady lift, vortex shedding and dynamic stall have been investigated both computationally and experimentally thanks to a probe design with a base bleed as presented by Brouckaert in his Ph.D. thesis [7].

This study is particularly focused on high temperature measurements, more specifically on the measurement of the unsteady pressure field in the hottest parts of Brayton engines such as the combustors and the high pressure turbine stages, at conditions where no measurements were possible a priori.

In order to achieve this goal, a cooled probe that can withstand these harsh environments was developed. Due to the necessity of manufacturing the smallest probe size, and ensure adequate cooling, the sensor is encapsulated with cooling channels.

In addition to the design and manufacturing of cooled probes, an automated cooling system and signal conditioning circuitry have also been designed and manufactured at the VKI.

A first prototype with a head diameter if 8 mm was manufactured after a thorough analysis of the heat transfer and coolant flow properties using a wire-bonded silicon-on-insulator (SOI) piezo-resistive pressure

transducer. Inconel 600 alloy, typically used in turbomachinery components, was used for the construction. In order to protect the sensor in harsh environments against any probable foreign object damage due to impinging particles and to improve the cooling, a screen was placed in front of the membrane which was also instrumental in cooling the sensor at the expense of a reduced frequency bandwidth.

The manufactured probe was calibrated and its dynamic and aerodynamic properties were well investigated prior to the measurement campaigns. The frequency bandwidth following the shock-tube testing was found to be limited to a flat response below 25 kHz due to the presence of a line-cavity resonance around 40 kHz at room temperature.

Although electron beam particle vapor deposition thermal barrier coating (EBPVD-TBC) process that will further improve temperature capability of the cooled probe was investigated and envisaged, such a coating has not yet been applied.

The first prototype was successfully tested in a turbojet engine, downstream the turbine rotor and in a combustor rig at temperatures approaching stoichiometric conditions, exceeding 2000 K at times. During these tests, an important experience on improving signal-to-noise ratio, operation of such a complex system composed of many components in a real environment was gained.

At high-temperature flow conditions, significant increases in the line-cavity resonance, greatly enhancing the frequency bandwidth of the cooled probe, due to the increase of the speed of sound and hence the Helmholtz frequency were observed. As the dynamic response of the cooled probe varies with respect to temperature, the transfer functions obtained at room temperature conditions could not be applied to the measurements at high temperature conditions. Without a high-temperature shock-tube, it is impossible to determine these required dynamic response transfer functions. Even then, at temperatures well above the membrane capability, where cooling is necessary, ensuring the appropriate thermal conditions truly poses a challenge.

The presence of a proper trigger is essential for unsteady measurement campaigns. In the lack of such a signal, aligning and phase informa-

tion from the measurements in the turbojet engine test, essential for the reconstruction of the flow-field in a blade-passage, were lost.

Due to the lack of validated unsteady data, only the steady components of the measured quantities were compared to existing measurement data, and perfect agreement (within $\pm$ 1%) on these values are found.

An important area that needs to be addressed via thorough studies is the blockage effect for such an intrusive technique. Although several publications are available, this domain remains a virgin field of research having a vital importance for the quantification of errors introduced.

Following the first prototype, lessons learned were applied on the second generation design of the cooled probe. A relatively new technology for the field, the leadless sensor was also utilized for this design. The second generation probe manufactured was tested on a low-bypass military turbofan engine downstream the low-pressure turbine rotor. Great improvements on the quality of the signals acquired and the facility of rigging, operation and de-rigging were achieved.

With the leadless sensor, where the sensing piezo elements are protected behind a variable thickness membrane, a mismatch on the DC levels (i.e. steady components) was observed. The errors are suspected to be caused by the thermal gradient at the back end of the sensor membrane, where the piezo elements which are not only sensitive to strain but also to temperature are placed. Although this fact may not pose a problem for uncooled applications, where temperature levels are relatively steady, it prohibits the use of leadless sensors for cooled probe designs. It is therefore important to employ conventional sensors where the resistive elemets face the measurement medium in cooled probe designs, where thermal gradient is an issue.

Measurements in a real turbomachinery environment should not be underestimated. On one side, the electromagnetic interference (EMI) and radio frequency interference (RFI) effects together with high levels of acoustic and mechanical excitations require the use of rugged equipment, as conventional laboratory grade computers, data-loggers and signal conditioning modules repeatedly fail. Special care should be given

for the isolation of the electronic equipment from any potentially harmful source including the power grid and even the chassis of the machine on which measurements are intended. On the other side, at temperature levels well exceeding the metal melting points, thermal and structural loadings must be seriously analyzed just as in the design of the machine components themselves.

Some of the error sources determined within this study may be listed as blockage effects, determination of dynamic response transfer functions with respect to temperature and investigation of thermal gradients across sensor membrane.

Concerning *future work*, a new signal conditioning module, allowing to track each piezo element composing the Wheatstone bridge on a piezo-resistive pressure transducer independently is currently developed. However, creating a thermal gradient across the sensor in a controlled laboratory environment, which is crucial for the static calibration for such a case still remains a true challenge.

The current state-of-the art at the VKI allows the manufacturing of probes that can withstand 250°C continuously without cooling. At the end of the ongoing studies, a temperature capability of 500°C is expected to be achieved for uncooled applications. Cooled probes will also benefit greatly from this achievement as the cooling requirements will greatly decrease, opening the gate for using shop-air instead of distilled water, rendering the massive and complicated cooling system unnecessary and achieving a higher technology readiness level (TRL), marking a milestone in introducing cooled probe applications to regular testing operations.

Bibliography

[1] Ainsworth, R. W., Allen, J. L., and Dietz, A. J. Methods for Making Unsteady Aerodynamic Pressure Measurements in a Rotating Turbine Stage. *Paper 22, AGARD CP 468, Luxembourg*, 1989. 41

[2] Ainsworth, R. W., Miller, R. J., Moss, R. W., and Thorpe, S.J. Unsteady Pressure Measurement. *Meas. Sci. Technol.*, Vol. 11, 2000. 7

[3] American National Standards Institute, and American Society of Mechanical Engineers, . *ANSI/ASME PTC 19.1-2005 Measurement Uncertainty*. American Society of Mechanical Engineers, 2006. 105

[4] Anderson, S. J., Chana, K. S., and Wilson, A. J. W. Design, development and testing of an in-engine radial traverse system for the trent engine. In *Proceedings of ASME Turbo Expo 2008*, ASME GT-2008-51332, Berlin, Germany, June 2008. xix, xx, 25, 26

[5] Ashby, G. C. Jr. Pressure measuring probe, Pat. No. 4783994, 1988. xix, 23

[6] Bergh, H.; Tijdeman, H., . Theoretical and experimental results for the dynamic response of pressure measuring systems. *NLR-TRF.283*, 1965. 43, 112

[7] Brouckaert, J. F. *Development of Fast Response Aerodynamic Pressure Probes for Time-Resolved Measurements in Turbomachines*. PhD thesis, Université Libre de Bruxelles/von Karman Institute for Fluid Dynamics, Sint Genesius-Rode, Belgium, October 2002. 9, 43, 174

[8] Carta, F. O. and Obrien, R. L. Unsteady aerodynamic measurement techniques for turbomachinery research. In B. Lakshminarayana & P. Runstadler Jr., , editor, *Measurement Methods in Rotating Components of Turbomachinery*, pages 177–185, 1980. 7

[9] Chana, K. S. Fluid temperature measurement, Pat. No. 7377687, May 2008. 4

[10] Cherret, M.P., . Temperature error compensation applied to pressure measurements taken with miniature semiconductors pressure transducers in a high speed research compressor. In C.H. Sieverding & T. Arts, , editor, *Proceedings of the 10th Symposium on Measuring Techniques for Transonic and Supersonic Flows in Cascades and Turbomachines, VKI*, Rhode-St-Genese, Belgium, September 1990. 14

[11] Chivers, J. High temperature pressure sensors for gas turbine applications. In *Advanced High Temperature Instrumentation for Gas Turbine Applications*, VKI LS 2009-06, Rhode-Saint-Genese, Belgium, May 11-14 2009. 13

[12] Cook, R. L. Aeroacoustic transducer, Pat. No. 4964091, 1990. 17

[13] Corporation, International Business Machines. IBM advances chip technology with breakthrough for making faster, more efficient semiconductors. News Release, on the world-wide web, Aug 1998. East Fishkill, N.Y., U.S.A., *http://www-03.ibm.com/press/us/en/pressrelease/2521.wss*. 10

[14] Denton, J. D. The 1993 igti scholar lecture: Loss mechanisms in turbomachines. *Journal of Turbomachinery*, 115(4):621(36), 1993. 14

[15] der Technischen Uberwachungs-Vereine (VdT UV), Verband. *Arbeitsgemeinschaft Druckbeh alter Merkblatt B-Series (design)*. Carl Heymanns Verlag, Cologne, Germany, january 1995 edition, 1995. 69, 70

[16] Dieck, Ronald H. *Measurement uncertainty: methods and applications*. ISA, NC, 4th edition, 2007. 105, 108

[17] Dittus, F. W. and Boelter, L. M. K. *Publications on Engineering*, volume 2. University of California, Berkeley, 1930. 48

[18] Epstein, A. H. High frequency response measurements in turbomachines. In *VKI Lecture Series on Measurement Techniques in Turbomachines*, VKI LS 1985-03, 1985. 43

[19] European Virtual Institute for Gas Turbine Instrumentation (EVI-GTI), . The lab gap matrix. on the world-wide web. *http://www.evi-gti.com/download/keyconcepts/Joint_LGM_issue0.xls*, MS-Excel Spreadsheet. xx, 3, 33

[20] Ferguson, D. G. *The Development of Air Cooling Techniques for Fast Response Pressure Transducers in High Temperature Environments*. PhD thesis, Cranfield University, Cranfield, United Kingdom, October 1997. 13

[21] Ferguson, D. G. and Ivey, P. C. Unsteady pressure measurement in a high temperature environment using water cooled fast response pressure transducers. In *IGTI TURBO/EXPO paper no 95-GT-345*, Houston, Texas, U.S.A., June 1995. 15

[22] Ferguson, D. G. and Ivey, P. C. A high-temperature assessment of air-cooled unsteady pressure transducers. *Transactions of the ASME*, 120:608–612, June 1998. 15

[23] Gahan, D. High temperature sapphire fiber optic sensor. In *Advanced High Temperature Instrumentation for Gas Turbine Applications*, VKI LS 2009-06, Rhode-Saint-Genese, Belgium, May 11-14 2009. 9

[24] Gossweiler, C. *Sonden und Messsystemen fur Schnelle Aerodynamische Strommungsmessung mit Piezoresistiven Druckgebern*. PhD Thesis, The Swiss Federal Institute of Technology Zurich (ETH Zurich), Zurich, Switzerland, 1993. 42

[25] Grey, J. Thermodynamic methods of high temperature measurement. In *ISA Transactions*, volume 4, pages 102–115, April 1965. 20

[26] Grey, J. Probe measurements in high-temperature gases and dense plasmas. In Eckert, E. R. G. and Goldstein, R. J., editors, *AGARDograph on 'Measurement Techniques in Heat Transfer'*, volume 130, pages 269–307. NATO AGARD, November 1970. xix, xx, 20, 21, 22, 23, 26, 27

[27] Humm, H.J., . Optimierung der Sondengestalt für aerodynamische Messungen in hochgradig fluktuierenden Strömungen. *Dissertation ETH Nr. 11661 Zürich.*, 1996. 138

[28] Inci, M.N., Kidd, S.R., Barton, J.S., and Jones, J.D.C. High temperature miniature fibre optic interferometric thermal sensors. *Measurement Science and Technology*, 4(3):382, 1993. 9

[29] Incropera, F.P. and DeWitt, D.P. *Fundamentals of heat and mass transfer*. Wiley, 1990. 51

[30] International Organization for Standardization, . *Guide to the expression of uncertainty in measurement, Supported by BIPM, IEC, IFCC, ISO IUPAC, IUPAP and OIML*. International Organization for Standardization, Geneva, 1995. 105

[31] Ivey, P. C. and Ferguson, D. G. An air cooled jacket designed to protect unsteady pressure transducers at elevated temperatures in gas turbine engines. In *Proceedings of ASME Turbo Expo 2002*, Amsterdam, The Netherlands, June 2002. xix, 16, 17

[32] Ivey, P. C. and Ferguson, D. G. An air cooled jacket designed to protect unsteady pressure transducers at elevated temperatures in gas turbine engines. In *Proceedings of ASME Turbo Expo 2002*, Amsterdam, The Netherlands, June 2002. 15, 45

[33] Kersey, A.D. and Dandridge, A. Two-wavelength interferometric fiber temperature sensor. In *Optical Fiber Communication Conference*, Reno, Nevada, January 1987. 9

[34] Kestin, J. and Wood, R. T. The influence of turbulence on mass transfer from cylinders. *Journal of Heat Transfer*, 93 C:321–327, 1971. 34

[35] Kupferschmied, P., Koppel, P., Gizzi, W., and C. andGyamarthy-Roduner, G. Time-resolved flow measurements with fast-response aerodynamic probes in turbomachines. *Measurement Science and Technology*, 11(7):1036–1054, July 2000. 138

[36] Kupferschmied, P.; Köppel, P.; Gizzi, W.; Roduner, C.; Gyamarthy, G., . Time-Resolved Flow Measurements With Fast Response Aerodynamic Probes In Turbomachines. *Meas. Sci. Technol.*, Vol. 11, 2000. 7

[37] Kupferschmied, P.; Roduner, C.; Gyarmathy, G., . Some Considerations on Using Miniature Pressure Sensors in Fast Response Aerodynamic Probes for Flow Temperature Measurements. In *Proceedings of the 14^{th} Symposium on Measuring Techniques for Transonic and Supersonic Flows in Cascades and Turbomachines*, Limerick, Ireland, 1998. 14

[38] Kurtz, A. D., Chivers, J. W. H., Ned, A. A., Goodman, S., Epstein, A. H., and Beheim, G. Improved ruggedised high temperature pressure transducers for gas turbine research development and active gas turbine control. VKI LS 2004-04, von Karman Institute, St. Genesius-Rode, Belgium, 2004. xxiv, 149

[39] Kurtz, A. D., Ned, A. A., and Epstein, A. H. Improved ruggedized soi transducers operational above 600c. In *Twenty-First Transducer Workshop*, Lexington, Maryland, U.S.A., June 2004. xix, 11, 12

[40] Kurtz, A. D., Ned, A. A., and Epstein, A. H. Ultra high temperature, miniature, soi sensors for extreme environments. In *IMAPS International HiTEC 2004 Conference*, Santa Fe, New Mexico, U.S.A., May 2004. xix, 12

[41] Kurtz, A. D., Nunn, T. A., Briggs, S. A., and Ned, A. Very high temperature silicon on silicon pressure transducers. In Singh, J. J. and Antcliff, R. R., editors, *Measurement Technology for Aerospace Applications in High Temperature Environements*, volume 3161 of *NASA Conference Publication*, pages 291–300, 1992. 10

[42] Lagen, N. T., Reece, G. D., Eves, J. W., and Geissinger, S. L. Water cooled static pressure probe, Pat. No. 5076103, 1991. xix, 23, 24

[43] Lakshminarayana, B. Techniques for aerodynamic and turbulence measurements in turbomachinery rotors. In B. Lakshminarayana & P. Runstadler Jr., , editor, *Measurement Methods in Rotating Components of Turbomachinery*, pages 5–29, 1980. 7

[44] Langmuir, I. The pressure effect and other phenomena in gaseous discharges. In *J. of the Franklin Institute*, volume 196, pages 751–762, December 1923. 20

[45] Larguier, R. Experimental analysis methods for unsteady flows in turbomachines. *Journal of Engineering for Power*, 103, 1981. 43

[46] Larguier, R. Experimental analysis methods for unsteady flows in turbomachines. In *International Symposium on Air Breathing Engines, 7th, Beijing, People's Republic of China, September 2-6, 1985, Proceedings (A86-11601 02-07). New York, AIAA, 1985, p. 279-289.*, pages 279–289, 1985. xx, 29

[47] Lowery, G. W. and Vachon, R. I. The effect of turbulence on heat transfer from heated cylinders. *International Journal of Heat and Mass Transfer*, 18:1229–1242, November 1975. xxi, 34, 56

[48] Lubbock, R. J. and Oldfield, M. L. G. Unsteady gas turbine flow measurements using fast-insertion high bandwidth total temperature and pressure probes. In *2nd Joint EVI-GTI/PIWG International Gast Tubine Instrumentation Conference*, EVI2008-029, Seville, Spain, September 2008. xix, 18, 19

[49] Jr.Mallon, J. R. Technology trends in high temperature pressure transducers: The impact of micromachining. In *NASA. Langley Research Center, The 1992 NASA Langley Measurement Technology Conference: Measurement Technology for Aerospace Applications in High-Temperature Environments p 251-254 (SEE N93-13661 03-35)*, pages 251–254, September 1992. 10

[50] Massini, M., Miller, R.J., and Hodson, H.P. Intermittent aspirated probe for measurements of stagnation pressure and temperature. In *Advanced High Temperature Instrumentation for Gas Turbine Applications*, VKI LS 2009-06, Rhode-Saint-Genese, Belgium, May 11-14 2009. xx, 26, 27

[51] Mendez, H. Silicon-on-insulator – soi technology and ecosystem – emerging soi applications. on the world-wide web, Apr 2009. *http://www.soiconsortium.org/pdf/Consortium_9april09_final.pdf*, PDF Presentation. 10

[52] Mersinligil, M., Brouckaert, J.F., Ottavy, X., and Courtiade, N. A high temperature high bandwidth fast response total pressure probe for measurements in a multistage axial compressor. In *Proceedings of ASME Turbo Expo 2011*, ASME GT2011-45558, Vancouver, Canada, June 2011. 14

[53] Mersinligil, M., Brouckaert, J.F., Ottavy, X., and Courtiade, N. On using fast response pressure sensors in aerodynamic probes to measure total temperature and entropy generation in turbomachinery blade rows. In *Proceedings of ASME Turbo Expo 2012*, ASME GT2012-69722, Copenhagen, Denmark, June 2012. 14

[54] Moore, M. T. High temperature-high response fluctuating pressure measurements. In Fazio, G. G., editor, *ASSL Vol. 63: Infrared and submillimeter astronomy*, pages 469–473, 1977. xx, 28

[55] Morgan, V. T. The overall convective heat transfer from smooth circular cylinders. In *Advances in heat transfer. Volume 11. (A76-17076 05-34) New York, Academic Press, Inc., 1975, p. 199-264.*, volume 11, pages 199–264, 1975. 34

[56] Ned, A. A., Kurtz, A. D., Beheim, G., Masheeb, F., and Stefanescu, S. Improved sic leadless pressure sensors for high temperature, low and high pressure applications. In *Twenty-First Transducer Workshop*, Lexington, Maryland, U.S.A., June 2004. xix, 13, 15

[57] Niska, H. Requirements for advanced high temperature instrumentation and measurements in gas turbine engines. In *Advanced High Temperature Instrumentation for Gas Turbine Applications*, VKI LS 2009-06, Rhode-Saint-Genese, Belgium, Rhode-Saint-Genese, Belgium, May 11-14 2009. 3

[58] Okojie, R. S., Fralick, G. C., Saad, G. J., Blaha, C. A., Adamczyk, J. J., and Feiereisen, J. M. A single crystal sic plug-and-play high temperature drag force transducer. In *TRANSDUCERS, The 12th International Conference on Solid-State Sensors, Actuators and Microsystems*, volume 1, pages 400–403, June 2003. 13

[59] Oldfield, M. L. G. and Lubbock, R.J. Fast insertion pressure and temperature probes. In *Advanced High Temperature Instrumentation for Gas Turbine Applications*, VKI LS 2009-06, Rhode-Saint-Genese, Belgium, May 11-14 2009. 19

[60] P. D. Baker & R. A. Masom, , editor. *Pressure instrumentation for gas turbine engines - A review of measurement technology*, April 1978. 7

[61] Passaro, A., LaGraff, J. E., Oldfield, M. L. G., and Biagioni, L. Fast acting probe for measurement of turbulent pressure and temperature fluctuations in a gas turbine combustor. In *44th AIAA Aerospace Sciences Meeting and Exhibit*, AIAA 2006-550, Reno, Nevada, January 2006. 18, 34

[62] Pau, M. *Design of the Cooling System for a High Temperature Fast Response Total Pressure Probe*. Diploma course project report, von Karman Institute for Fluid Dynamics, Sint Genesius Rode, Belgium, June 2006. 59

[63] Propulsion Instrumentation Working Group (PIWG), . Sensor specifications. on the world-wide web. *http://piwg.org/DOC/JointLabGapMatrix-summaryVersionNovember2010.xls*, MS-Excel Spreadsheet. 3

[64] Schmid, F. Dynamic pressure in extreme temperatures, capability of meggitt sensing systems. In *EVI-GTI Dynamic Pressure Measurements Workshop*, EVI2011-DPWS-008, Munich, Germany, October 2011. 9

[65] Schmidt, E. and Wenner, K. Warmeabgabe uber den umfang eines angeblasenen geheizten zylinder. *Forschung im Ingenieurwesen*, 12(2):65–73, 1941. xxii, 89, 90

[66] Schricker, A. Recent developments in high temperature dynamic pressure sensors at piezocryst. In *EVI-GTI Dynamic Pressure Measurements Workshop*, EVI2011-DPWS-009, Munich, Germany, October 2011. 9

[67] Sieverding, C. H., Arts, T., and Dénos, R. Annular cacade tests. In dunker, R., editor, *Advances in Engines Technology*. J. Wiley & Sons, 1995. xx, 43, 44

[68] Sieverding, C. H., Arts, T., Dénos, R., and Brouckaert, J.-F. Measurement techniques for unsteady flows in turbomachines. *Experiments in Fluids*, 28:285–321, 2000. 7

[69] Simon, D. L., Garg, S., Hunter, G. W., Guo, T-H., and Semega, K. J. Sensor needs for control and health management of intelligent aircraft engines. In *Proceedings of the ASME Turbo Expo*, ASME GT2004-54324, Vienna, Austria, June 2004. 2

[70] Smith, M. C. and Kuethe, A. M. Effects of turbulence on laminar skin friction and heat transfer. *The Physics of Fluids*, 9 No.12:2337–2344, 1966. 34

[71] Vyas, N. S. and Rao, J. S., editors. *Measurements of the effect of free-stream turbulence length scale on heat transfer*, June 1992. 34

[72] Wagner, W., Saul, A., and Pruss, A. International equations for the pressure along the melting and along the sublimation curve of ordinary water substance. *Journal of Physical and Chemical Reference Data*, 23(3):515, 1994. xx, 48

[73] Warnack, D. An optimized pneumatic probe for investigation of gas turbine aerodynamics in full scale gas turbines. In *Proceedings of ASME Turbo Expo 2002*, ASME GT-2002-30044, Amsterdam, The Netherlands, June 2002. xix, 24

[74] Welsh, B.L.; Pyne, C.R., . A method to improve the temperature stability of semiconductor strain gauge transducers. *Journal of Physics and Scientific Instrumentation*, 13, 1980. 14

[75] Wyler, J. S. Probe blockage effects in free jets and closed tunnels. *ASME Transactions Series Journal of Engineering Power*, 97:509–514, October 1975. 138

[76] Zukauskas, A. Heat transfer from tubes in crossflow. *Advances in Heat Transfer*, 8:93–160, 1972. 34, 59

[77] Zukauskas, A. and Ziugzda, J. *Heat transfer of a cylinder in crossflow*. Washington, DC, Hemisphere Publishing Corp., 1985, 219 p. Translation., 1985. 34